Conformation of 2-fold Anisotropic Molecules Confined on a Spherical Surface

by

Wuyang Zhang

A thesis
presented to the University of Waterloo
in fulfilment of the
thesis requirement for the degree of
Doctor of Philosophy
in
Physics

Waterloo, Ontario, Canada, 2012

AUTHOR'S DECLARATION

I hereby declare that I am the sole author of this thesis. This is a true copy of the thesis, including any required final revisions, as accepted by my examiners.

I understand that my thesis may be made electronically available to the public.

Abstract

Anisotropic molecules confined on a spherical or other curved surface can display coupled positional and orientational orderings, which make possible applications in physics, chemistry, biology, and material science. Therefore, controlling the order of such system has attracted much attention recently. Several distinct conformations of rod-like or chain-like molecules confined on a spherical surface have been predicted, including states such as tennis-ball, rectangle, and cut-and-rotate splay. These conformations have four $+1/2$ defects and are suggested to dominate over the splay conformation that has two $+1$ defects. For the purpose of investigating the conformations of 2-fold anisotropic molecules confined on the spherical surface, the author of this thesis utilizes the Onsager model to study the system of rigid rods and conducts Monte Carlo simulations on the bead-bond model to research the system of semiflexible polymer chains. At low surface coverage density, no particular pattern of the molecules would form. However, coupled positional and orientational ordering begins to emerge beyond a transition density. On the basis of the numerical solutions of the Onsager model of rigid rods, the splay conformation is shown to be the only stable state. On the other hand, Monte Carlo simulations on a polymer system indicate that the ordered state always accompanies the tennis-ball symmetry. With comparison to the continuous isotropic-nematic transition of a fluid of hard rods embedded in a flat two-dimensional space, the disorder-order transition for both the system of rigid rods and the system of polymer chains confined on the spherical surface has first-order phase-transition characteristics.

Acknowledgments

I am very grateful to Professor Jeff Z. Y. Chen, for his patient supervision and valuable direction throughout my Ph.D. program. I would also like to thank my thesis committee of Prof. Qing-bin Lu, Prof. Russell Thompson, and Prof. Hans De Sterck, who have engaged me in insightful conversations on my work. Especially, I would like to thank Professor Béla Joós, my external defense committee member from University of Ottawa. Prof. Joós provided me very helpful corrections for my thesis, which made this final version much better in literature. Besides, I really want to thank my parents and my wife as well for their support and accompany in every minute of my life. Furthermore, I also want to give thanks to my friends, Dr. Ying Jiang, Mr. Sergey Mkrtchyan, Mr. Zi Jian Long, Mr. Taoran Lin, and Mr. Yu-Cheng Su. Without them, I would not have had the motivation to complete my study. Finally, I would like to thank the Natural Sciences and Engineering Research Council of Canada for financial support and SHARCNET for computational time.

Contents

List of Figures

Chapter 1

Introduction

1.1 Anisotropic Molecules Confined on a Spherical Surface

Controlling the ordering of matter is always the leading edge in physics; it not only provides researchers opportunities to utilize and verify sophisticated theoretical ideas and mathematical methods, but also enables applications in physics, chemistry, material science, and biology due to the strong relationship between the ordering of matter and its properties. For instance, the positional ordering of atom array determines the ductility of metal, while the optical properties of liquid crystal applied in Liquid Crystal Displays rely on the orientational ordering of liquid crystal molecules. Recently, researchers have paid attention to the ordering in a system consisting of anisotropic molecules, which could have coupled positional and orientational orderings and, consequently, novel properties and applications. In an elegant paper, for example, Nelson [58] suggested the possibility of creating a 4-fold tetravalent colloid particle by coating it with a nematic shell, a sheet of anisotropic objects such as nanorods, polymers, or gemini lipids. In this case, the micron-sized particles would have four chemical linkers similar to sp^3 hybridized chemical bonds of carbon, silicon, and germanium atoms [Fig. 1.1.(B)] and then are able to arrange into a colloidal crystal with a diamond structure which has a considerably larger photonic band gap than the common bcc or fcc colloid crystal

[28]. Furthermore, the same idea of "colloidal diamonds" is useful to researchers and engineers to construct more complex materials [46, 48], which can be applied to photonic crystal optical devices and circuits [5] or biomedicine [54]. The more significant point is that, this 4-fold tetrahedral symmetry of the nematic shell, which is called the tennis-ball conformation, has explosively expanded researchers' horizon, since people had well believed that the conformation with Mermin's boojums [53]—so-called splay conformation [Fig. 1.1.(A)]—may be a good choice for the nematic shell confined to a spherical surface. The competition of 2-fold splay conformation and 4-fold tennis-ball conformation will be further discussed in this thesis.

In the system of anisotropic molecules confined to a curved surface, a question is naturally raised how the in-plane order of anisotropic molecules couples the geometric deformations of the confinement. The same question can be asked for a three-dimensional system where a bulk of anisotropic molecules interacts with a curved surface. In short, due to the curvature of the surface confining the anisotropic molecules, the conformation of molecules could spontaneously generate some topological defects which break the symmetry of the system of anisotropic molecules and, hence, create orders coupled in the orientational and spatial distributions [84, 85]. This thesis focuses on the conformation of 2-fold anisotropic molecules confined on a spherical surface. The 2-fold molecule means that the molecule is identical to itself if rotated by 180°; such system includes rod-like liquid crystals, polymer chains, etc.

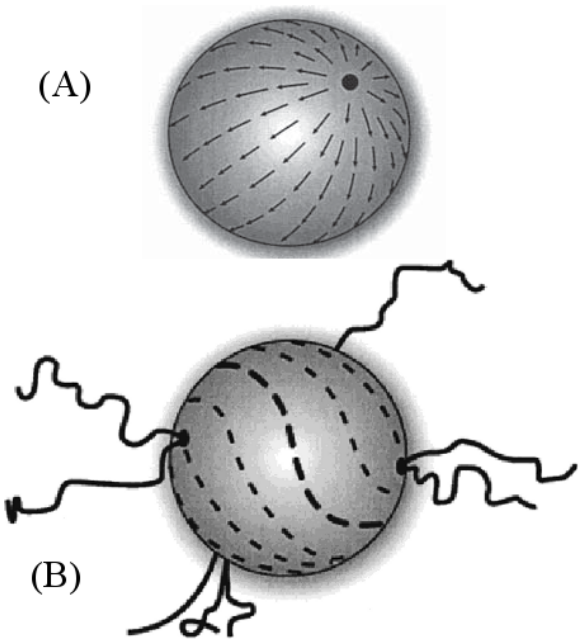

Figure 1.1: (taken from Ref. [58])(A) The splay conformation has two Mermin's boojums (point defects with topological index +1) on the north and south poles of the sphere. (B) The "tennis-ball" conformation has four chemical linkers similar to sp^3 hybridized chemical bonds.

1.2 Extension to Three Dimensions

Beyond the two-dimensional system, the conformation of the anisotropic molecules interacting with a curved surface in three dimensions is quite interesting as well and even more complicated.

For the system of *liquid crystals*, Huber and Stark [31] suggested that a hard sphere dispersed into a nematic liquid crystal would drive the conformation of liquid crystal surrounding it to display a "tennis-ball" symmetry. In experiments, a nematic shell confined by double-emulsion drops may display various, complicated conformations [25, 48]. Fig. 1.2 shows some typical conformations of a nematic shell in a double emulsion drop with the inner drop of radius a and the outer drop of radius R, where the nematic shell could have four defects, three defects, or two defects. Note that the thickness of nematic shell is heterogeneous, since the inner and outer drop are not concentric due to gravitational force.

The model of anisotropic molecules interacting with a curved surface is also related to another class of systems — *polymer chains* in confined geometries. Typical examples include DNA wrapped around histones in the structure of chromatin [39, 63, 50, 71, 24] (or similarly polyelectrolyte adsorbed on colloid particles or micelles [82, 52]) and DNA packaging in bacteriophage capsid [23, 70, 13, 64, 94]. Understanding the physical mechanism of DNA conformation in nucleosomes or bacteriophage capsids can help us to realize and even master artificial manipulation of DNA. As a result, the model of a polymer chain adsorbed onto a spherical, cylindrical, or other non-planar surface has been developed to investigate the DNA-confinement complexation. A primarily interesting topic of this model is the adsorption-desorption transition, which has been studied theoretically [86, 22, 60, 42, 89, 18] or by computer simulations [87, 1, 80] for polymer chains of different lengths and flexibilities. A range of various configurations of polymer adsorbed on a spherical surface, such as "tennis-ball" like, solenoid, and multiloop conformations, were also unveiled [1, 80]. Fig. 1.3 shows some conformations of semiflexible polyelectrolyte/particle complexes at various chain rigidities k_{ang} and ionic concentrations C_i. On the other hand, the experiments of DNA packaging in bacteriophage capsids unveiled that DNA could be packaged in a highly condensed set of rings

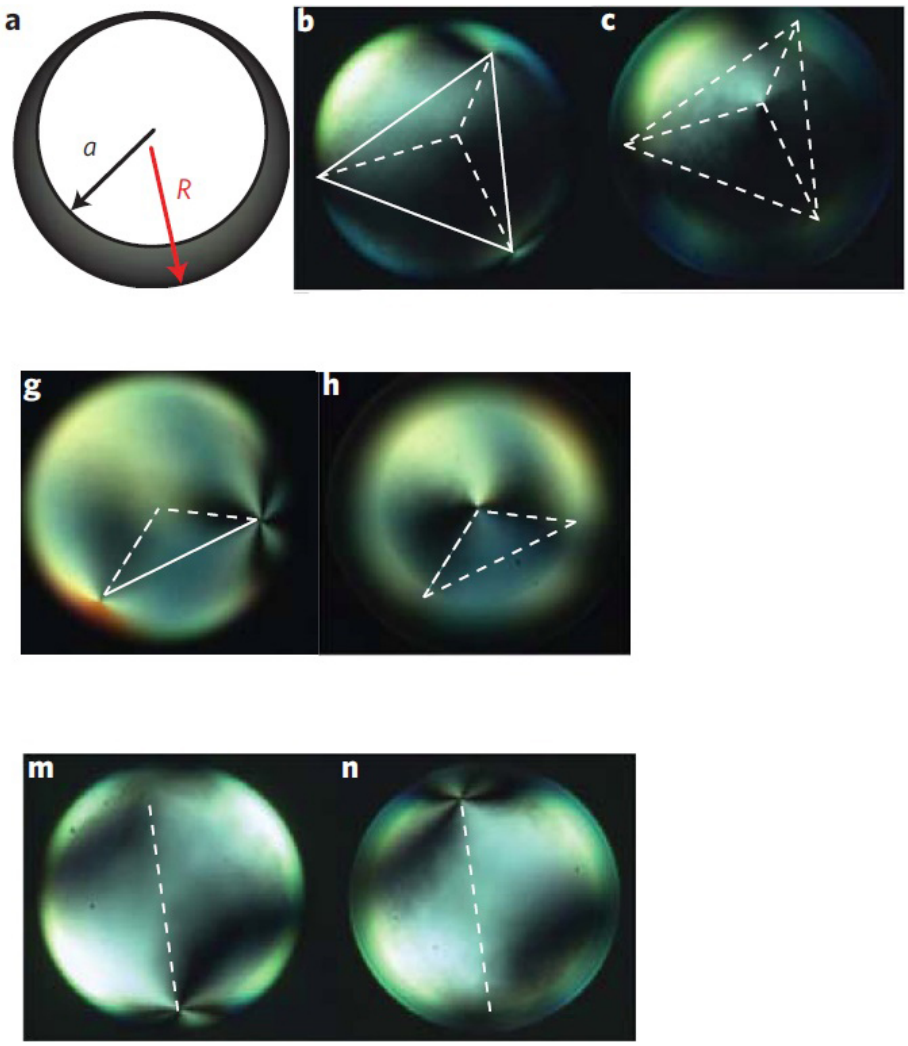

Figure 1.2: (taken from Ref. [48]) The conformation of a nematic shell in a double emulsion drop, where the radii of inner and outer drops are a and R respectively (a), could have four $+1/2$ defects (b and c), three defects (g and h), or two $+1$ defects (m and n).

concentric due to the confinement of the capsid shell (Fig. 1.4). Therefore, some authors looked into the model of a polymer chain confined inside a sphere theoretically [62, 37] or by computer simulations [37, 6, 44, 3] and discussed various possible conformations of polymer chain, say spool-like, helical, coaxial, and concentric.

In summary, the three-dimensional system of anisotropic molecules interacting with a curved surface is fundamental for us to comprehend some significant physical, chemical, and biological phenomena and develop related applications. Of course, for the purpose of understanding the three-dimensional system, it is a prerequisite to understand the two-dimensional system of anisotropic molecules confined on a curved surface that will be discussed in this thesis.

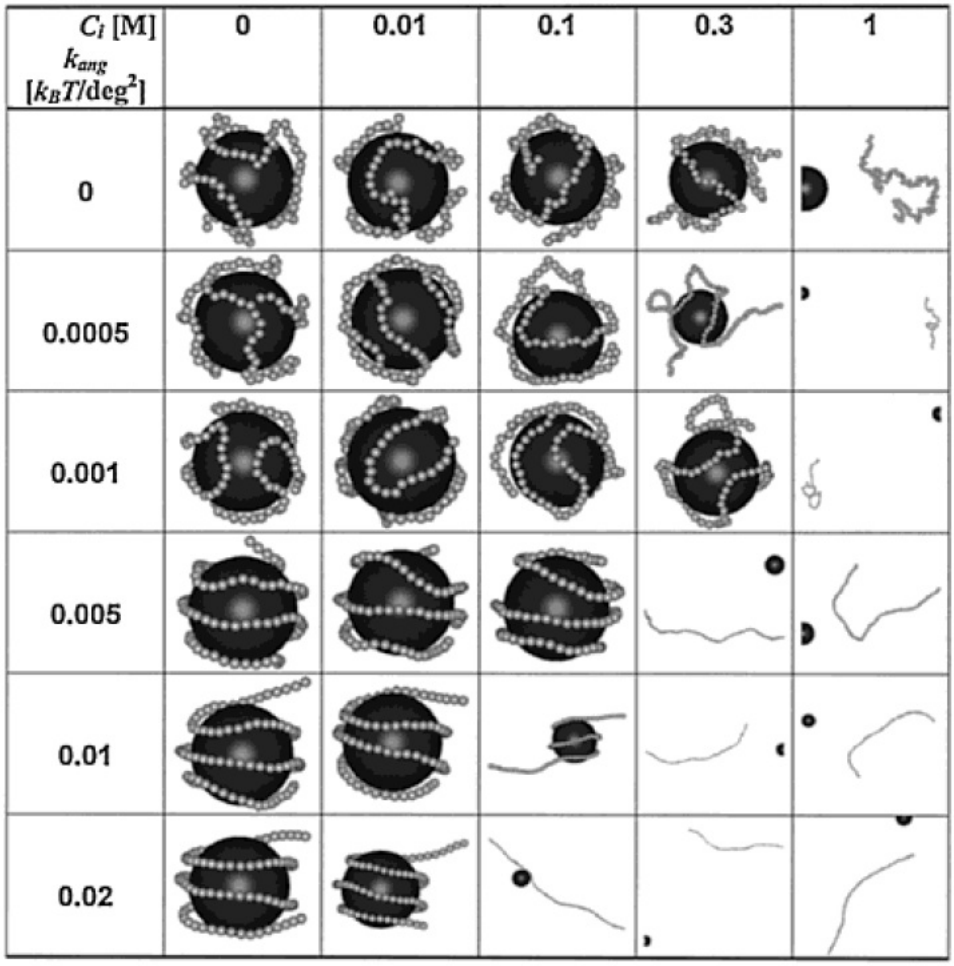

Figure 1.3: (taken from Ref. [80]) The Monte Carlo snapshots of semiflexible polyelectrolyte/particle complexes vary at different chain rigidities k_{ang} and ionic concentrations C_i. The polymer chain is stiffer in greater k_{ang}, while greater C_i is more likely to prevent the adsorption.

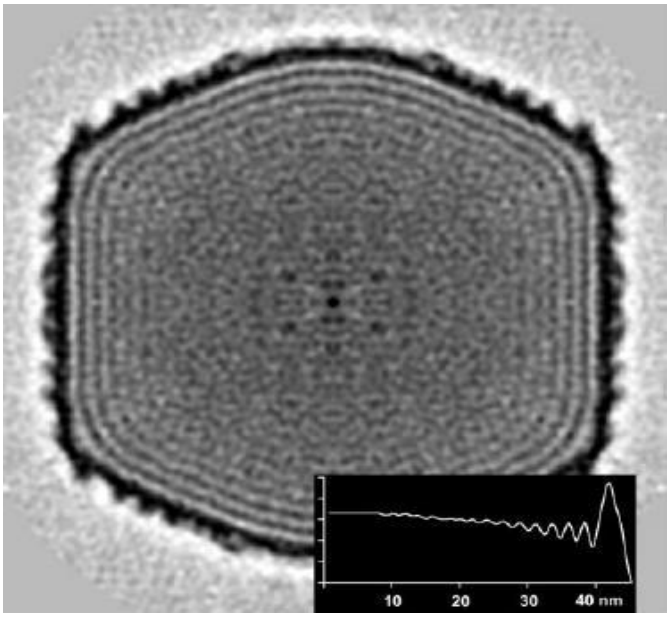

Figure 1.4: (taken from Ref. [64]) DNA of bacteriophage T4 is shown to be packaged in a highly condensed set of rings concentric to the capsid shell observed by cryo-electronic microscopy and image reconstruction techniques. The inset shows the spherically averaged density of DNA as a function of radius.

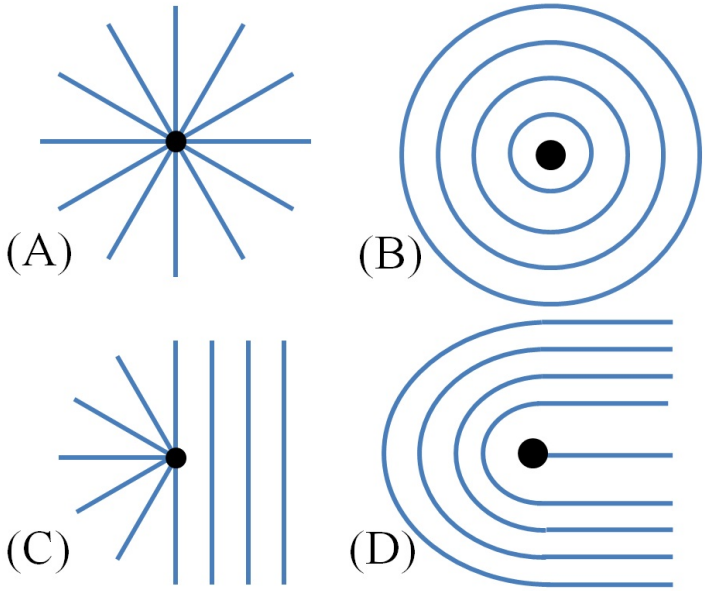

Figure 1.5: +1 defects (A and B) and +1/2 defects (C and D).

1.3 Topological Defects and Theoretical Models

1.3.1 Topological point defects and Poincaré-Hopf theorem

The conformation of anisotropic molecules confined on a two-dimensional curved surface could have one or more defects. For the purpose of studying the conformations, it is helpful for us to understand some basic ideas of defects. In topology, a defect is described by its index (or charge), which is defined by the revolution that the orientational field rotates around the defect. Fig. 1.5 shows some typical defects which could exist in a field consisting of 2-fold "vectors". In Fig. 1.5.(A) and (B), the orientational field turns 2π counterclockwise following a path encircling the defect counterclockwise; therefore, the index is defined as +1. In Fig. 1.5.(C) and (D), the orientational field turns π counterclockwise instead of 2π; therefore, the index is defined as +1/2.

According to knowledge of differential geometry, although the conformations of anisotropic molecules could be very complicated, all of them must follow a simple

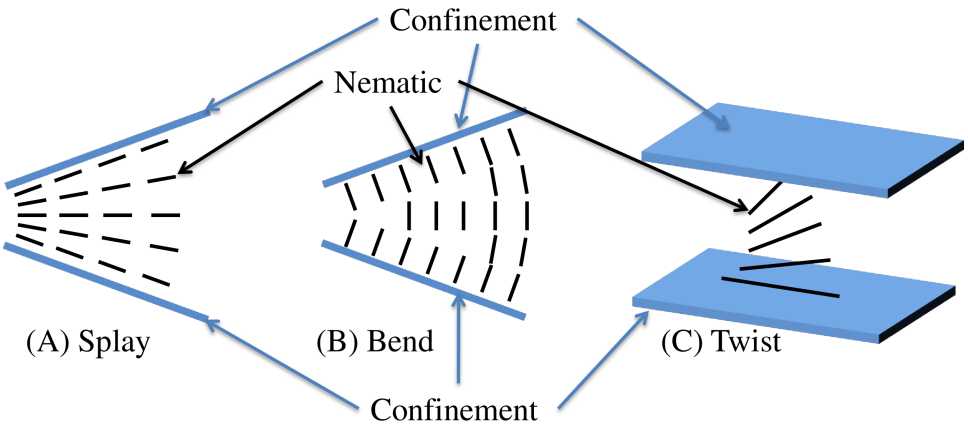

Figure 1.6: Three distortions of nematic field: (A) splay ($\nabla \cdot \mathbf{n} \neq 0$), (B) bend ($\nabla \times \mathbf{n} \perp \mathbf{n}$), and (C) twist ($\nabla \times \mathbf{n} \parallel \mathbf{n}$). The twist distortion doesn't exist in two dimensional space.

rule of topology, which is described by the Poincaré-Hopf theorem [66, 30, 79]. For a field confined on a closed surface S, the sum of the indexes of all defects must equal to the Euler characteristic of the closed surface, i.e.

$$\sum_i \sigma_i = \chi_S, \tag{1.1}$$

where σ_i is the index of i-th defect and χ_S is the Euler characteristic of surface S. In particular, $\chi_S = 2$ for any spherical or ellipsoidal surface, which implies that the sum of the defect indexes must be 2 for a spherical nematic shell. This is why researchers [25, 48] found that the conformations of a nematic shell could have two $+1$ defects, four $+1/2$ defects, or two $+1/2$ and one $+1$ defect combination.

The Poincaré-Hopf theorem provides us a framework within which we search for possible conformations by means of various theories and models.

1.3.2 Continuum model

If we are interested in a close pack of anisotropic molecules confined on a spherical surface, it is a good idea to apply a continuum model, such as the Frank continuum theory and Landau-de Gennes model, to investigate such system. In the continuum

model, the orientational distributions (Fig. 1.6) of rod-like molecules are modeled by a vector field $\mathbf{n}(\mathbf{r})$, i.e., the direction $\mathbf{n}$ of the molecule as a function of its position $\mathbf{r}$. Corresponding spatial derivatives, $\nabla \cdot \mathbf{n}$, $\mathbf{n} \cdot (\nabla \times \mathbf{n})$, and $\mathbf{n} \times (\nabla \times \mathbf{n})$, characterize splay, twist, and bend distortions of the director field, respectively. The Frank free energy is written as a sum of quadratic powers of the derivatives, with the corresponding phenomenological splay, twist, and bend coefficients, K_1, K_2, and K_3 [21]. On a two dimensional surface, K_2 is absent, since $\nabla \times \mathbf{n}$ is always perpendicular to the surface for a two dimensional system. Therefore, we are left with only splay and bend distortions. As Nelson suggested [58], one can use the Frank continuum model to study the colloid particle coated by a layer of nematic shell. The Frank free energy of the nematic shell is written as

$$F_{\text{Frank}} = \frac{1}{2} \int_{S^2} \left[K_1 (\nabla \cdot \mathbf{n})^2 + K_3 (\nabla \times \mathbf{n})^2 \right] \mathrm{d}\mathbf{r}. \tag{1.2}$$

With the *one* Frank constant approximation ($K_1 = K_3$), the Frank free energy (1.2) can be mapped into the energy of the ferromagnetic two-dimensional XY model [59]. Then, one can show that the free energy is proportional to the square of the defect index. In other words, $+1/2$ defect has only quarter of energy of $+1$ defect. Hence, the total energy of four $+1/2$ defects is lower than that of one $+1$ and two $+1/2$ combination, and, of course, lower than that of two $+1$ defects. Moreover, to minimize the defect-defect repulsion, it is the best that the four $+1/2$ defects are arranged to sit at the four vertices of a tetrahedron. Therefore, coating a colloid particle with a layer of anisotropic molecules would create 4-fold tetrahedral symmetry on the surface of the spherical particle, where the texture of the nematic shell resembles a tennis ball [Fig. 1.1(B)]. Such tetrahedral symmetry was also predicted by Lubensky and Prost who considered a more general model of a closed membrane consisting of p-fold symmetric anisotropic molecules [49]. Note that this thesis focuses on the case of $p = 2$, such as rigid rods and polymer chains.

In addition to the "tennis-ball" conformation of anisotropic molecules confined to a spherical surface, researchers also provided us fresh insights into further controlling the order of this system. As one of the possibilities, when the spherical surface deforms to other geometries, the positions of defects may move on the surface and then produce other symmetries instead of the perfect tetrahedral symmetry.

Within the Landau-de Gennes model, Kralj *et al.* [40] studied the distribution of local orientational order of a uniaxial ellipsoidal nematic shell, where the four $+1/2$ defects move to the north and south poles and even unite to two $+1$ defects for more slender shell, or the four $+1/2$ defects move to the equator for flatter shell (Fig. 1.7). The same system was also investigated by Bates *et al.* [8] using the Lebwohl-Lasher lattice model. The conformation of anisotropic molecules can also be changed by applying an external field [75].

The advantage of the phenomenological continuum model is that, with the help of differential geometry, the free energy of the model can be derived into the expression of defect energy which can be easily handled for further analysis of the conformations. However, the continuum model has its intrinsic weaknesses so that we must consider other models. Such weaknesses include that, for example, the continuum model is no longer convincing when the density of molecules is low. In particular, at low densities the positional and orientational entropies dominate, which drive the system towards a homogeneous and isotropic state. In this case, the vector field $\mathbf{n}(\mathbf{r})$ cannot be defined. Only if the surface density goes beyond a transition density, a nematic field starts to develop in this system. Hence, the continuum model lacks the ability to describe the order-disorder transition of this system.

1.3.3 Rod or chain model

Since we are considering the conformations of rod-like or chain-like molecules, it is desirable to generate a rod or chain model, which contains no phenomenological constants as those assumed in the continuum models, to describe such system. To study these rod or chain models, we can apply analytical theories or conduct Monte Carlo simulations. Note that the density of rods or chains is one of the key parameters determining the macroscopic properties of the rod or chain model. At low surface density, to maximize the orientational and positional entropies, no particular pattern would form by these rods; therefore, the conformation is isotropic and homogeneous. Beyond a transition density, coupled orientational and positional ordering starts to emerge, giving rise to a configurational texture on the spherical

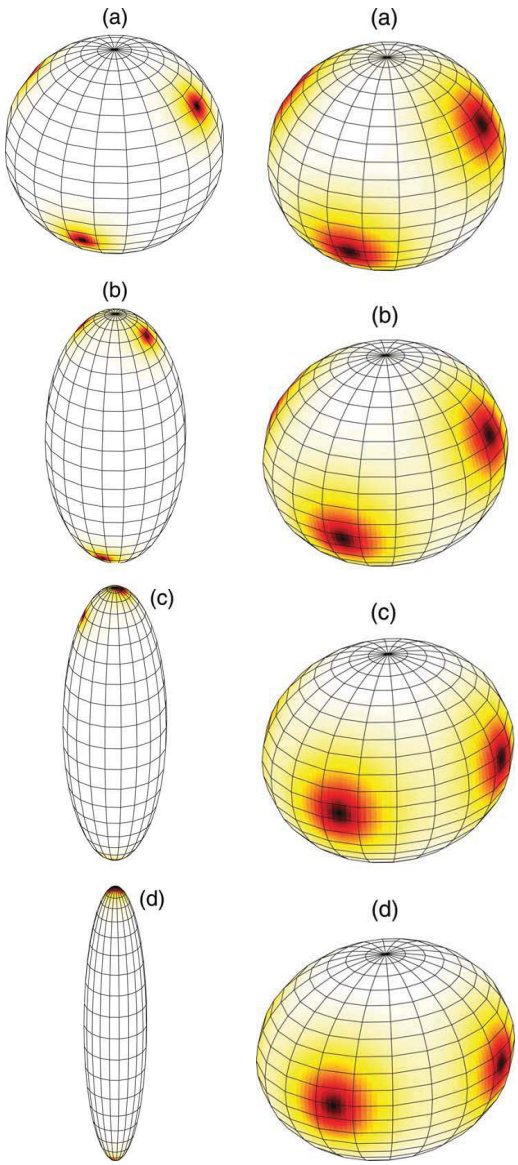

Figure 1.7: (taken from Ref. [40]) For slender uniaxial ellipsoidal shell (left column), the defects move to the poles. For flat uniaxial ellipsoidal shell (right column), the defects move to the equator. Here, the black color means low orientational order where the defect locates.

surface.

Consider the system of rod-like molecules confined to a spherical surface. Although the continuum theory suggests the existence of the tetrahedral tennis-ball conformation, could such configuration exist in the rod model of volume-excluding rigid rods on the spherical surface? Or, even loosely, instead of having four defects located exactly at the vertices of an equal-sided tetrahedron, can a tennis-ball state exists, which can be defined as a structure where the vector joining the two defects near the north pole is perpendicular to the vector joining the other pair near the south pole [Fig. 1.9(A2)]? Recent Monte Carlo simulations of *thin* rods have ruled out the existence of the perfect tetrahedral tennis-ball structure [74, 7]. Instead, other possible defect structures have been suggested. On the basis of a Monte Carlo snapshot, Bates [7] showed a configuration that resembles a tennis-ball texture but is more similar to splay, since the two $+1/2$ defects of each pair on the north and south poles are very close to each other (Fig. 1.8); in another simulation snapshot [7] the vector joining the two defects near the north pole is parallel to the vector joining the other pair near the south pole, four defects forming corners of a rectangle on the xz-plane shown in Fig. 1.9(A3). Shin *et al.* [74] and Bates [7] also suggested the existence of a so-called "cut-and-rotate" splay structure — the pattern resembles cutting a perfect splay state along the north-south pole plan and then rotating one of the hemispheres by an angle about the y-axis shown in Fig. 1.9(A4). None of these Monte Carlo simulations has assessed free energies of these possible configurations and disorder-order transition. For the rod model, it is well known that the competition between the entropic effects and the excluded volume interaction can be transparently reflected by the main ingredients in the Onsager theory [65], which has been used for describing nematic structure of rigid rods in three dimensions [61]. Recently, our research group generalized the free energy expression of Onsager, suitable for a spatially inhomogeneous system on a spherical surface, to study the resulting nematic defect structure and concluded that the only stable state is the splay configuration within the considered parameter range for *thin* rods [92, 93]. The instability of other possible configurations—tennis-ball, rectangle, and cut-and-rotate splay—can also be assessed by means of the Onsager free energies. Fig. 1.9 shows the four possible configurations of rigid rods confined

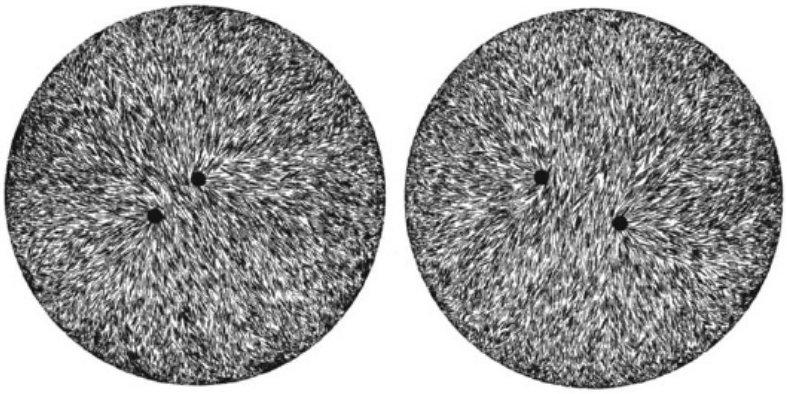

Figure 1.8: (taken from Ref. [7]) Snapshot of Monte Carlo simulation shows two +1/2 defects of each pair on the north and south poles are very close to each other.

to a spherical surface: splay (A1 and B1), tennis-ball (A2 and B2), rectangle (A3 and B3), and cut-and-rotate splay (A4 and B4), where the right column of figures are the maps of orientational entropy fields that will be explained in Chapter 2.

As well, some theoretical studies on the conformation of a polymer chain on a spherical surface were published recently [55, 77, 47, 57, 12, 43, 76, 20]. Considering a Gaussian chain confined on a curved surface, Mondescu and Muthukumar [55] calculated the probability distribution function of the end-to-end vector and the mean-square end-to-end distance. Spakowitz and Wang [77] considered the statistical behavior of a noninteracting wormlike chain confined to a spherical surface; they provided a closed-form expression of the mean-square end-to-end distance for any value of total chain length, persistence length, and sphere radius. Lin *et al.* [47] obtained some numerical solutions of polymer conformations with local geometrical quantities on cylindrical and ellipsoidal surfaces based on the principle of minimization of bend energy. By applying the mean field theory to a noninteracting wormlike chain confined on a spherical surface or in the interior of a sphere, Morrison and Thirumalai [57] found highly wrapping conformation due to the stiffness of the chain and the confinement of the sphere. Some other works [12, 43] also supported the wrapping conformation by means of computer simulations. Moreover, if incorporating the excluded volume interaction in the semiflexible chains, the wrapping conformation could have more complicated symmetry with some fine

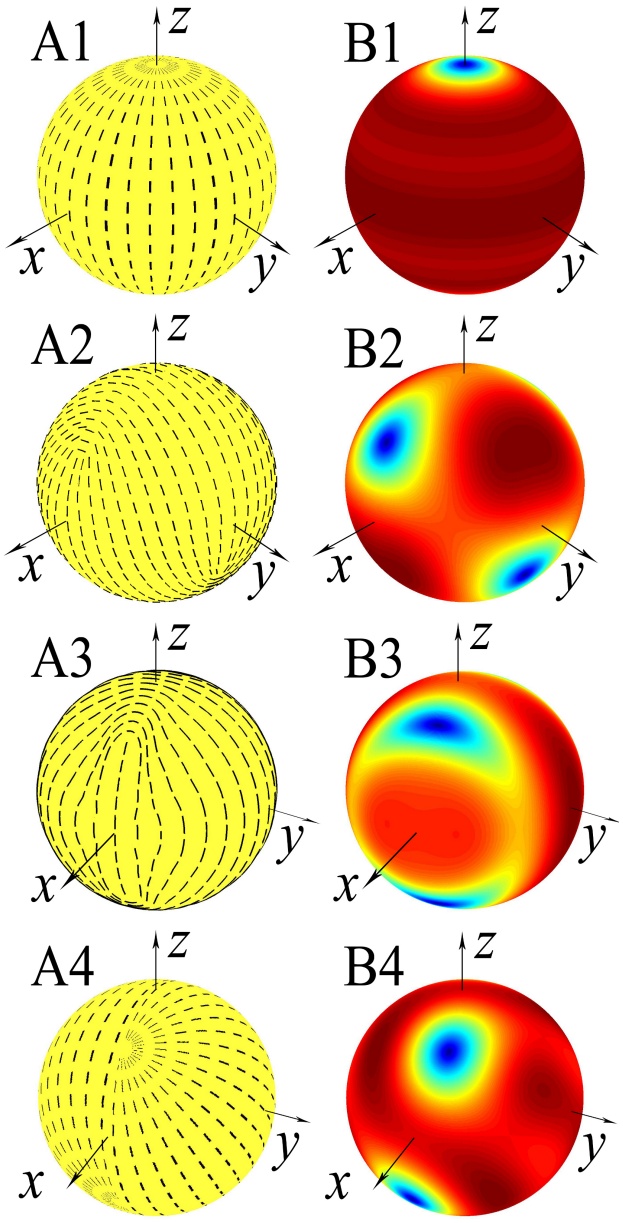

Figure 1.9: Four possible configurations are considered in this work: splay (A1 and B1), tennis-ball (A2 and B2), rectangle (A3 and B3), and cut-and-rotate splay (A4 and B4). Plots B1-B4 represent distribution maps of orientational entropy fields that are produced according to the procedure explained in Chapter 2.

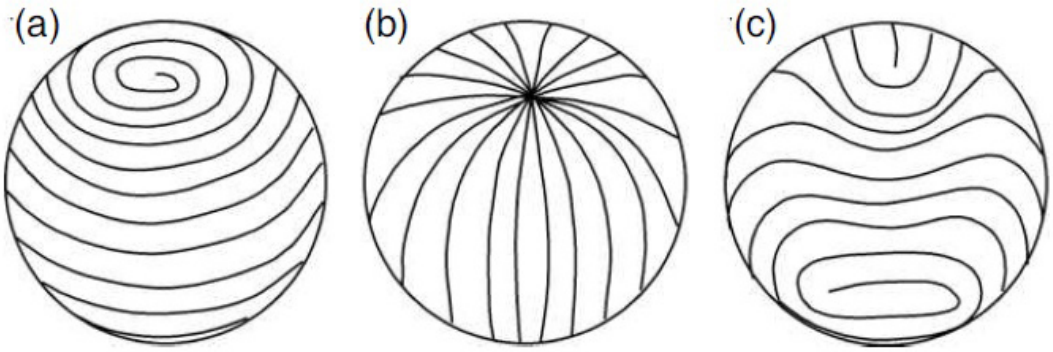

Figure 1.10: (taken from Ref. [20]) Three possible conformations may exist for a polymer confined on a spherical surface: helicoidal (a), splay (b), and tennis-ball (c), where the splay conformation is forbidden if the polymer chain has the excluded volume interaction.

structures. By minimizing the energy of a linear chain of charges confined on a spherical surface, Slosar and Podgornik [76] observed a helical symmetry of charge distribution wound around the surface of the sphere. Indeed, similar to the splay conformation of rods on a spherical surface, one can imagine a helicoidal conformation for a self-avoiding polymer chain on a spherical surface [Fig. 1.10(a)]. Of course, for a semiflexible polymer chain, the helicoidal conformation is not the only option. Each +1 defect on either north or south pole of the helicoidal conformation can be stretched into two +1/2 defects, and the four +1/2 defects locate on the four vertices of a tetrahedron. This is the tennis-ball conformation for a polymer chain on a spherical surface [Fig. 1.10.(c)]. By means of Monte Carlo simulations on a semiflexible polymer chain confined on a spherical surface, Angelescu *et al.* [20] confirmed that the tennis-ball state could *not* exist for neutral chains but can be observed for charged chains. However, this conclusion does conflict with the continuum theory which doesn't depend on any static electric interaction. Recently, our group conducted Monte Carlo simulations on the neutral semiflexible polymer chain confined on a spherical surface and confirmed that the ordered state always accompanies the tennis-ball symmetry [91].

1.4 Present Work and Organization of the Thesis

For the purpose of studying the conformations of anisotropic molecules confined on a spherical surface, the thesis will discuss the conformation of rods in Chapter 2, a long wormlike chain in Chapter 3, and many semiflexible chains in Chapter 3. Finally, the summary and outlook for this topic are concluded in Chapter 5.

In Chapter 2, a system of self-avoiding hard rods is investigated on the basis of a generalized Onsager model, which allows us to write the free energy as a functional of the density distribution (which is a function of spatial and orientational variables). The numerical solution of the model indicates that the splay state, where on average rods line up in parallel to the longitudinal lines on the spherical surface, is the only stable state. Although they can be enforced by numerical tricks, tennis-ball, rectangle, and cut-and-rotate splay configurations all yield higher free energy than that of a ground splay state. We also predict that the disorder-splay transition has first-order characteristics.

In Chapter 3, using Monte Carlo simulations of a wormlike chain that contains the excluded-volume interaction, it is demonstrated that a directionally anisotropic state exists at high surface coverage, when the chain is confined to a spherical surface. The isotropic-anisotropic transition has first-order phase-transition characteristics and can be compared with the isotropic-nematic transition observed in lyotropic polymer systems, both driven by the excluded-volume interaction. Unlike a bulk nematic state, the anisotropic state of polymer-segment orientations observed here always couples with positional ordering, displaying the so-called tennis-ball texture.

In Chapter 4, we discussed a system of semiflexible chains confined to a spherical surface with two approaches — Monte Carlo simulation and Onsager model. The former demonstrates that, if the persistence length of each chain is comparable to its contour length, the system displays a perfect tetrahedral tennis-ball configuration, which has never been encountered for the system of rigid rods discussed in Chapter 2 or the system of a long wormlike chain studied in Chapter 3. The numerical solution of Onsager model is fully prepared in mathematics, but not finished in this thesis.

Chapter 2

Onsager Model for the Structure of Rigid Rods Confined on a Spherical Surface

2.1 Introduction

Consider the system where N rod-like particles of length ℓ, interacting with each other through the excluded-volume interaction, are confined on a spherical surface of radius R. This model belongs to a class of recently studied systems that points to the existence of the 4-fold tetrahedral symmetry [58, 31, 25, 48]. Such structure breaks the azimuthal symmetry of a splay distribution, shown in Fig. 1.9(A1), and contains four $+1/2$ defects appearing at the vertices of a tetrahedron on the spherical surface, shown in Fig. 1.9(A2), two on the xz-plane near the north pole and two on the yz-plane near the south pole. Note that the vector joining the two defects near the north pole is perpendicular to the vector joining the other pair near the south pole [Fig. 1.9(A2)]. However, recent Monte Carlo simulations of *thin* rods confined on a spherical surface have ruled out the existence of the perfect tetrahedral tennis-ball structure in this system. Instead, the rectangle conformation [7] and "cut-and-rotate" splay [7, 74] have been suggested. For the rectangle conformation, the four $+1/2$ defects appear on the vertices of a rectangle on the

xz-plane [Fig. 1.9(A3)]. The cut-and-rotate splay resembles cutting a perfect splay state along the north-south pole plan and then rotating one of the hemispheres by an angle about the y-axis shown in Fig. 1.9(A4).

In this chapter, we consider numerical solutions of a free-energy model, generalizing the Onsager interaction between rod-like particles on a spherical surface. It has been well accepted that Onsager theory is capable of describing nematic structures of rigid rods [65], including spatially inhomogeneous systems [17, 14, 32] where orientational degrees of freedom are coupled with positional degrees of freedom in the free energy expression. We aim at finding an exact solution of the free energy functional [Sect. 2.2] in the Onsager model using a multiple-variable approach [Sect. 2.3], so that the free energy can be minimized with no ambiguous approximations. Incorporating the symmetric properties of the splay, tennis-ball, rectangle, and cut-and-rotate splay configurations, we can also enforce the system to each individual symmetry for the purpose to search for the possible existence of these different states. One of the main results from this exercise is that the global minimum of the free energy corresponds to only one state, namely the splay state [Sect. 2.4.1-4]. Within the a wide range of the searched parameter space, tennis-ball, rectangle, and cut-and-rotate splay configurations do not correspond to a free energy minimum. Furthermore, we defined the orientational and positional order parameters that can be used to characterize the physical properties near the disorder-splay transition point [Sect. 2.4.5], and found that the nature of the transition is first order, within the current mean-field approach [Sect. 2.4.6], which is also supported by the bifurcation analysis [Sect. 2.4.7].

2.2 Free Energy Functional of Onsager Model

We consider a system of N rigid "rods" which are embedded on the surface of a sphere of radius R. Because straight rods cannot be completely confined on a curved surface, here we use the model that each rod is a curved geodesic segment of length ℓ, which is an arc portion of the so-called great circle whose radius equals the radius R of the sphere. These rod particles interact with each other through an excluded-volume interaction. Note that on a two-dimensional surface, the excluded volume actually manifests itself in the form of an excluded area, which always exists even for extremely small, vanishing rod radius to length ratio. In this thesis it is assumed that rods have no thickness D, which can be considered as an approximation for actual systems having small D/ℓ.

In his classical work [65], Onsager developed a free-energy functional for the three-dimensional, spatially homogeneous system of rigid rods interacting with each other through excluded volume interactions, as a functional of the density distribution function. His approach can be easily generalized to write down the free energy of the current system, now including both spatial and orientational dependencies,

$$\beta F = \int \varrho(\mathbf{r},\mathbf{u}) \ln\left[8\pi^2 R^2 \varrho(\mathbf{r},\mathbf{u})\right] \, \mathrm{d}\mathbf{r}\mathrm{d}\mathbf{u} + \frac{1}{2}\int \varrho(\mathbf{r},\mathbf{u}) w(\mathbf{r},\mathbf{u},\mathbf{r}',\mathbf{u}') \varrho(\mathbf{r}',\mathbf{u}') \, \mathrm{d}\mathbf{r}\mathrm{d}\mathbf{u}\mathrm{d}\mathbf{r}'\mathrm{d}\mathbf{u}', \quad (2.1)$$

where $\beta = 1/k_B T$. In the above, we have assumed a density distribution function, $\varrho(\mathbf{r},\mathbf{u})$, where $\mathbf{r}$ and $\mathbf{u}$ are the position vector and tangent unit vector, respectively, of the center of mass of a rod. The free energy as a functional of $\varrho(\mathbf{r},\mathbf{u})$ needs to be minimized; the result is the stable-state distribution function for the system. The first term arises from both orientational and translational entropies, where a linear term $\varrho(\mathbf{r},\mathbf{u}) \ln 8\pi^2 R^2$ has been added which does not affect the structure of the current theory. The second term contains a function $w(\mathbf{r},\mathbf{u},\mathbf{r}',\mathbf{u}')$ that depends on variables $(\mathbf{r},\mathbf{u})$ and $(\mathbf{r}',\mathbf{u}')$, which represent the coordinates of the centers of mass of two rods; this function takes a value 1 if any parts of the two rods overlap and 0 otherwise [17]. Although only accurate at the level of the second-virial approximation, the competition between the entropy and the excluded-volume

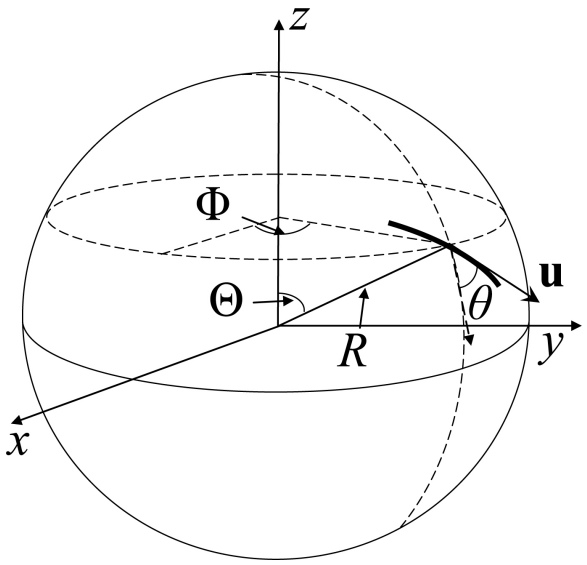

Figure 2.1: After the coordinate system is chosen, the location of a rod is given by the polar angle Θ and azimuthal angle Φ, and the orientation of the rod by the angle between the tangent vector $\mathbf{u}$ and the longitudinal line.

terms captures the important physics in most systems involving rigid rods, such as the isotropic-nematic liquid-crystal phase transition [65, 33], the isotropic-nematic interface [29, 56, 51, 36, 17, 14, 38], and nematic rods near a hard wall surface [68, 67, 83].

To proceed further we adopt a spherical-coordinate system to specify the position $\mathbf{r}$ of the center of mass of a rod by the polar and azimuthal variables, Θ and Φ, shown in Fig. 2.1. The orientation of a rod is described by θ, the angle which $\mathbf{u}$ makes with respect to the local longitudinal direction passing through the center of mass (Fig. 2.1). The free energy can be rewritten as,

$$\beta F = R^2 \int \varrho(\Theta,\Phi;\theta) \ln\left[8\pi^2 R^2 \varrho(\Theta,\Phi;\theta)\right] \sin\Theta \mathrm{d}\Theta\mathrm{d}\Phi\mathrm{d}\theta$$
$$+ \frac{R^4}{2} \int \varrho(\Theta,\Phi;\theta) w(\Theta,\Phi,\theta,\Theta',\Phi',\theta') \varrho(\Theta',\Phi';\theta') \sin\Theta \sin\Theta' \mathrm{d}\Theta\mathrm{d}\Phi\mathrm{d}\theta\mathrm{d}\Theta'\mathrm{d}\Phi'\mathrm{d}\theta'. \tag{2.2}$$

The density distribution function $\varrho(\Theta, \Phi; \theta)$ satisfies the normalization condition,

$$R^2 \int \varrho(\Theta, \Phi; \theta) \sin\Theta \mathrm{d}\Theta \mathrm{d}\Phi \mathrm{d}\theta = N, \tag{2.3}$$

where N is the total number of rods in the system. Furthermore, we introduce the probability distribution function

$$f(\Theta, \Phi; \theta) \equiv R^2 \varrho(\Theta, \Phi; \theta)/N, \tag{2.4}$$

which can be interpreted as the probability for finding the center of mass of a rod at the position described by (Θ, Φ) and with an orientation represented by θ. The function $f(\Theta, \Phi; \theta)$ is now normalized to

$$\int f(\Theta, \Phi; \theta) \sin\Theta \mathrm{d}\Theta \mathrm{d}\Phi \mathrm{d}\theta = 1. \tag{2.5}$$

As a functional of the probability distribution function $f(\Theta, \Phi; \theta)$, the free energy can be rewritten as,

$$\begin{aligned} \beta F = N \ln N + N \int f(\Theta, \Phi; \theta) \ln \left[8\pi^2 f(\Theta, \Phi; \theta)\right] \sin\Theta \mathrm{d}\Theta \mathrm{d}\Phi \mathrm{d}\theta \\ + \frac{N^2}{2} \int f(\Theta, \Phi; \theta) w(\Theta, \Phi, \theta, \Theta', \Phi', \theta') f(\Theta', \Phi'; \theta') \sin\Theta \sin\Theta' \mathrm{d}\Theta \mathrm{d}\Phi \mathrm{d}\theta \mathrm{d}\Theta' \mathrm{d}\Phi' \mathrm{d}\theta'. \end{aligned} \tag{2.6}$$

The equilibrium state of the model can be found from a minimization of F with respect to $f(\Theta, \Phi; \theta)$.

The function $w(\Theta_1, \Phi_1, \theta_1, \Theta_2, \Phi_2, \theta_2)$ contains six variables and can be defined by using basic relations between the variables associated with two interacting rods. The orientation vector $\mathbf{u}_i$ and center-of-mass vector $\mathbf{r}_i$ of rod i, where $i = 1$ and 2, can be written as $\mathbf{u}_i = \cos\theta_i \hat{\mathbf{\Theta}}_i + \sin\theta_i \hat{\mathbf{\Phi}}_i$ and $\mathbf{r}_i = R\hat{\mathbf{R}}_i$, where $\hat{\mathbf{R}}$, $\hat{\mathbf{\Theta}}$, and $\hat{\mathbf{\Phi}}$ are unit vectors of the spherical-coordinate system. In this way we can define the normal to the great-circle plane for a particle located at $\mathbf{r}_i$, $\mathbf{n}_i = \mathbf{r}_i \times \mathbf{u}_i$.The direction from the sphere's center to the intersection point of two great circles on the sphere's surface is a vector that can be represented by $\mathbf{j} = \mathbf{n}_1 \times \mathbf{n}_2 / |\mathbf{n}_1 \times \mathbf{n}_2|$.

Based on these vector relationships the function w can be easily evaluated,

$$w(\Theta_1, \Phi_1, \theta_1, \Theta_2, \Phi_2, \theta_2) = \begin{cases} 1, & \text{if } \mathbf{j} \cdot \hat{\mathbf{R}}_i > \cos(\ell/2R) \\ & \quad \text{for both } i = 1 \text{ and } 2, \\ & \text{or } \mathbf{j} \cdot \hat{\mathbf{R}}_i < -\cos(\ell/2R) \\ & \quad \text{for both } i = 1 \text{ and } 2, \\ 0, & \text{otherwise.} \end{cases} \tag{2.7}$$

The above is a function of ℓ/R only for geodesic rods considered here. The leading correction for rods of finite D/ℓ can also be written in a similar expression, but we focus on the case of $D/\ell = 0$ here.

In order to minimize the free energy, computationally we could represent the function in question, $f(\Theta, \Phi; \theta)$, by direct discretization of all three involved variables. Such discretization was considered previously for similar rod systems where two or three variables were involved [17, 14]. Because of the large number of independent variables needed to numerically represent $f(\Theta, \Phi; \theta)$ with high precision, other numerical tricks were required. In this thesis we take an expansion of $f(\Theta, \Phi; \theta)$ in terms of orthonormal basis functions, adjusting expansion coefficients to minimize the free energy.

2.3 Numerical Approach

In this thesis, the distribution function $f(\Theta, \Phi; \theta)$ is expanded in terms of orthonormal basis functions, with expansion coefficients adjusted to minimize the free energy. In particular we use the basis function,

$$\psi_{lmn}(\Theta, \Phi; \theta) = Y_{lm}(\Theta, \Phi) U_n(\theta), \tag{2.8}$$

as a combination of the spherical harmonics $Y_{lm}(\Theta, \Phi)$ and Fourier bases $U_n(\theta)$, all written as real functions (see Appendix A). The basis functions, each of which has three indexes l, m, and n, follow the orthonormal condition,

$$\int \psi_{lmn}(\Theta, \Phi; \theta) \psi_{l'm'n'}(\Theta, \Phi; \theta) \sin\Theta \mathrm{d}\Theta \mathrm{d}\Phi \mathrm{d}\theta = \delta_{ll'} \delta_{mm'} \delta_{nn'}, \tag{2.9}$$

where δ_{ij} is the Kronecker delta.

The function w can be then expanded in terms of the orthonormal bases,

$$w(\Theta, \Phi, \theta, \Theta', \Phi', \theta') = \frac{\ell^2}{4\pi R^2} \sum_{lmn, l'm'n'} \psi_{lmn}(\Theta, \Phi; \theta) W_{lmn,l'm'n'} \psi_{l'm'n'}(\Theta', \Phi'; \theta'). \tag{2.10}$$

At a given value of ℓ/R, the constant matrix, $W_{lmn,l'm'n'}$, can be evaluated according to

$$W_{lmn,l'm'n'} = \frac{4\pi R^2}{\ell^2} \int \psi_{lmn}(\Theta, \Phi; \theta) w(\Theta, \Phi, \theta, \Theta', \Phi', \theta') \cdot \psi_{l'm'n'}(\Theta', \Phi'; \theta') \sin\Theta \sin\Theta' \mathrm{d}\Theta \mathrm{d}\Phi \mathrm{d}\theta \mathrm{d}\Theta' \mathrm{d}\Phi' \mathrm{d}\theta'. \tag{2.11}$$

A constant, $4\pi R^2/\ell^2$, has been factored out in the above to properly account for the magnitude of the excluded volume. The integral part of (2.11) contains further ℓ/R-dependence through the expression in (2.7). Numerically, $W_{i,i'}$ is evaluated by means of Simpson's approximation, at an integration step $\ell/36R$ for Θ and Φ and $\pi/36$ for θ; the results were stored as a constant matrix before further computation takes place.

The unknown function, f, can then be expressed in terms of unknown coefficients ϕ_{lmn} in the expansion,

$$f(\Theta, \Phi; \theta) = \sum_{lmn} \phi_{lmn} \psi_{lmn}(\Theta, \Phi; \theta). \tag{2.12}$$

The normalization condition, (2.5), can be directly used to determine the coefficient of the leading basis function, labeled $(l, m, n) = (0, 0, 0)$,

$$\psi_{000} = 1\Big/\sqrt{8\pi^2}, \tag{2.13}$$

which gives

$$\phi_{000} = 1\Big/\sqrt{8\pi^2}. \tag{2.14}$$

The free energy can then be treated as a function of multiple variables, all ϕ_{lmn} other than ϕ_{000}, in this search for the free energy minimum,

$$\begin{aligned}\beta F = N\ln N + N\int f(\Theta,\Phi;\theta)\ln\left[8\pi^2 f(\Theta,\Phi;\theta)\right]\sin\Theta \mathrm{d}\Theta\mathrm{d}\Phi\mathrm{d}\theta \\ + \frac{N^2\ell^2}{8\pi R^2}\sum_{lmn,l'm'n'}\phi_{lmn}W_{lmn,l'm'n'}\phi_{l'm'n'}.\end{aligned} \tag{2.15}$$

The isotropic state is characterized by a constant density distribution. The expansions considered here yield a free energy for the isotropic state,

$$\beta F_0 = N\ln N + \frac{N^2\ell^2}{8\pi R^2}W_{000,000}\phi_{000}^2. \tag{2.16}$$

We can then write the reduced free-energy difference per particle,

$$\begin{aligned}\tilde{f} =& (\beta F - \beta F_0)/N \\ =& \int f(\Theta,\Phi;\theta)\ln\left[8\pi^2 f(\Theta,\Phi;\theta)\right]\sin\Theta\mathrm{d}\Theta\mathrm{d}\Phi\mathrm{d}\theta \\ &+ \frac{\rho\ell^2}{2}\sum_{lmn,l'm'n'}{}'\ \phi_{lmn}W_{lmn,l'm'n'}\phi_{l'm'n'},\end{aligned} \tag{2.17}$$

where the summation $\sum'$ runs taken over all (l, m, n) and (l', m', n') except for the $(l, m, n) = (l', m', n') = (0, 0, 0)$ terms. Beyond ϕ_{lmn}, the system contains two parameters, the length-to-radius ratio ℓ/R through the W matrix and the reduced density

$$\rho\ell^2 = \frac{N\ell^2}{4\pi R^2} \tag{2.18}$$

as the coefficient of the second term in (2.17). For each set of specified parameters, ℓ/R and $\rho\ell^2$, we attack the minimization problem, by treating $\tilde{f}$ as a multi-variable function of ϕ_{lmn}, where $(l, m, n) \neq (0, 0, 0)$.

In the actual computation, we further took advantage of the symmetry properties listed in Appendix B to reduce the number of unknown variables, ϕ_{lmn}. We approximated the expansion by neglecting terms having indexes $l = 8$, $n = 8$ and higher. The expansions including terms with index $l = 8$ and $n = 8$ were also considered; although the minimized free energies were a little shifted, the results discussed in next section would not be changed at all. For the purpose to save computational time, we focused on the expansions with indexed up to 6. This means that there are 16, 46, 47, and 91 bases needed to describe the splay, tennis-ball, rectangle, and cut-and-rotate splay states, respectively. The numerical error of ignoring higher order terms are negligible, within the precision of required calculation.

The computational task for conducting the search of the free energy minimum relies on an implementation of the Broyden-Fletcher-Goldfarb-Shanno (BFGS) algorithm explained in Ref. [26]. BFGS is a quasi-Newton method, which searches for a stationary point of a multi-variable function starting from an initial guess iteratively. At each step, BFGS method determines a search direction from the gradient and uses the approximation of the Hessian matrix to find the next point. The stationary point is located until the gradient converges to zero. At every search step, the value of the function to be minimized, (2.17), and its gradient,

$$\begin{aligned} G_{lmn} \equiv & \frac{\partial \tilde{f}}{\partial \phi_{lmn}} \\ = & \int \left\{ 1 + \ln \left[8\pi^2 f(\Theta, \Phi; \theta) \right] \right\} \psi_{lmn}(\Theta, \Phi; \theta) \sin \Theta \mathrm{d}\Theta \mathrm{d}\Phi \mathrm{d}\theta \\ & + \rho \ell^2 \sum_{l'm'n'} W_{lmn,l'm'n'} \phi_{l'm'n'}, \end{aligned} \tag{2.19}$$

must be provided.

While the computational task of the W-related terms in both Eqs. (2.17) and (2.19) can be performed efficiently by taking summations, the integration in terms related to $\ln f(\Theta, \Phi; \theta)$ in both expressions is not straightforward and most numerically expensive. For a given set ϕ_i, we evaluated the entire function $f(\Theta, \Phi; \theta)$ from the expansion, (2.12), and treated these integrations involving logarithmic terms taking a numerical integration based on Simpson's rule.

2.4 Results

2.4.1 Free-energy minimum

The model system that we are considering can be characterized by the length of the rod, ℓ, the radius of confining sphere R, and the number of particles N. Out of these parameters, from a scaling point of view, only two reduced parameters are important, ℓ/R, and the reduced surface density, $\rho\ell^2$ in (2.18). Indeed, the reduced free energy, (2.17), contains these reduced parameters. The results discussed in this section are presented as a function of $\rho\ell^2$, with selected ℓ/R in the range $[0.1, 1]$.

The solid curves in Figs. 2.2-2.11 represent the minimized free energy obtained from the numerical minimization for $\ell/R = 0.1$, 0,2, ..., 1, all corresponding to the ground-state splay conformation. The number of independent ϕ_{lmn} in the expansion (2.17) varies according to the underlying symmetry properties listed in Appendix B. Because the splay conformation has a higher symmetry than the other three, splay terms which exist in a splay configuration are also common in the expansions of the free energies for other three types of configurations. For every given system, we have employed four different processes of conducting the minimization search. Each process corresponds to a study of a particular type of conformation; we directly search for the free-energy minimum of this conformation by varying the undetermined coefficients of all relevant terms and removing all other terms that violate the symmetry properties of such a state. By the end of the search, all four processes converge to one single result: in the expansion of f (Eq. 2.12), only the coefficients ϕ_{lmn} of the splay terms are significantly present and coefficients ϕ_{lmn} of the non splay terms vanish. Therefore, within the range of parameter space studied and within the validity of the Onsager model, we find that the splay conformation is the only stable conformation.

In order to dissect the structures associated with the non-splay conformations, we took another approach in this numerical study. From the symmetry of the expansion, we can see that each non-splay conformation is characterized by a leading term in the free-energy expansion, tennis-ball state by the $(l, m, n) = (3, 2, 0)$ term, rectangle state by the $(2, 2, 0)$ term, and cut-and-rotate splay state by the $(3, -2, 0)$

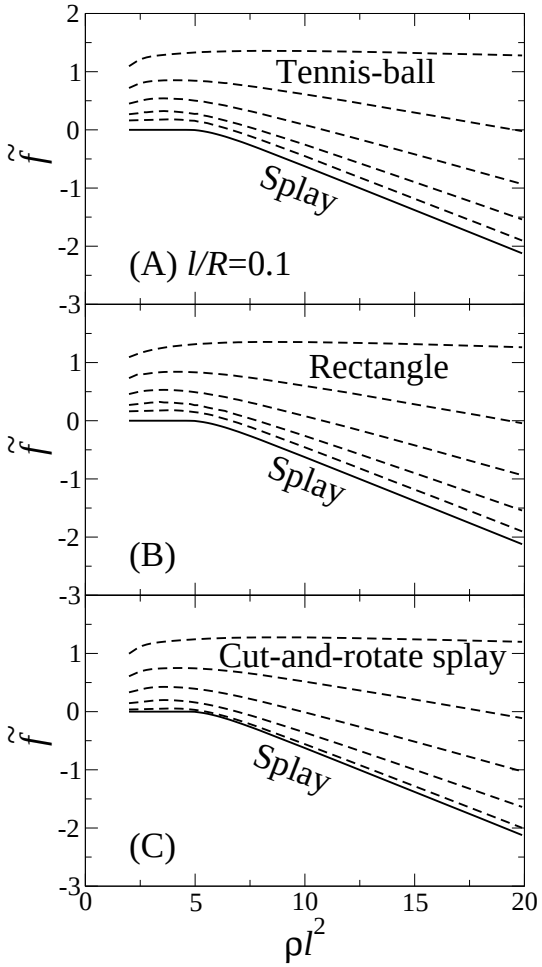

Figure 2.2: Minimized free energy plotted as a function of reduced density $\rho\ell^2$ for $\ell/R = 0.1$. Fig. (A) show the free energies of the splay states (solid curve) and the tennis-ball states (dashed curves) with leading term coefficient fixed at -0.1 -0.08, -0.06, -0.04, and -0.02 from the top to bottom curves. Fig. (B) show the free energies of the splay states(solid curve) and the rectangle states (dashed curves) with leading term coefficient fixed at 0.1 0.08, 0.06, 0.04, and 0.02 from the top to bottom curves. Fig. (C) show the free energies of the splay states (solid curve) and the cut-and-rotate splay states (dashed curves) with leading term coefficient fixed at 0.1 0.08, 0.06, 0.04, and 0.02 from the top to bottom curves.

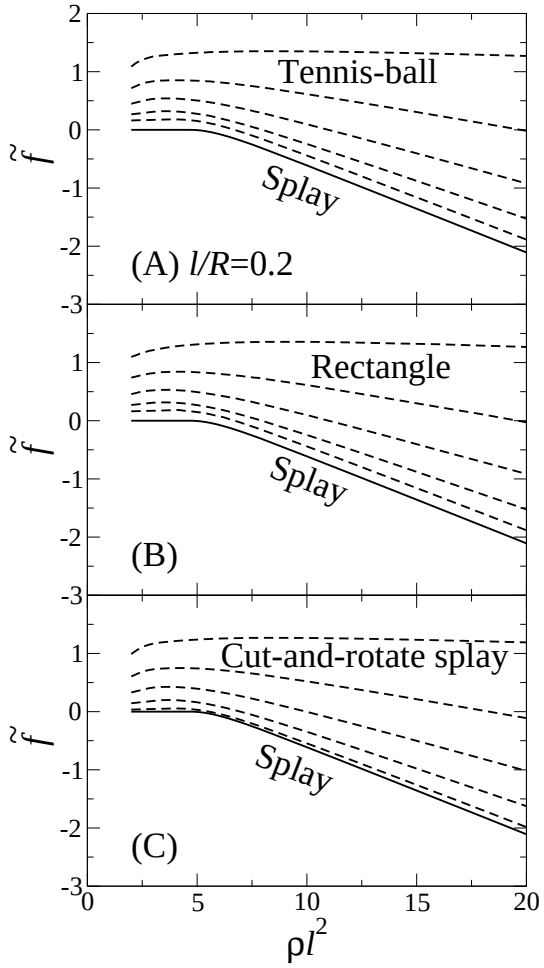

Figure 2.3: Minimized free energy plotted as a function of reduced density $\rho\ell^2$ for $\ell/R = 0.2$. Fig. (A) show the free energies of the splay states (solid curve) and the tennis-ball states (dashed curves) with leading term coefficient fixed at -0.1 -0.08, -0.06, -0.04, and -0.02 from the top to bottom curves. Fig. (B) show the free energies of the splay states(solid curve) and the rectangle states (dashed curves) with leading term coefficient fixed at 0.1 0.08, 0.06, 0.04, and 0.02 from the top to bottom curves. Fig. (C) show the free energies of the splay states (solid curve) and the cut-and-rotate splay states (dashed curves) with leading term coefficient fixed at 0.1 0.08, 0.06, 0.04, and 0.02 from the top to bottom curves.

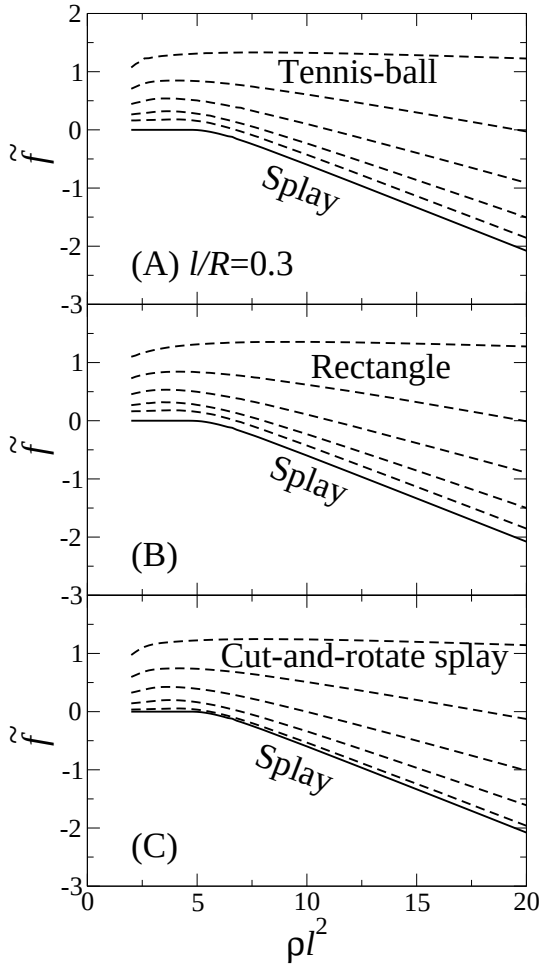

Figure 2.4: Minimized free energy plotted as a function of reduced density $\rho\ell^2$ for $\ell/R = 0.3$. Fig. (A) show the free energies of the splay states (solid curve) and the tennis-ball states (dashed curves) with leading term coefficient fixed at -0.1 -0.08, -0.06, -0.04, and -0.02 from the top to bottom curves. Fig. (B) show the free energies of the splay states(solid curve) and the rectangle states (dashed curves) with leading term coefficient fixed at 0.1 0.08, 0.06, 0.04, and 0.02 from the top to bottom curves. Fig. (C) show the free energies of the splay states (solid curve) and the cut-and-rotate splay states (dashed curves) with leading term coefficient fixed at 0.1 0.08, 0.06, 0.04, and 0.02 from the top to bottom curves.

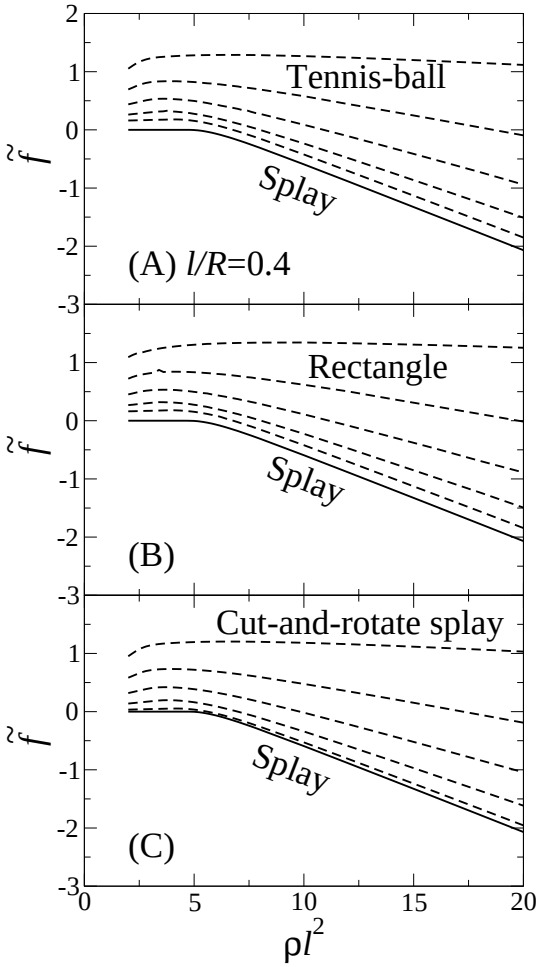

Figure 2.5: Minimized free energy plotted as a function of reduced density $\rho\ell^2$ for $\ell/R = 0.4$. Fig. (A) show the free energies of the splay states (solid curve) and the tennis-ball states (dashed curves) with leading term coefficient fixed at -0.1 -0.08, -0.06, -0.04, and -0.02 from the top to bottom curves. Fig. (B) show the free energies of the splay states(solid curve) and the rectangle states (dashed curves) with leading term coefficient fixed at 0.1 0.08, 0.06, 0.04, and 0.02 from the top to bottom curves. Fig. (C) show the free energies of the splay states (solid curve) and the cut-and-rotate splay states (dashed curves) with leading term coefficient fixed at 0.1 0.08, 0.06, 0.04, and 0.02 from the top to bottom curves.

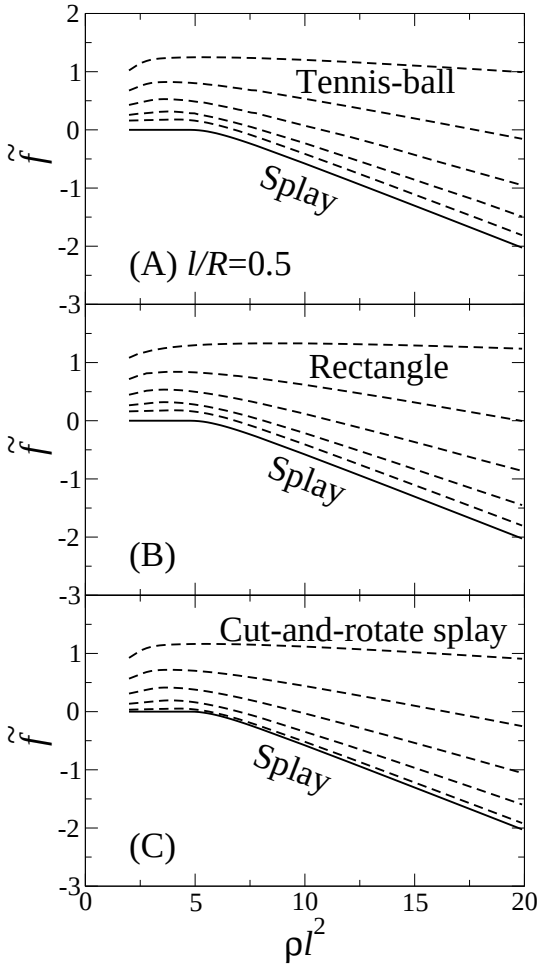

Figure 2.6: Minimized free energy plotted as a function of reduced density $\rho\ell^2$ for $\ell/R = 0.5$. Fig. (A) show the free energies of the splay states (solid curve) and the tennis-ball states (dashed curves) with leading term coefficient fixed at -0.1 -0.08, -0.06, -0.04, and -0.02 from the top to bottom curves. Fig. (B) show the free energies of the splay states(solid curve) and the rectangle states (dashed curves) with leading term coefficient fixed at 0.1 0.08, 0.06, 0.04, and 0.02 from the top to bottom curves. Fig. (C) show the free energies of the splay states (solid curve) and the cut-and-rotate splay states (dashed curves) with leading term coefficient fixed at 0.1 0.08, 0.06, 0.04, and 0.02 from the top to bottom curves.

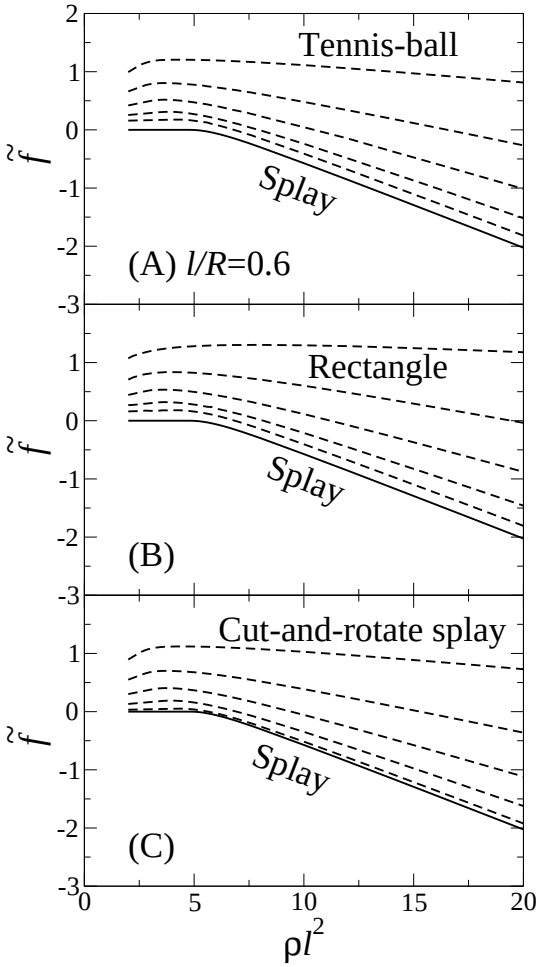

Figure 2.7: Minimized free energy plotted as a function of reduced density $\rho\ell^2$ for $\ell/R = 0.6$. Fig. (A) show the free energies of the splay states (solid curve) and the tennis-ball states (dashed curves) with leading term coefficient fixed at -0.1 -0.08, -0.06, -0.04, and -0.02 from the top to bottom curves. Fig. (B) show the free energies of the splay states(solid curve) and the rectangle states (dashed curves) with leading term coefficient fixed at 0.1 0.08, 0.06, 0.04, and 0.02 from the top to bottom curves. Fig. (C) show the free energies of the splay states (solid curve) and the cut-and-rotate splay states (dashed curves) with leading term coefficient fixed at 0.1 0.08, 0.06, 0.04, and 0.02 from the top to bottom curves.

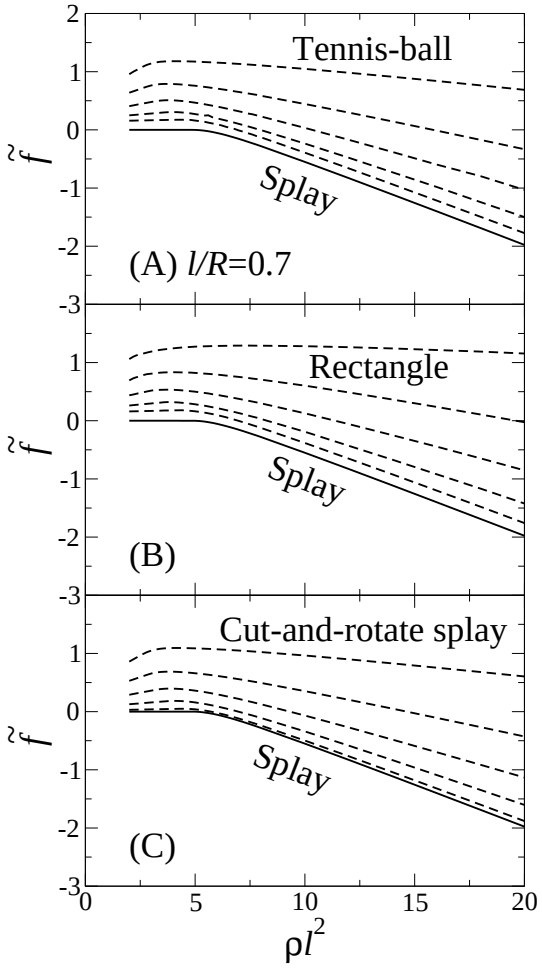

Figure 2.8: Minimized free energy plotted as a function of reduced density $\rho\ell^2$ for $\ell/R = 0.7$. Fig. (A) show the free energies of the splay states (solid curve) and the tennis-ball states (dashed curves) with leading term coefficient fixed at -0.1 -0.08, -0.06, -0.04, and -0.02 from the top to bottom curves. Fig. (B) show the free energies of the splay states(solid curve) and the rectangle states (dashed curves) with leading term coefficient fixed at 0.1 0.08, 0.06, 0.04, and 0.02 from the top to bottom curves. Fig. (C) show the free energies of the splay states (solid curve) and the cut-and-rotate splay states (dashed curves) with leading term coefficient fixed at 0.1 0.08, 0.06, 0.04, and 0.02 from the top to bottom curves.

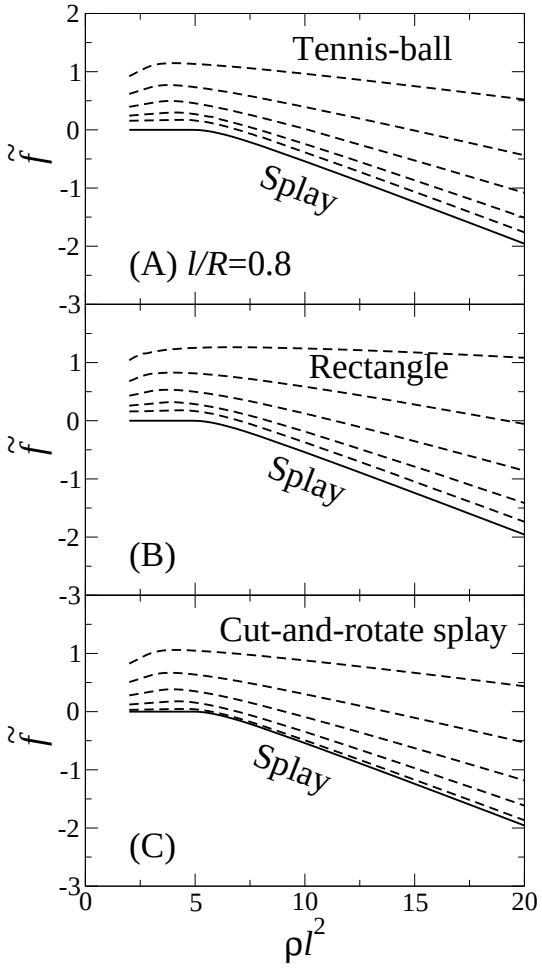

Figure 2.9: Minimized free energy plotted as a function of reduced density $\rho\ell^2$ for $\ell/R = 0.8$. Fig. (A) show the free energies of the splay states (solid curve) and the tennis-ball states (dashed curves) with leading term coefficient fixed at -0.1 -0.08, -0.06, -0.04, and -0.02 from the top to bottom curves. Fig. (B) show the free energies of the splay states(solid curve) and the rectangle states (dashed curves) with leading term coefficient fixed at 0.1 0.08, 0.06, 0.04, and 0.02 from the top to bottom curves. Fig. (C) show the free energies of the splay states (solid curve) and the cut-and-rotate splay states (dashed curves) with leading term coefficient fixed at 0.1 0.08, 0.06, 0.04, and 0.02 from the top to bottom curves.

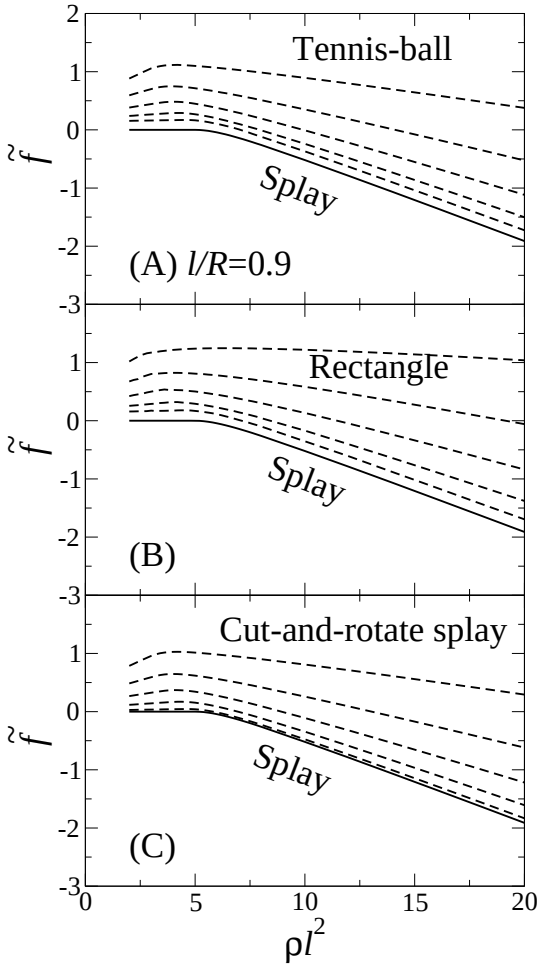

Figure 2.10: Minimized free energy plotted as a function of reduced density $\rho\ell^2$ for $\ell/R = 0.9$. Fig. (A) show the free energies of the splay states (solid curve) and the tennis-ball states (dashed curves) with leading term coefficient fixed at -0.1 -0.08, -0.06, -0.04, and -0.02 from the top to bottom curves. Fig. (B) show the free energies of the splay states(solid curve) and the rectangle states (dashed curves) with leading term coefficient fixed at 0.1 0.08, 0.06, 0.04, and 0.02 from the top to bottom curves. Fig. (C) show the free energies of the splay states (solid curve) and the cut-and-rotate splay states (dashed curves) with leading term coefficient fixed at 0.1 0.08, 0.06, 0.04, and 0.02 from the top to bottom curves.

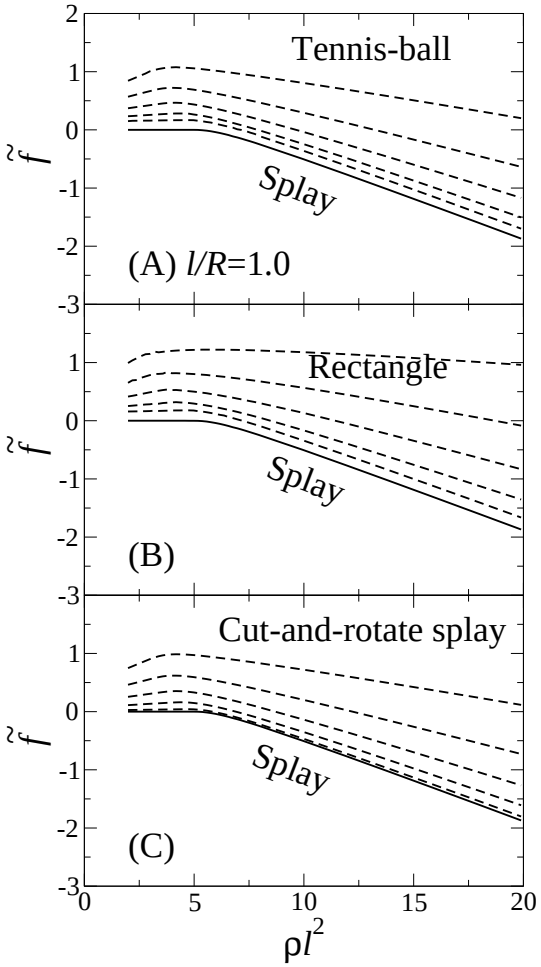

Figure 2.11: Minimized free energy plotted as a function of reduced density $\rho\ell^2$ for $\ell/R = 1.0$. Fig. (A) show the free energies of the splay states (solid curve) and the tennis-ball states (dashed curves) with leading term coefficient fixed at -0.1 -0.08, -0.06, -0.04, and -0.02 from the top to bottom curves. Fig. (B) show the free energies of the splay states(solid curve) and the rectangle states (dashed curves) with leading term coefficient fixed at 0.1 0.08, 0.06, 0.04, and 0.02 from the top to bottom curves. Fig. (C) show the free energies of the splay states (solid curve) and the cut-and-rotate splay states (dashed curves) with leading term coefficient fixed at 0.1 0.08, 0.06, 0.04, and 0.02 from the top to bottom curves.

term; these terms do not exist in a splay state. We *fixed* the coefficients ϕ_{lmn} of these non-splay terms (hence enforced symmetry breaking into a particular state) and numerically searched for the free-energy minima by varying other coefficients. The fixed ϕ_{lmn} was set at small increments, covering a significant range to ensure a thorough search. Examples of such a minimization procedure are displayed in Figs. 2.2-2.11 as well. The dashed curves in Figs. 2.2(A)-2.11(A) show the resulting free energies by letting the tennis-ball order parameter $\phi_{3,2,0}$ fixed at -0.1, -0.08, -0.06, -0.04, and -0.02, from the top to bottom. The dashed curves in Figs. 2.2(B)-2.11(B) show the resulting free energies by letting the rectangle order parameter $\phi_{2,2,0}$ fixed at 0.1, 0.08, 0.06, 0.04, and 0.02, from the top to bottom. The dashed curves in Figs. 2.2(C)-2.11(C) show the resulting free energies by letting the cut-and-rotate splay order parameter $\phi_{3,-2,0}$ fixed at 0.1, 0.08, 0.06, 0.04, and 0.02, from the top to bottom. Note the highest curves in all these plots have free energies far exceeding the free energy of the isotropic state (i.e., $\tilde{f}$ is significantly positive) at a wide range of $\rho\ell^2$. Most importantly, $\tilde{f}$ as a function of ϕ_{lmn} for a considered $\rho\ell^2$ changes monotonically. Within the parameter range searched in this work, we can rule out the existence of stable non-splay configurations. As well, these plots demonstrates how other possible conformations converge to a splay ground state, as the relevant ϕ_{lmn} decreases.

2.4.2 Onsager model and Frank energy

The consideration of a ground-state tennis-ball conformation stemmed from an analysis of elastic theory of the orientational field generated by the particles. In a one-Frank-constant approximation in two dimensions [58, 49], K_2 is absent and $K_1 = K_3$, where K_1 for splay distortion, K_2 for twist distortion, and K_3 for bend distortion are the Frank constants; the Frank energy can be mapped into the energy of the two-dimensional ferromagnetic XY model [59]. Then one can show that the free energy is proportional to the square of the defect index. The tennis-ball conformation contains four $+1/2$ defects (the orientational field turns a π angle around each defect) and the splay conformation contains two $+1$ defects (the orientational field turns 2π around each defect). Thus, within this assumption, the tennis-ball conformation has a lower energy than that of the splay [58, 49].

Here we deal with the specific system of thin rods ($D/\ell \sim 0$), for which we need to check if the one-Frank-constant approximation is still satisfied. In fact, the Frank free energy (Eq. 1.2) can be recovered from the Onsager free energy (Eq. 2.1); it was explored previously for nematic textures to determine Frank constants from the Onsager model [81, 73]. The basic idea in this comparison is to assume a distribution function $\varrho(\mathbf{r}, \mathbf{u})$ in terms of $\mathbf{u}$ and $\mathbf{n}(\mathbf{r})$ by introducing a trial function describing the angular distribution about a vector director field $\mathbf{n}(\mathbf{r})$ and integrate out the $\mathbf{u}$ dependence so that the free energy is now dependent on $\mathbf{n}(\mathbf{r})$ only. As the next step, a square first-order-derivative expansion is carried out, leaving leading quadratic terms in the same structure as the Frank energy. This way, one can pin down the Frank coefficients for nematic rods, without phenomenological assumptions of the magnitude of K_1, K_2 and K_3. According to Refs. [81, 69], such a comparison gives rise to $K_1 \simeq 0.06 \ll K_3 \simeq 0.4$ [81] in a system containing thin rods [74, 7]. This estimate can be contrasted with the $K_1 \sim K_3$ requirement for the stabilization of a tennis-ball configuration discussed in Refs. [58, 49], and is the reason why nematic, *rigid* rods does not display the tennis-ball configuration on spherical surface.

On the other hand, confined systems consisting of molecules with some semi-flexibity might display the tennis-ball texture in high density. An interesting real system is the liquid of 5CB molecules [48], which has $K_1 \approx K_3$ [10], in consistence with the one-Frank-constant condition; experimentally, non-splay textures were observed [48]. Another related system, though theoretical, is a long self-avoiding semiflexible polymer chain confined on a spherical surface. Because of the flexibility along the chain, K_3 now becomes comparable to K_1. Using Monte Carlo simulations, it was recently concluded that this system displays a disorder-order transition, where the ordered state always accompanies the tennis-ball symmetry [91].

Monte Carlo simulations of nematic rods on a spherical surface agree with the results here [7]. It should be noted, however, the analysis in Refs. [81, 73] was conducted by assuming a specific distribution form in $\varrho(\mathbf{r}, \mathbf{u})$ and was done in three dimensional space. A similar analysis for nematic rods embedded on a curved surface will reveal the nature of K_1 and K_3 further and is useful.

2.4.3 Cut-and-rotate splay

Using Monte Carlo simulations of thin rods on a spherical surface, Shin *et al.* recently suggested the existence of the so-called cut-and-rotate splay conformation in closely packed hard rods [74], where $\ell/R \approx 0.4$ and $\rho\ell^2 \approx 14$. The hard rods were modeled by straight lines and confined to the tangent plane of the sphere, each rod having a nonzero diameter $D = \ell/15$. The excluded volume interaction of this thickness-to-length ratio has the same effects as the excluded area interaction of geodesic rods considered in this work. The cut-and-rotate splay configuration can be visualized as if it is made from a perfect splay by cutting the plane containing the north and south poles, rotating one of the hemispheres by an angle, and then reforming the structure by combining two hemispheres. In an idealized picture [Fig. 1.9(A4)] where the director field *perfectly* aligns along the longitudinal lines, there is no Frank-free-energy cost for cutting and rotating and, consequently, the cut-and-rotate splay configuration has a similar Frank energy as the splay state, according to the analysis based on the Frank free energy model [58, 49, 74].

However, the angular distribution about the director field of this conformation contains a sharp change at the cutting circle. Following the trial function approach and taking a complete expansion of the Onsager free energy in terms of spatial derivatives of $\mathbf{n}(\mathbf{r})$, one can show that only the quadratic terms of first-order derivatives correspond to the Frank energy [81, 73]. Higher order terms, both in higher power of the first derivatives and higher-order derivatives of $\mathbf{n}(\mathbf{r})$, which are included in the unexpanded version of the Onsager free energy, disfavor such sharp changes by raising the free energy of the system. This effect rules out the cut-and-rotate splay in the current system. It should be noted that the model in this research deals with geodesic rods, which are not exactly straight rods simulated in Refs. [74, 7]; despite this, we still expect the same qualitative physical picture in the small ℓ/R limit.

In the above we have already calculated the free energy of an enforced cut-and-rotate splay symmetry shown in Figs. 2.2-2.11, from a numerical solution of (2.17) by fixing a leading cut-and-rotate splay term, $\phi_{3,2,0}$. Here we take yet another approach to examine this state by actually taking a "cut-and-rotate" process. To

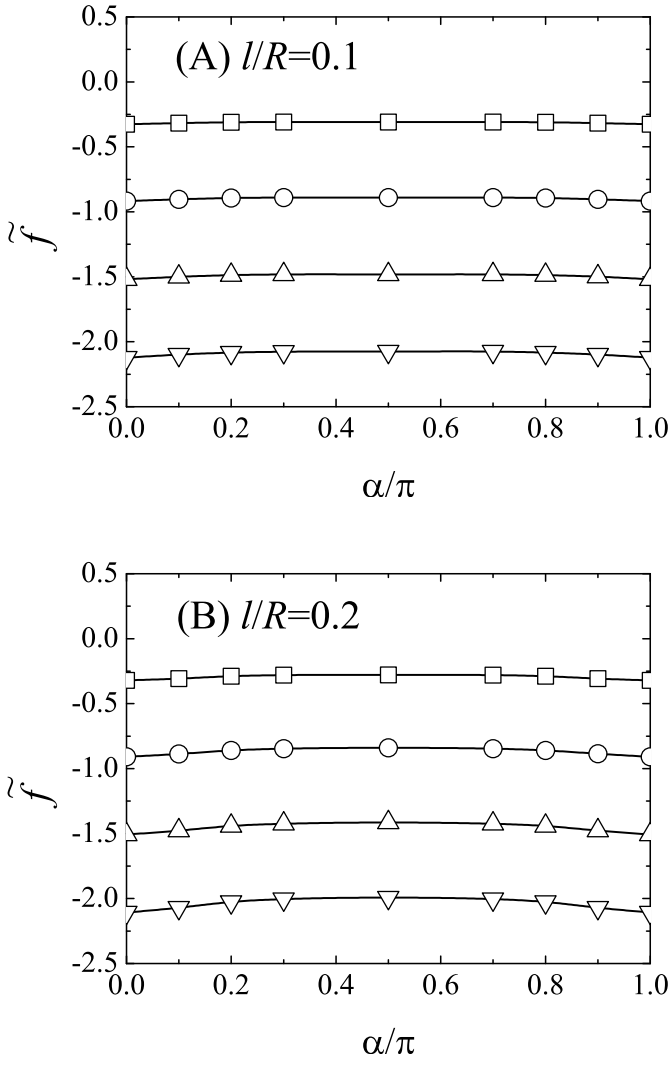

Figure 2.12: Cut-and-rotate-splay free energy plotted as a function of the rotation angle α at various densities $\rho\ell^2 = 7.96$ (circles), 11.94 (squares), 15.92 (up triangles), and 19.90 (down triangles) for (A) $\ell/R = 0.1$ and (B) $\ell/R = 0.2$, based on the solution of (2.6).

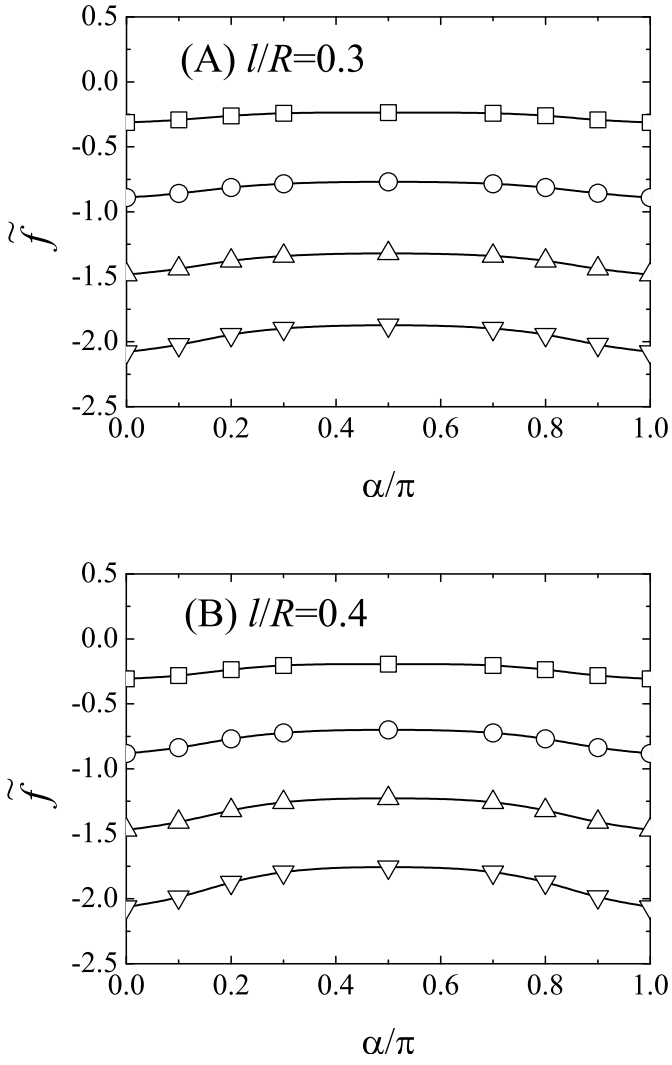

Figure 2.13: Cut-and-rotate-splay free energy plotted as a function of the rotation angle α at various densities $\rho\ell^2 = 7.96$ (circles), 11.94 (squares), 15.92 (up triangles), and 19.90 (down triangles) for (A) $\ell/R = 0.3$ and (B) $\ell/R = 0.4$, based on the solution of (2.6).

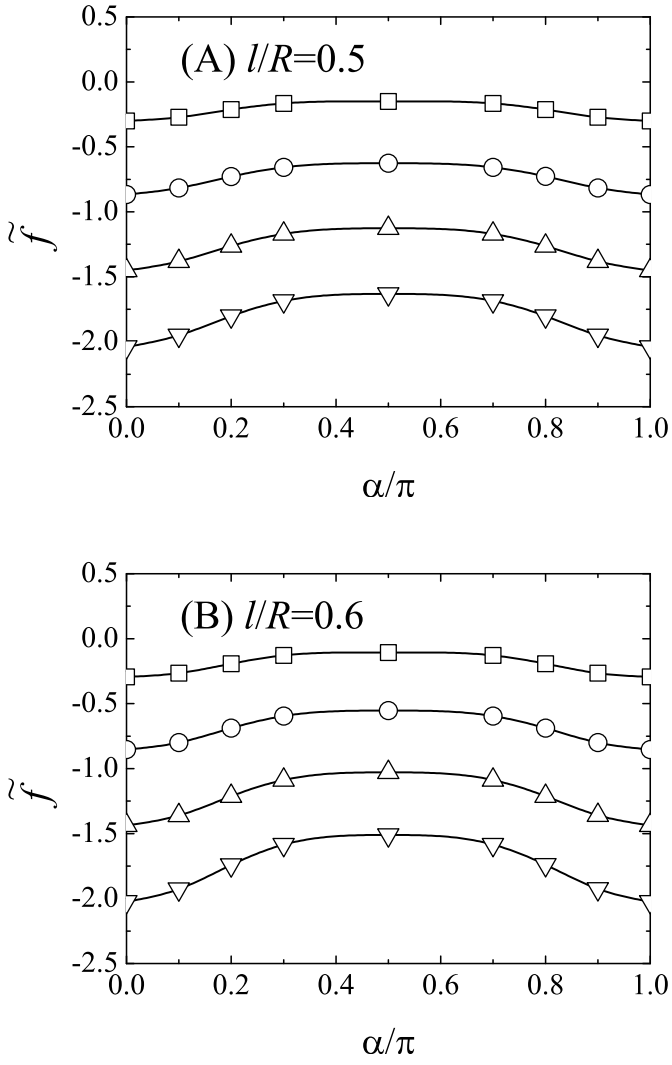

Figure 2.14: Cut-and-rotate-splay free energy plotted as a function of the rotation angle α at various densities $\rho\ell^2 = 7.96$ (circles), 11.94 (squares), 15.92 (up triangles), and 19.90 (down triangles) for (A) $\ell/R = 0.5$ and (B) $\ell/R = 0.6$, based on the solution of (2.6).

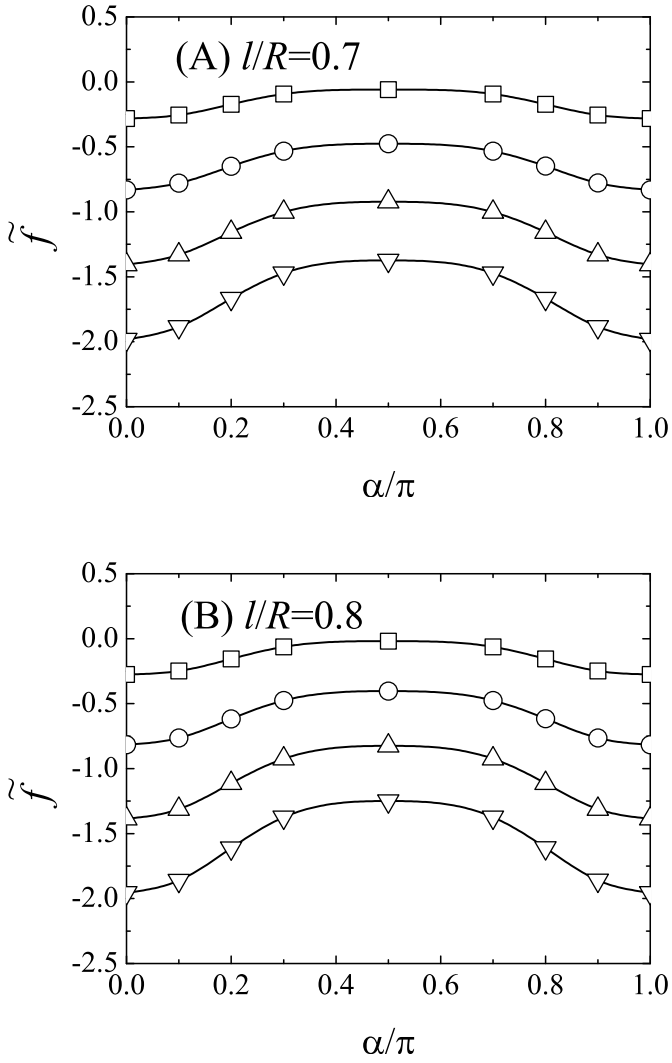

Figure 2.15: Cut-and-rotate-splay free energy plotted as a function of the rotation angle α at various densities $\rho\ell^2 = 7.96$ (circles), 11.94 (squares), 15.92 (up triangles), and 19.90 (down triangles) for (A) $\ell/R = 0.7$ and (B) $\ell/R = 0.8$, based on the solution of (2.6).

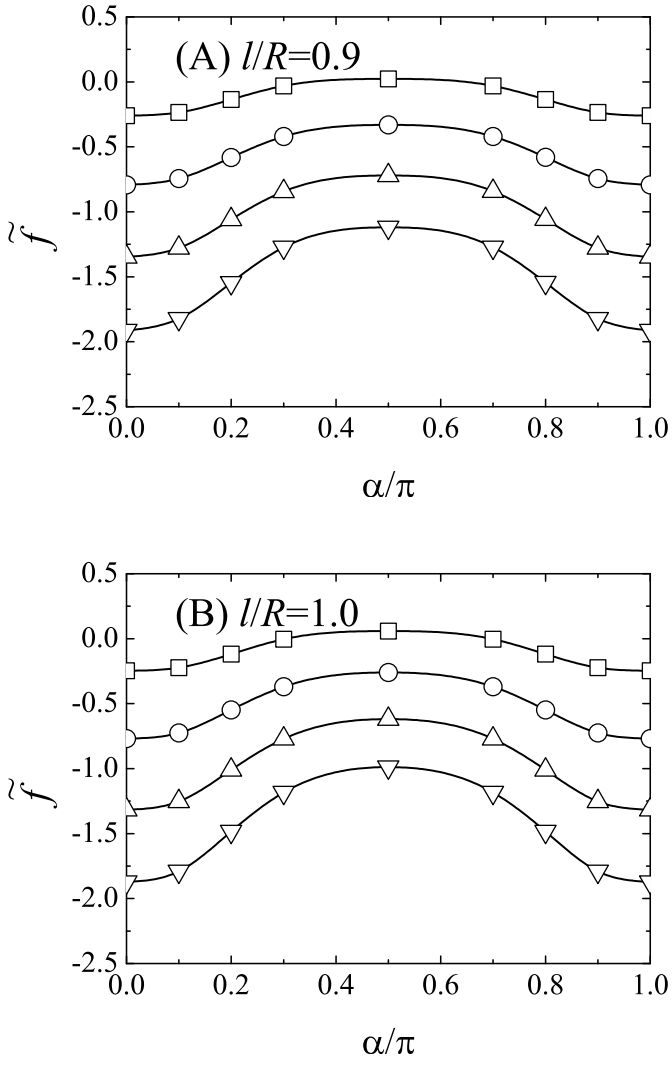

Figure 2.16: Cut-and-rotate-splay free energy plotted as a function of the rotation angle α at various densities $\rho\ell^2 = 7.96$ (circles), 11.94 (squares), 15.92 (up triangles), and 19.90 (down triangles) for (A) $\ell/R = 0.9$ and (B) $\ell/R = 1.0$, based on the solution of (2.6).

show the cut-and-rotate effects, we took the density distribution $f_{\rm spl}(\Theta,\theta)$ of the splay conformation, which was obtained from the free energy minimization, and cut it through the xz-plane. Then the distribution on the hemisphere containing the positive y-axis was rotated by an $\alpha/2$ angle about the y-axis, and the distribution on the other hemisphere is rotated by a $-\alpha/2$ angle. With the aid of the addition theorem of spherical harmonics, the new distribution could be easily obtained, which was substituted into Eq. 2.6 for evaluation of the free energy. In Figs. 2.12-2.16, we display the cut-and-rotate splay free energy per rod, as a function of the rotation angle α, for $\ell/R = 0.1, 0.2, 0.3, ..., 1.0$. From the plots, we can see that cut-and-rotate splay state has a higher free energy in comparison with that of the splay state ($\alpha = 0$ or π). This is more so in large-ℓ/R systems than in small-ℓ/R systems. These plots, together with the symmetry-based analysis in Figs. 2.2-2.11, preclude the probability that cut-and-rotate splay is a stable state within the validity of the free energy model in (2.6).

2.4.4 Nematic-director field, local entropy field, and defect visualization

As discussed above, all four possible configurations considered in this Chapter contain coupled orientational and spatial ordering. In this subsection, we discuss order parameters resulting from the numerical solution of the Onsager model (Eq. 2.6).

The left panels in Fig. 1.9 are idealized texture illustrations where the local nematic directors are indicated by *unit vectors* forming a director field. The important information on the local orientational entropy is not clearly represented in these plots. On the basis of the distribution function containing Θ, Φ and θ as variables, we consider here a *scalar* orientational entropy field $\sigma(\Theta,\Phi)$, represented by a local orientational order parameter defined by the following procedure. First, a 2×2 matrix $\mathcal{S}$ is constructed,

$$\mathcal{S} = \langle 2\mathbf{uu} - \mathbf{I} \rangle = \begin{pmatrix} \langle \cos 2\theta \rangle & \langle \sin 2\theta \rangle \\ \langle \sin 2\theta \rangle & -\langle \cos 2\theta \rangle \end{pmatrix}. \tag{2.20}$$

The average $\langle \cdots \rangle$ is performed over the orientational distribution locally,

$$\langle \cos 2\theta \rangle = \frac{\int \cos 2\theta f(\Theta, \Phi; \theta) \mathrm{d}\theta}{\int f(\Theta, \Phi; \theta) \mathrm{d}\theta}, \tag{2.21a}$$

$$\langle \sin 2\theta \rangle = \frac{\int \sin 2\theta f(\Theta, \Phi; \theta) \mathrm{d}\theta}{\int f(\Theta, \Phi; \theta) \mathrm{d}\theta}. \tag{2.21b}$$

We then select the positive eigenvalue of the matrix $\mathcal{S}$ as a measure for the orientational entropy field,

$$\sigma(\Theta, \Phi) = \sqrt{\langle \cos 2\theta \rangle^2 + \langle \sin 2\theta \rangle^2}. \tag{2.22}$$

Figures 1.9(B1)-(B4) are illustrations of $\sigma(\Theta, \Phi)$ for $L/R = 0.5$ and $\rho L^2 = 12$, based on $f(\Theta, \Phi; \theta)$ determined from the present work, which was obtained for splay (all expansion coefficients free in minimization), tennis-ball ($\phi_{3,2,0}$ fixed at 0.1), rectangle ($\phi_{2,2,0}$ fixed at 0.1), and cut-and-rotate splay ($\phi_{3,-2,0}$ fixed at 0.1) configurations. A color scheme is used in the plot, where red, yellow, green, cyan, and blue are used to represent σ values ranging from high to low. These plots show that the structural defects can be visualized not only by the director field but also by an analysis of the orientational entropy field. In the splay configuration, two low σ (high-entropy) defects are located at north and south poles. In a tennis-ball state, four low-σ defects occupy the vertices of a tetrahedron, *which is a similar picture as the one displayed for the result of a Landau-de Gennes model under one-Frank constant approximation* [40]. In a rectangle configuration, four low σ defects can be seen along a great circle cutting through xz-plane, where the pattern in a low σ region is greatly distorted; in a cut-and-rotate splay configuration, four low σ defects follow the same symmetry of the director-field defects; however, the locations of the lowest σ (off the xz-plane) do not completely overlap with the locations of the proposed defects (on the xz-plane) in the director field [74]. These plots can be compared with Figs. 1.9(A1)-(A4), where an idealized illustration of the four configurations is displayed.

2.4.5 Splay order parameter

Next we examine two order parameters that display the characteristics of the overall orientational and positional ordering of the disorder-splay phase transition. One of

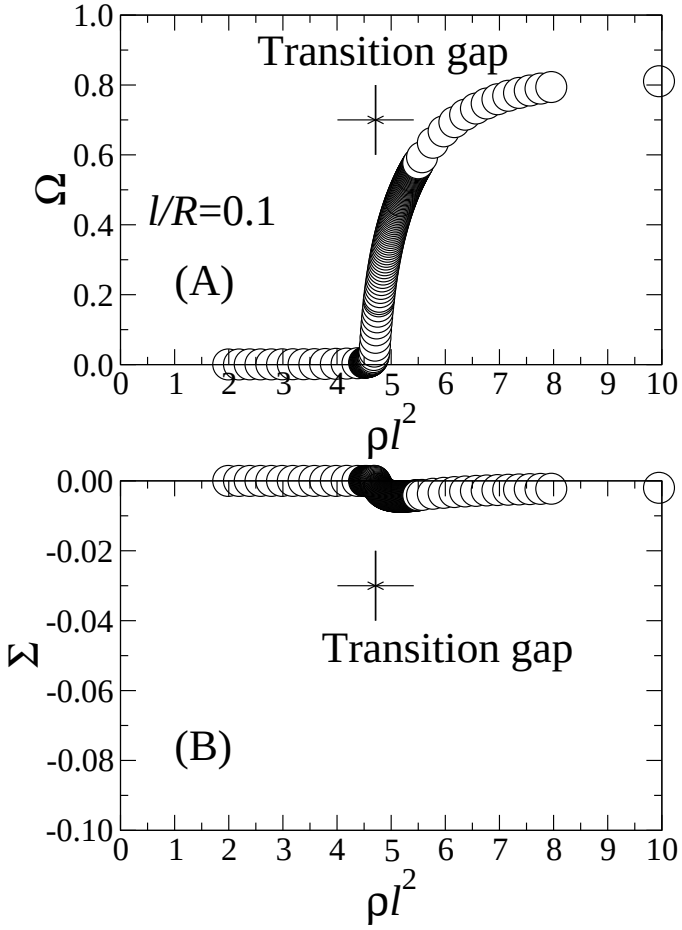

Figure 2.17: Orientational (A) and positional (B) order parameters, Ω, Σ, plotted as functions of reduced density, $\rho\ell^2$, for $\ell/R = 0.1$. Data points associated with nonzero Ω and Σ were produced from splay configurations. The area inside the two vertical lines indicate the transition region discussed in Sect. 2.4.3

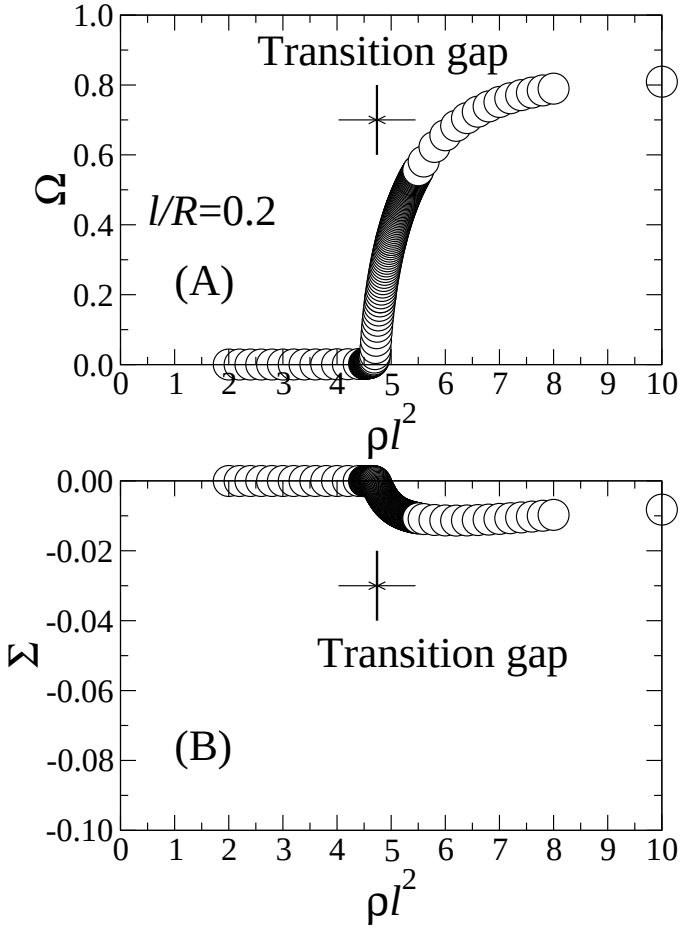

Figure 2.18: Orientational (A) and positional (B) order parameters, Ω, Σ, plotted as functions of reduced density, $\rho\ell^2$, for $\ell/R = 0.2$. Data points associated with nonzero Ω and Σ were produced from splay configurations. The area inside the two vertical lines indicate the transition region discussed in Sect. 2.4.3.

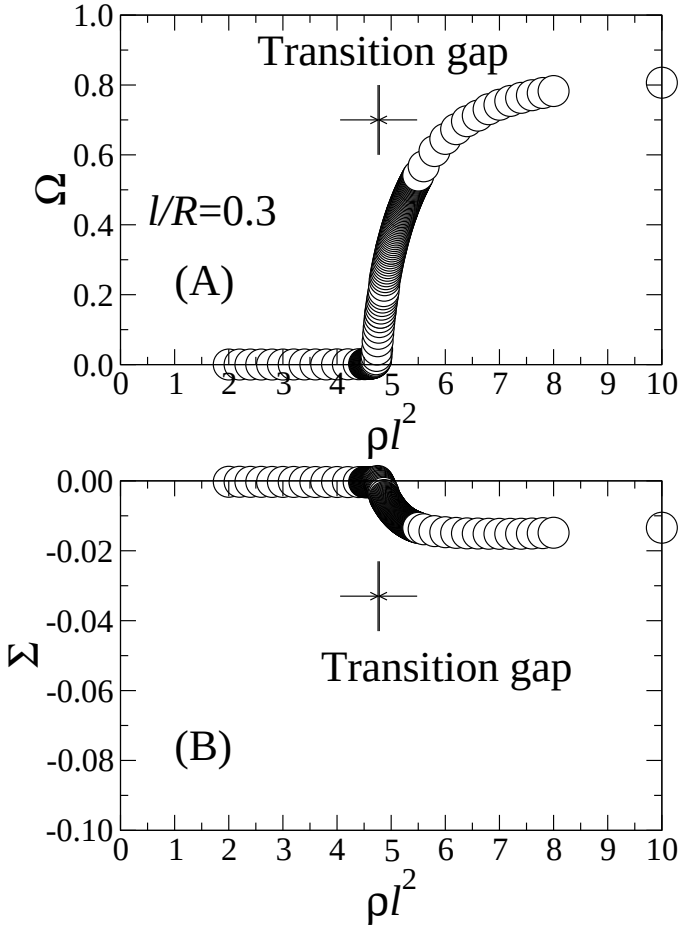

Figure 2.19: Orientational (A) and positional (B) order parameters, Ω, Σ, plotted as functions of reduced density, $\rho\ell^2$, for $\ell/R = 0.3$. Data points associated with nonzero Ω and Σ were produced from splay configurations. The area inside the two vertical lines indicate the transition region discussed in Sect. 2.4.3.

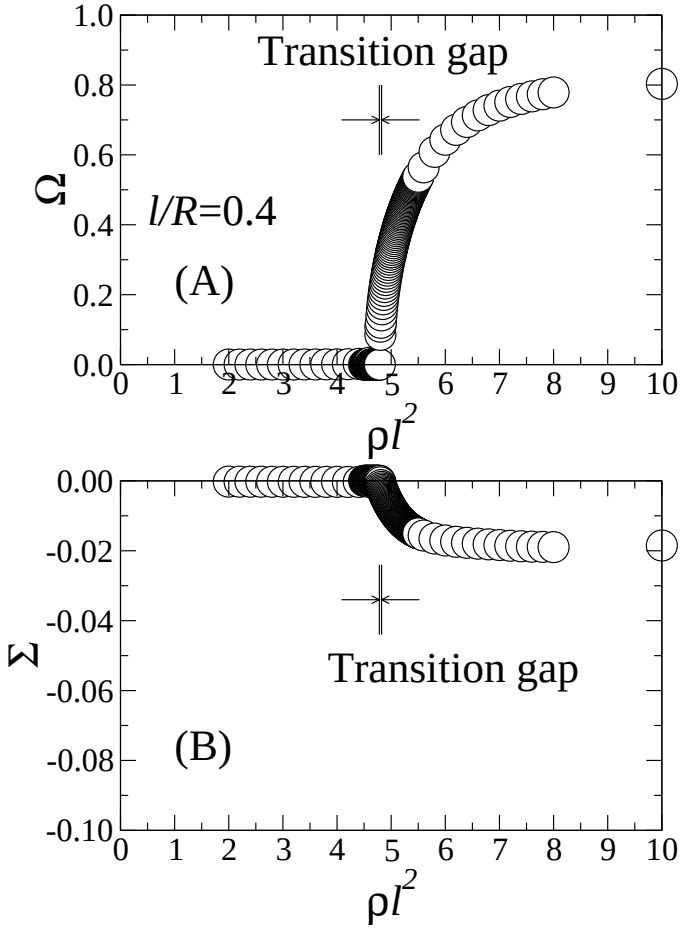

Figure 2.20: Orientational (A) and positional (B) order parameters, Ω, Σ, plotted as functions of reduced density, $\rho\ell^2$, for $\ell/R = 0.4$. Data points associated with nonzero Ω and Σ were produced from splay configurations. The area inside the two vertical lines indicate the transition region discussed in Sect. 2.4.3.

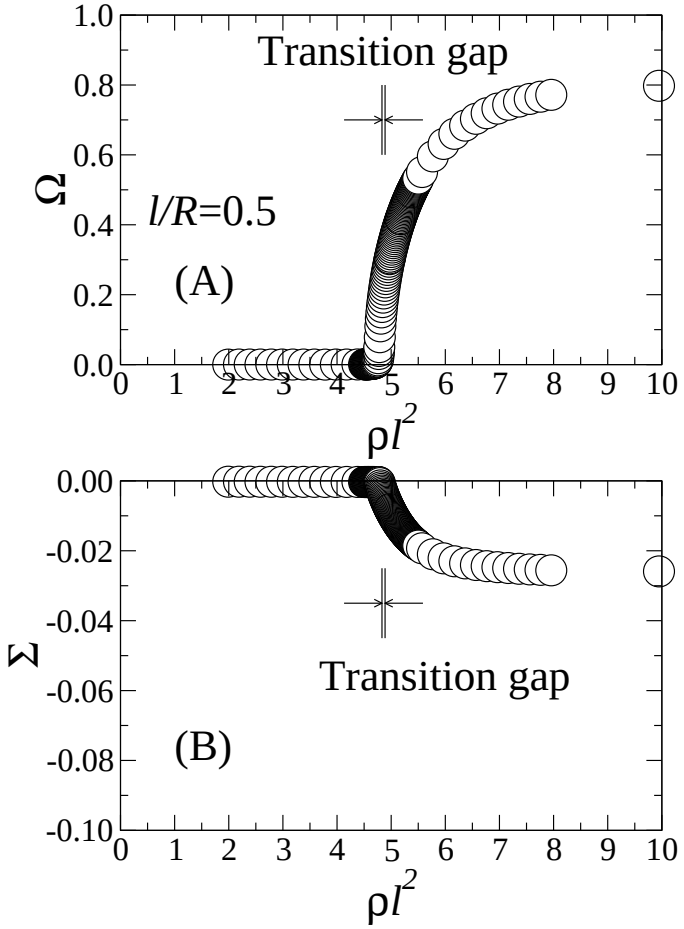

Figure 2.21: Orientational (A) and positional (B) order parameters, Ω, Σ, plotted as functions of reduced density, $\rho\ell^2$, for $\ell/R = 0.5$. Data points associated with nonzero Ω and Σ were produced from splay configurations. The area inside the two vertical lines indicate the transition region discussed in Sect. 2.4.3.

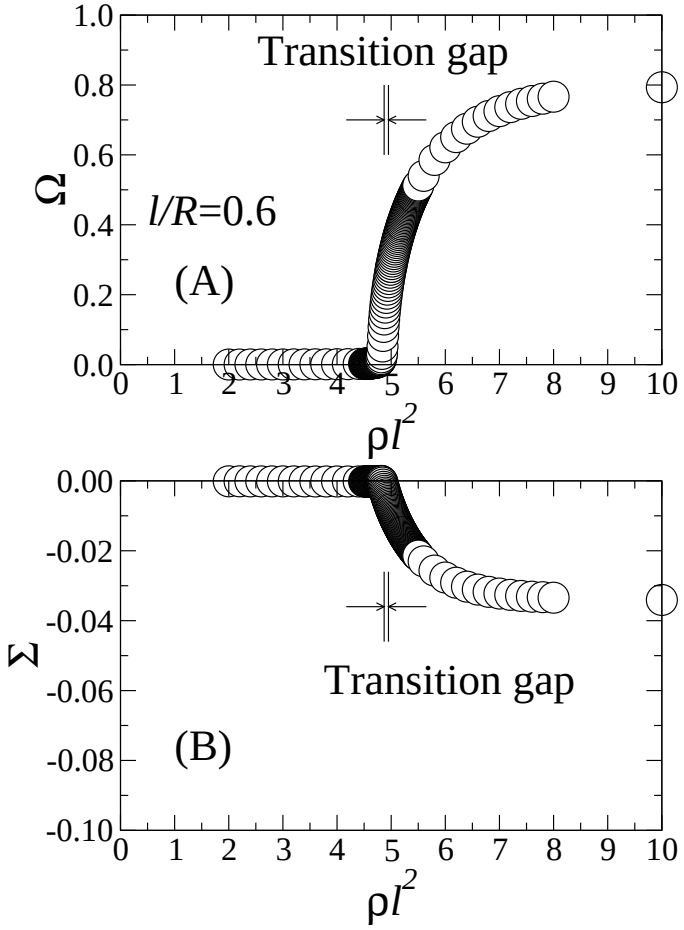

Figure 2.22: Orientational (A) and positional (B) order parameters, Ω, Σ, plotted as functions of reduced density, $\rho\ell^2$, for $\ell/R = 0.6$. Data points associated with nonzero Ω and Σ were produced from splay configurations. The area inside the two vertical lines indicate the transition region discussed in Sect. 2.4.3.

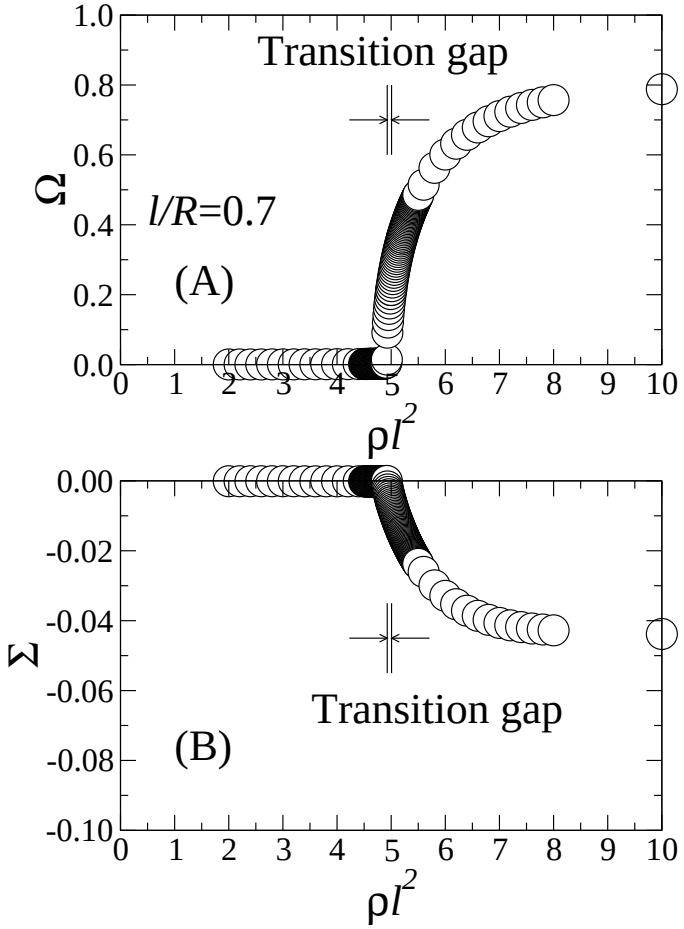

Figure 2.23: Orientational (A) and positional (B) order parameters, Ω, Σ, plotted as functions of reduced density, $\rho\ell^2$, for $\ell/R = 0.7$. Data points associated with nonzero Ω and Σ were produced from splay configurations. The area inside the two vertical lines indicate the transition region discussed in Sect. 2.4.3.

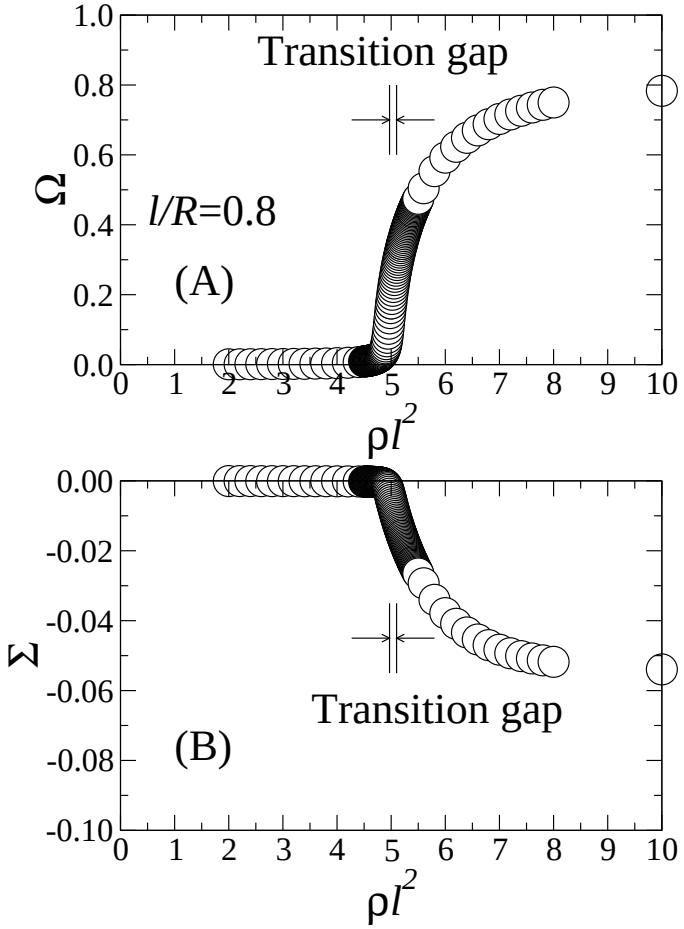

Figure 2.24: Orientational (A) and positional (B) order parameters, Ω, Σ, plotted as functions of reduced density, $\rho\ell^2$, for $\ell/R = 0.8$. Data points associated with nonzero Ω and Σ were produced from splay configurations. The area inside the two vertical lines indicate the transition region discussed in Sect. 2.4.3.

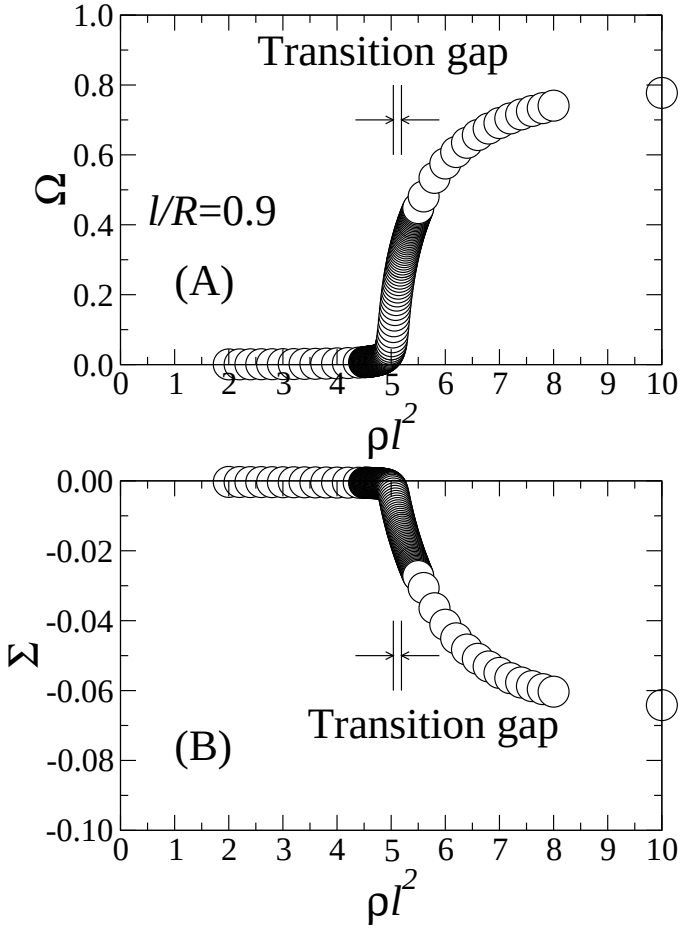

Figure 2.25: Orientational (A) and positional (B) order parameters, Ω, Σ, plotted as functions of reduced density, $\rho\ell^2$, for $\ell/R = 0.9$. Data points associated with nonzero Ω and Σ were produced from splay configurations. The area inside the two vertical lines indicate the transition region discussed in Sect. 2.4.3.

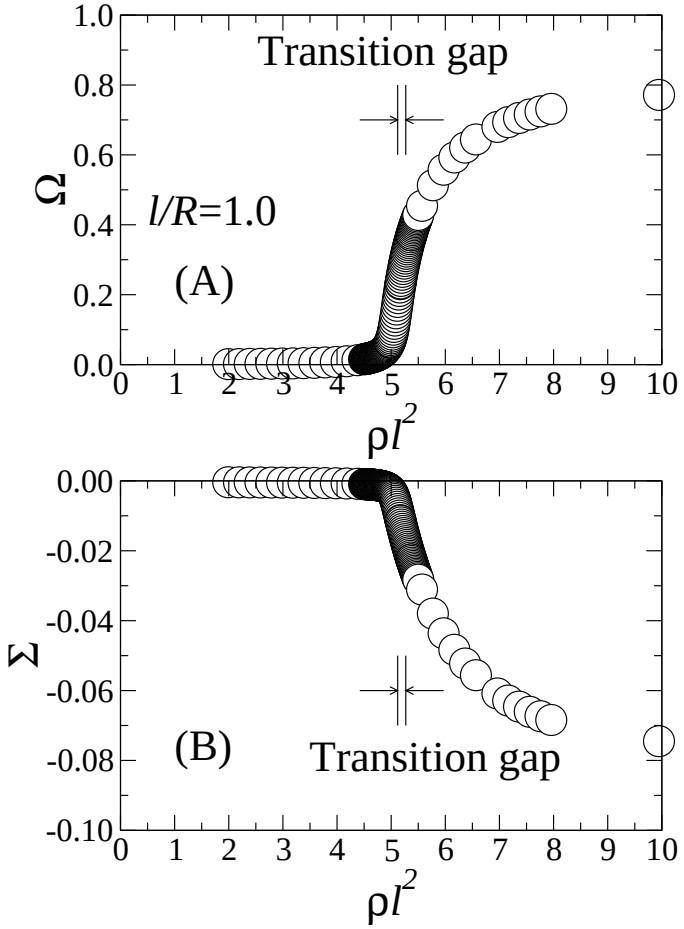

Figure 2.26: Orientational (A) and positional (B) order parameters, Ω, Σ, plotted as functions of reduced density, $\rho\ell^2$, for $\ell/R = 1.0$. Data points associated with nonzero Ω and Σ were produced from splay configurations. The area inside the two vertical lines indicate the transition region discussed in Sect. 2.4.3.

which, Ω, concerns the global orientational order and is defined by,

$$\begin{aligned}\Omega &= \int \cos 2\theta f(\Theta, \Phi; \theta) \sin \Theta \mathrm{d}\Theta \mathrm{d}\Phi \mathrm{d}\theta \\ &= 2\pi\phi_{002},\end{aligned} \tag{2.23}$$

which yields a 0 value in the isotropic phase, a positive value in the splay phase where rods line up along the longitudes (observed here), and a negative value in the helicoidal phase where rods line up along the latitudes. The fact that we only see a positive Ω for *rigid* rods verifies the fact that $K_1 \ll K_3$ discussed in Sect. 2.4.2; this was noted by Nelson in Ref. [58].

The global spatial order parameter,

$$\begin{aligned}\Sigma &= \int P_2 (\cos \Theta) f(\Theta, \Phi; \theta) \sin \Theta \mathrm{d}\Theta \mathrm{d}\Phi \mathrm{d}\theta \\ &= \sqrt{\frac{8}{5}}\pi\phi_{200},\end{aligned} \tag{2.24}$$

yields a 0 value in the isotropic phase, a positive value in a spatially ordered state where the pole regions are more dense, and a negative value in a spatially ordered state where the equator region is more dense.

Figures 2.17-2.26 show Ω and Σ as functions of $\rho\ell^2$ for the splay branch. The initial guess of the density distribution function $f(\Theta, \Phi; \theta)$ in the numerical search was taken from the optimized function determined earlier at a slightly higher value of $\rho\ell^2$. This way, in the region where a disorder state is stable (reflected by significantly nonzero Ω and Σ), the minimized results closely adhered to a splay configuration. As $\rho\ell^2$ is lowered passing a transition region, an isotropic state is reached in the low density region, where $\Omega = \Sigma = 0$. Comparing Σ of the case $\ell/R = 0.1$ with those of the systems $\ell/R = 0.5$ and 1.0, we can also see that the spatial ordering is weakened as ℓ/R becomes smaller. This is consistent with the expectation that this model system here becomes spatially disordered approaching the asymptotic limit of a flat two-dimensional system, $\ell/R \ll 1$, while keeping an orientational order (a nematic state).

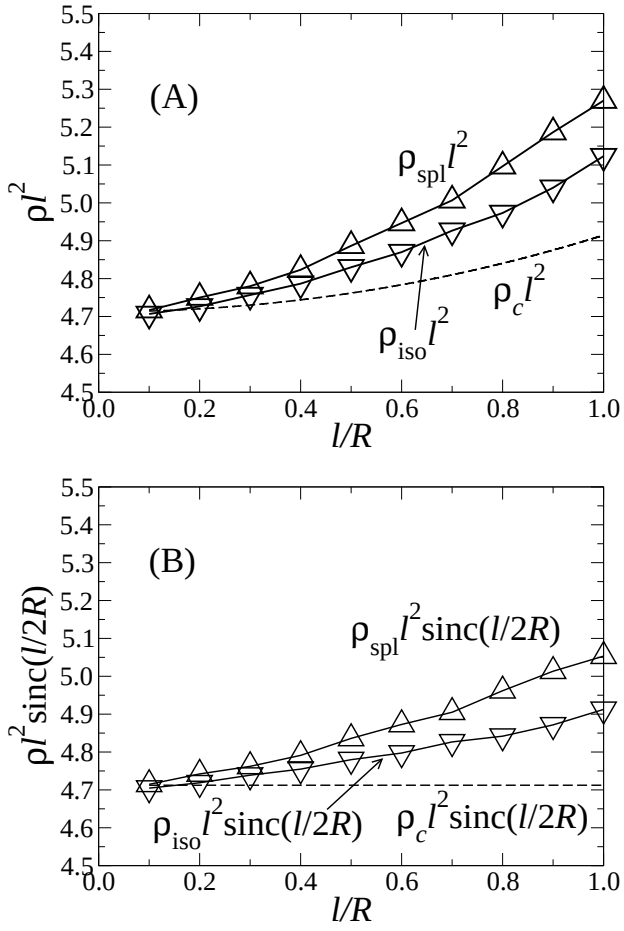

Figure 2.27: Transition densities determined from the numerical results plotted as a function of ℓ/R in two perspectives: (A) $\rho_{\rm iso}\ell^2$ (down triangles) and $\rho_{\rm spl}\ell^2$ (up triangles) themselves and (B) with a curvature factor $\mathrm{sinc}(\ell/2R)$. The dashed curves demonstrates a perceived isotropic-nematic transition in a curved space, $\rho_c\ell^2\mathrm{sinc}(\ell/2R) = 3\pi/2$, which is gives the correct transition point at $\ell/R = 0$ only.

2.4.6 Disorder-splay phase transition

The order-parameter plots in Fig. 2.17-2.26 follow the splay solution of the model and give us the approximate location of the transition density for the disorder-splay phase transition (bifurcation point). To further study the characteristics of the isotropic-splay transition, we used splay-relevant, undetermined ϕ_{l0n} and substituted them into Eq. 2.17, to produce an expansion of the free energy. In comparison with the Landau expansion in the phase-transition theory, one important feature in the expansion is the existence of third order terms coupling Ω with Σ and other ϕ_{l0n} factors. This can be understood from the symmetry of the problem without actually expanding the free energy. For example, making the transformation of $\Omega \to -\Omega$ implies the change from splay to latitudinal helicoidal or vice versa; these are two different physical states hence the corresponding free energies cannot be identical. Moreover, the change in the free energies cannot be compensated by the transformation of other coefficients ϕ_{l0n}. An immediate implication is that in a Landau expansion, odd-power terms exist, so that the associated phase transition is discontinuous. Using the numerical data presented above, we clarify the properties of the transition in this subsection.

The method used here is similar to the determination of the first-order isotropic-nematic phase transition in the lyotropic liquid-crystal theory, although there is no spatial disorder in the latter [65, 61]. To determine the transition density, conceptually we consider two systems, one is in an isotropic phase with a number density $\rho_{\rm iso}$ and the other is in a splay state with $\rho_{\rm spl}$. These two systems are in phase equilibrium at the transition densities, in such a way that the chemical potentials,

$$\mu = (\partial F/\partial N)_A, \tag{2.25}$$

are the same in the two systems. We also equate the osmotic pressures,

$$\Pi = (\mu N - F)/A, \tag{2.26}$$

in the two systems, where $A = 4\pi R^2$ is the surface area,. The transition densities

are determined from solving two non-linear equations,

$$\mu_{\rm iso}(\rho_{\rm iso}) = \mu_{\rm spl}(\rho_{\rm spl}), \tag{2.27a}$$

$$\Pi_{\rm iso}(\rho_{\rm iso}) = \Pi_{\rm spl}(\rho_{\rm spl}). \tag{2.27b}$$

The free energy βF is already given in (2.15) for the splay branch and (2.16) for the isotropic branch. The derivatives of the free energy of the isotropic branch can be obtained analytically from (2.16), while those of the splay branch were obtained in this work by a numerical difference with respect to ρ. The procedure is identical to the one used in studying the isotropic-nematic transition of a lyotropic system of rods [61].

The transition densities $\rho_{\rm iso}\ell^2$ and $\rho_{\rm spl}\ell^2$ are plotted in Fig. 2.27(A) by down and up triangles, respectively. The first-order transition gap is wider in larger ℓ/R-systems and converges to zero in the limit of a flat two-dimensional system ($\ell/R \to 0$). This fact implies that the first-order disorder-splay transition reduces to a continuous isotropic-nematic transition in flat two dimensions as $\ell/R \to 0$, within the validity of the Onsager model; the asymptotic reduced transition density at $\ell/R = 0$, 4.7, is consistent with the value found earlier $\rho_c\ell^2 = 3\pi/2$ [33, 15]. For larger ℓ/R, the transition densities deviate from 4.7, the theoretical critical density of the isotropic-nematic transition of flat two dimensional hard-rod system, and the first-order nature of the disorder-splay transition in finite L/R systems starts to emerge, which can be compared to the first-order nature of the isotropic-nematic transition in a three-dimensional lyotropic system [61, 34, 35, 16]. The reasons of the deviation and the first-order nature are the curvature of the spherical surface and the non-uniform spatial distribution of rods on the spherical surface, which are discussed within two steps below.

First, we assume that the rods are uniformly distributed in space and consider the effect of the curvature of the spherical surface. For two rods embedded in flat two dimensions, the excluded volume is $\ell^2 \sin\gamma$, where γ is the angle between the directions of the two rods. However, for two rods confined to a spherical surface, the excluded volume must be rewritten as $\ell^2 \mathrm{sinc}(\ell/2R) \sin\gamma$ due to the curvature of the spherical surface (see Appendix C for the derivation), where the function $\mathrm{sinc}x = \sin x/x$. Taking into account the curvature of the spherical surface, we

have to rewrite the reduced density as

$$\rho\ell^2\text{sinc}\frac{\ell}{2R} = \frac{N\ell^2}{4\pi R^2}\text{sinc}\frac{\ell}{2R}. \tag{2.28}$$

In the next subsection about the bifurcation analysis, we confirm that, within the assumption of uniform spatial distribution, the disorder-splay transition should be continuous and the critical density would be $\rho_c\ell^2\text{sinc}(\ell/2R) = 3\pi/2$, same as that of flat two dimensions. In Fig. 2.27(B), we plot the transition densities as the redefined reduced density $\rho\ell^2\text{sinc}(\ell/2R)$ *v.s.* ℓ/R, which can be compared to the constant value $3\pi/2$ (dashed line). However, the transition densities still deviate from $\rho_c\ell^2\text{sinc}(\ell/2R) = 3\pi/2$, which is due to the non-uniform spatial distribution of rods in fact.

In the second step, we cancel out the assumption of uniform spatial distribution to investigate the effects of non-uniform spatial distribution that indeed occurs in the system here. According to the discussion in the next subsection, we confirm that the non-uniform spatial distribution will generate cubic terms in the Landau expansion of the free energy, which implies that the transition is first order. Besides, as mentioned in the last subsection, the spatial order becomes stronger as ℓ/R becomes larger. Therefore, the gap and the deviation of transition densities away from $\rho_c\ell^2\text{sinc}(\ell/2R) = 3\pi/2$ is more obvious for larger ℓ/R (Fig. 2.27).

In summary, the fact that the first-order nature of the disorder-splay transition of the rigid-rod system confined to the *spherical* surface differs from the continuous isotropic-nematic transition of a hard-rod fluid in *flat* two-dimensional space is due to both the curvature of the spherical surface and non-uniform spatial distribution of rods.

Instead of the hypothetical phase-equilibrium physical picture, we are, however, dealing with a single system where N (therefore $\rho\ell^2$) is fixed. In a typical plot given in Fig. 2.17-2.26 where ρ continually changes, we can divide ρ into three regions. In the $\rho \leq \rho_{\text{iso}}$ or $\rho \geq \rho_{\text{spl}}$ region, the system is either in a disorder or splay state. In the $\rho_{\text{iso}} < \rho < \rho_{\text{spl}}$ region, the system is actually in a crossover state between the disorder and splay states. Both Ω and Σ are different in this region from the splay branch plotted in Fig. 2.28. For an isotropic-nematic transition in

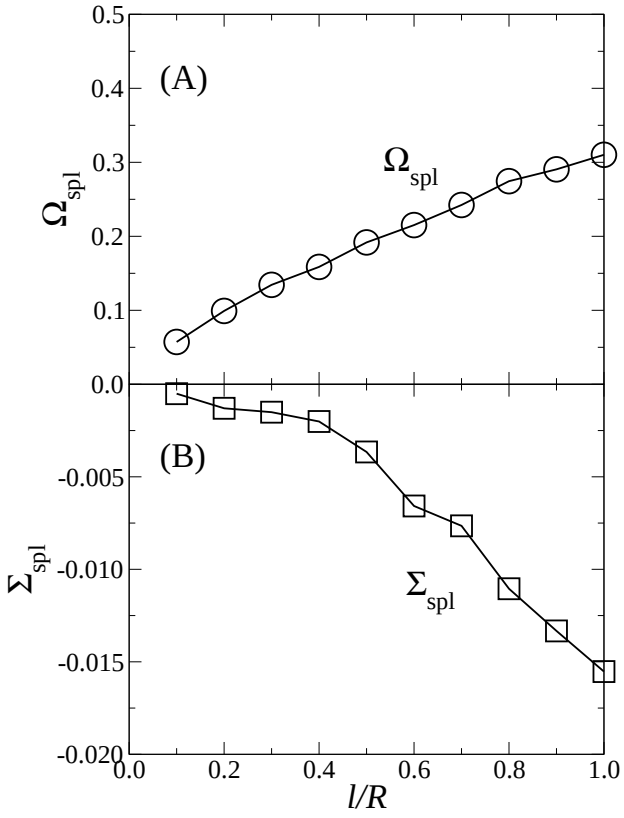

Figure 2.28: The orientational and spatial order parameters, Ω (A) and Σ (B), at $\rho_{\rm spl}\ell^2$ plotted as functions of ℓ/R.

the thermodynamic limit, this density region normally corresponds to a isotropic-nematic interface [17, 14, 19, 32]; details are not discussed further in this thesis.

We studied a free energy function in a mean-field theory level. As it turns out, in a Monte Carlo simulation where the critical fluctuations existed, Frenkel and Eppenga [27] provided concrete evidence that the two-dimensional isotropic-nematic transition in a flat space is a Kosterlitz-Thouless (KT) transition. The relationship between the disorder-splay transition of rods on a spherical surface and the KT isotropic-nematic transition of rods in a flat surface remains to be discovered by a theory or simulation where the critical fluctuations are properly incorporated.

2.4.7 Splay bifurcation analysis

Most of the results discussed in the previous subsections were based on the numerical solutions to the Onsager model. The expansion in Eq. 2.17 also offers an opportunity for us to examine the leading expansion terms of the free energy as a function of the order parameters. The analysis in this subsection verifies the results in the above for the disorder-splay transition.

Accurate to the cubic terms, in general we can write a small-ϕ_{lmn} expansion of the free energy in Eq. 2.17,

$$\begin{aligned}\tilde{f} = & \sum_{l,l',n,n'} \left(4\pi^2 \delta_{ll'}\delta_{nn'} + \frac{\rho\ell^2}{2} W_{l0n,l'0n'}\right) \phi_{l0n}\phi_{l'0n'} \\ & + \sum_{l,l',l'',n,n',n''} B_{l0n,l'0n',l''0n''}\phi_{l0n}\phi_{l'0n'}\phi_{l''0n''} \\ & + \mathcal{O}\left(\phi^4\right),\end{aligned} \tag{2.29}$$

where, because of the symmetry of splay configuration, all terms associated with an index $m \neq 0$ vanish and all l and n must be *nonnegative even* numbers. The coefficients of cubic terms $B_{l0n,l'0n',l''}$ is nonzero only if the rank l's satisfy $|l'-l''| \leq l \leq l'+l''$ and the rank n's satisfy $n = |n'-n''|$ or $n = n'+n''$. For example, the coefficients of terms $\phi_{002}^2\phi_{004}$, $\phi_{002}\phi_{200}\phi_{202}$, $\phi_{200}\phi_{202}^2$, and ϕ_{200}^3 are not zero. According to Appendix D, the coefficients of quadratic terms can be evaluated by substituting

$$W_{l0n,l'0n'} = \frac{16\pi}{1-n^2}\delta_{ll'}\delta_{nn'} + \left(\frac{\ell}{R}\right)^2 \mathfrak{F}(l,l',n,n') + \mathcal{O}\left[\left(\frac{\ell}{R}\right)^4\right] \tag{2.30}$$

into Eq. 2.29, where $\mathfrak{F}(l,l',n,n')$ is a function of l, l', n, and n'.

The discussion is organized into three steps. First, we consider the limit of flat two dimensions, i.e. $\ell/R \to 0$. In this case, only the first term of $W_{l0n,l'0n'}$ (Eq. 2.30) survives, which means the matrix W is diagonalized and the quadratic terms of the Landau expansion of free energy (Eq. 2.29) become

$$\sum_{l,n}\left[4\pi^2 + 8\pi\rho\ell^2/(1-n^2)\right]\phi_{l0n}^2.$$

For the quadratic terms of ϕ_{00n}^2 with $n \neq 0$, the coefficients could be positive at low densities and negative at high densities, since $1 - n^2 < 0$ for $n \geq 2$. Besides, the lowest transition density is given by the leading term $n = 2$, where $\rho_c \ell^2 = 3\pi/2$. The high n-rank order parameters ϕ_{00n} are coupled to ϕ_{002} due to the cubic or high order terms of the Landau expansion of free energy, e.g., $\phi_{004} \sim \phi_{002}^2$ from the cubic term $\phi_{002}^2 \phi_{004}$, which is actually of fourth order of ϕ_{002} [15]. For the quadratic terms of ϕ_{l00} with $l \neq 0$, the coefficients are definitely positive, which implies ϕ_{l00} vanishes during the minimization. For the quadratic terms of ϕ_{l0n} with $l \neq 0$ and $n \neq 0$, one can see that order parameters ϕ_{l02} for any l have the same critical density as ϕ_{002}, which is not surprising for a KT transition. During the KT transition, the vortex-anti-vortex unbinding causes an inhomogeneous spatial distribution of rods which may consist of any mode of rank l. In summary, the bifurcation analysis for the limit $\ell/R \to 0$ confirms a continuous isotropic-nematic phase transition at the critical density $\rho_c \ell^2 = 3\pi/2$, which is consistent with the study of the hard-rod system in flat two dimensions [33, 15].

Second, for finite ℓ/R, the coupling quadratic terms, such as $\phi_{002}\phi_{200}$ and $\phi_{002}\phi_{202}$, exist so that ϕ_{200} and ϕ_{202} are coupled to the linear order of ϕ_{002}. Therefore, the cubic terms $\phi_{002}\phi_{200}\phi_{202}$, $\phi_{200}\phi_{202}^2$, and ϕ_{200}^3 are indeed of cubic order and contribute to the first order phase transition.

Finally, we consider finite ℓ/R but still assume the density distribution is uniform in space, which means ϕ_{l0n} for $l \neq 0$ and any n vanishes and only the terms ϕ_{00n} survive in the Landau expansion of free energy (Eq. 2.29). We take more delicate evaluation for $W_{00n,00n'}$ in Appendix D with the assumption of uniform spatial distribution, which is

$$W_{00n,00n'} = \frac{16\pi}{1-n^2} \mathrm{sinc} \frac{\ell}{2R} \delta_{nn'}. \tag{2.31}$$

Analogically, the coefficients of quadratic terms become

$$\sum_n \left[4\pi^2 + 8\pi\rho\ell^2 \mathrm{sinc}(\ell/2R)/(1-n^2) \right] \phi_{00n}^2,$$

which implies a continuous transition at the critical density $\rho\ell^2 \mathrm{sinc}(\ell/2R) = 3\pi/2 \approx 4.7$, which is used as a reference in the discussion of transition densities in the previous subsection.

2.5 Conclusion

In this Chapter, it is demonstrated that the Onsager treatment for rigid rods can be generalized to study the system of curved rigid rods confined on the spherical surface. The excluded volume interaction in the system can be approximated by a free-energy term that depends on both orientational and positional variables. A numerical method is developed, which allows us to minimize the free energy within a controlled precision, adjusting the density distribution function. It is observed that the free energy minimum corresponds to a stable splay state and that the tennis-ball, rectangle, and cut-and-rotate splay configurations are all not stable, within a significantly wide parameter region searched computationally. The properties of the disorder-splay transition were also studied.

Chapter 3

Monte Carlo Simulation of Self-Avoiding Wormlike Polymer on a Spherical Surface

3.1 Introduction

The model of a polymer chain confined to a spherical surface provides significant insights into the physical properties of a number of chemical and biological systems [77, 57, 12, 43, 76]. It has been shown that the competition among involved length scales (the total contour length L of the polymer, the sphere radius R and the persistence length ℓ_p of the polymer) creates interesting conformational properties unique to this model [77, 43, 57, 12], which are normally seen in nanoscale in actual systems. Adding to this competition, is the interaction between polymer segments, which can make the wrapping polymer displaying more complicated conformational structures [12, 76, 47]. One important feature of this system, is the coupling of the segmental orientational properties with the positional properties, which can be compared to bulk states observed in lyotropic wormlike polymer systems, where the orientational and positional properties are not necessarily coupled [61].

Within the parameter region $\ell_p \gg R$, Spakowitz and Wang [77] investigated this model and provided an analytical expression for the mean-square end-to-end

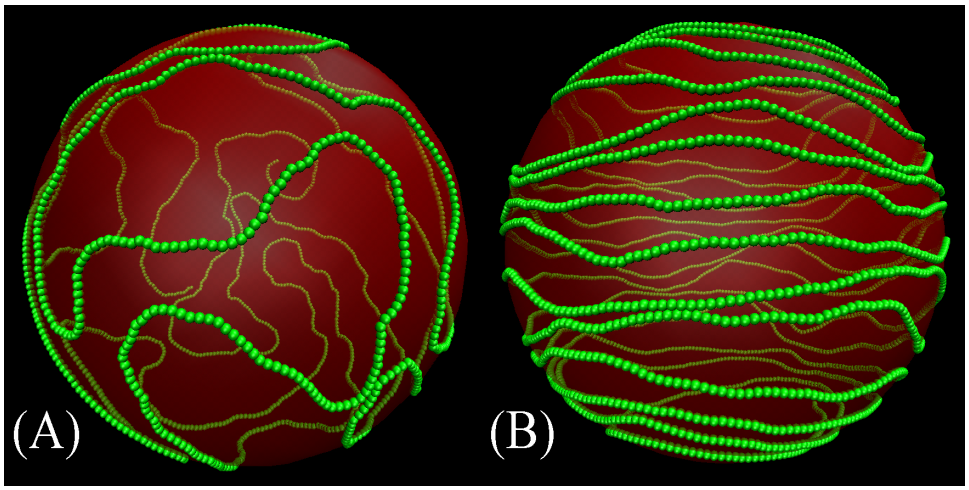

Figure 3.1: (A) Simulation snapshot for an isotropic state and (B) a highly helicoidal state (which actually contains a weak tennis-ball texture).

distance of a semiflexible chain without the excluded volume interaction. They found that the chain tends to lie near the equator region of the spherical surface due to the orientational correlation, which was also supported by a recent computer simulation [43]. A similar observation was also made by Morrison and Thirumalai [57] who went further to analytically study a noninteracting wormlike chain confined to the interior of a spherical cavity.

An interesting but less investigated parameter region is $\ell_p \leq R$ with length scales more relevant to the DNA packaging problem, since the persistence length of DNA [11] and the scale of bacteriophage capsid shell [64] are around 50nm. The bending energy of a semiflexible chain normally creates an orientational correlation typically persistent along the chain within a distance of a few ℓ_p. Any spacial and orientational ordering would have been lost after the chain wraps around the sphere, forming an isotropic state [Fig. 3.1(A)]. In this chapter, we demonstrate that the excluded-volume interaction is responsible for the formation of an ordered anisotropic state, in analogy to the isotropic-nematic phase transition of a two-dimensional polymer liquid crystal, at a relatively high surface density.

Qualitatively, we expect that a helicoidal-like configuration (a resembling snapshot of the Monte Carlo simulation is given in Fig. 3.1(B)) could occur at high

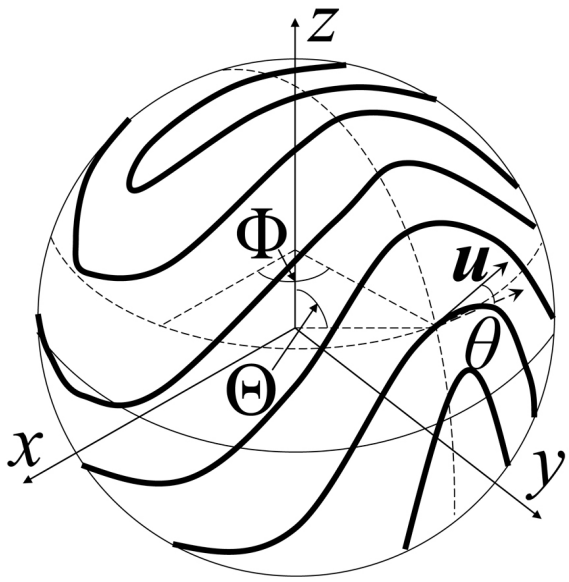

Figure 3.2: The illustration of the tennis-ball conformation is given with the definition of the coordinate system. Note that the fluctuations in segmental displacements of a Monte Carlo snapshot obscure the tennis-ball symmetry. After $x-$, $y-$, and $z-$ axes are selected, the location of a polymer segment is given by the polar angle Θ and azimuthal angle Φ, and the orientation of this segment by the angle between the bond vector $\mathbf{u}$ and a latitude circle.

surface coverage where the polymer forms a tight spacial packing arrangement. If the configuration were perfectly helicoidal, the terminal ends of the polymer would appear in the north and south poles and the entire polymer would wrap the surface with almost perfect circular configurations. In a related system of small rigid rod-like molecules confined to the surface of a sphere, liquid-crystal theories indicated that the high-density anisotropic state could be a tennis-ball state (Fig. 3.2), where the orientation pattern of molecules makes the system to display a partial tetrahedron symmetry [58]. In a coordinate system where the location of a point on the spherical surface is specified by the polar and azimuthal angles, Θ and Φ, the coupled positional and orientational distribution function $\varrho(\Theta, \Phi; \theta)$, where θ, the angle that $\mathbf{u}$ makes with respect to local latitude, is a local variable that specifies the molecular orientation at Θ and Φ, satisfies the tennis-ball symmetry properties (Appendix B),

$$\begin{aligned} &\varrho(\Theta, \Phi; \theta) = \varrho(\Theta, 2\pi - \Phi; \pi - \theta) = \varrho(\Theta, \Phi; \pi + \theta) = \\ &\varrho(\Theta, \pi + \Phi; \theta) = \varrho(\pi - \Theta, \pi/2 + \Phi; -\theta). \end{aligned} \tag{3.1}$$

Therefore, an interesting question is: for the system of a polymer confined to a spherical surface at high surface coverage, is the anisotropic state helicoidal or tennis-ball like? Recent Monte Carlo simulation studies of polyelectrolyte adsorbed on an oppositely charged spherical particle [87, 80] have indicated the formation of a tennis-ball state. It has been further speculated that the tennis-ball state may exist, probably as a precursor to a perfect helicoidal state[20]. There is, however, no effort spent on proving that the segmental distribution function displays the anticipated symmetry in Eq. 3.1 — a crucial step to recognize a tennis-ball state.

In this chapter, using Monte Carlo simulations [Sect. 3.2] we focus on the study of the conformation of a wormlike chain confined to a spherical surface, taking into account the excluded-volume interaction. For the purpose of distinguishing the isotropic and anisotropic conformations of the confined polymer, we pay attention to the orientational distribution of the polymer segments instead of properties such as the mean square end-to-end distance discussed in Refs [77, 12]. Analyzing several different order parameters, two of which are particularly designed to handle the tennis-ball state, we provide concrete evidence that shows [Sect. 3.3.1 and 3.3.2]

(a) there is an isotropic-anisotropic transition at relatively high surface segmental density, (b) the anisotropic state has the symmetry properties of a tennis-ball state (Eq. 3.1), and (c) there is no separate perfect helicoidal state in the system. Moreover, the isotropic-anisotropic transition is proved to have first-order characteristics [Sect. 3.3.3].

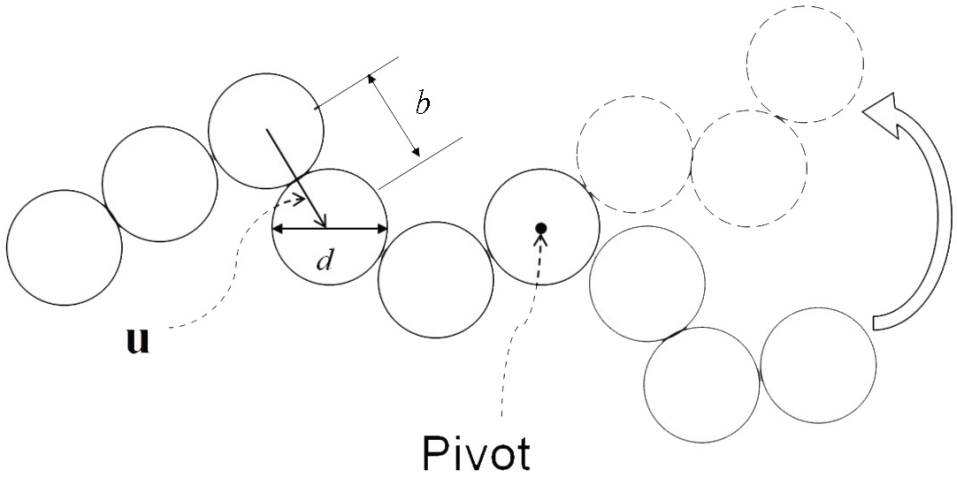

Figure 3.3: The bead-bond model of polymer chain include $N_b + 1$ beads and N_b bonds with the bead diameter d and bond length b. In this thesis, it is fixed that $d = b$.

3.2 Bead-bond Model and Monte Carlo Simulation

We consider a semiflexible-chain model containing N_b+1 monomers (beads) linearly connected by bonds of length b (Fig. 3.3) [9]. To model the semiflexibility a bending energy ε is invoked for two connected bonds and the total bending energy of the system is,

$$V = \frac{\varepsilon}{2} \sum_{i=1}^{N_b-1} |\mathbf{u}_{i+1} - \mathbf{u}_i|^2, \tag{3.2}$$

where $\mathbf{u}_i$ is the bond vector, pointing from the i-th to the $(i + 1)$-th monomer. We also assume that every monomer has a hard diameter of $d = b$, in order to simulate the effects of the excluded-volume interaction. All monomers are allowed to move only on the surface of a sphere having radius R. It turns out that when a semiflexible chain is confined in a two-dimensional space, as long as $\ell_p \gg d$, the magnitude of d has little influence on results considered in this chapter. The choice

of $d = b$ prevents intersecting of polymer segments.

In the Monte Carlo simulations, we implemented the pivot algorithm [45], which has the promise of efficiently driving the simulated polymer into uncorrelated configurations. Besides, for the purpose of efficiently checking the overlap of any two beads with diameter d, the neighbor-list algorithm is also implemented [2]. At a Monte Carlo step (MCS), we randomly selected a monomer dividing the polymer into smaller and bigger portions; we considered the vector from the center of the sphere to the selected monomer to be the rotation axis, against which the entire smaller portion of the polymer was rotated by a random small angle. Note that this maintains the fact that rotated monomers are still located on the surface of the sphere (Fig. 3.3). Such a Monte Carlo move was then evaluated by both the excluded-volume condition and the Metropolis transition probability [45] associated with the bending energy V (Eq. 3.2). Using the data blocking method, we found that the longest correlation time of the studied systems is approximately 10^5 MCS. At the beginning of each Monte Carlo simulation, we generated a preliminary configuration of a self-avoiding polymer and equilibrated the system with 10^6 MCS before taking statistical measurements. Typical data points shown in Figs. 3.4-3.13 were produced by measurements accumulated from 10^7 MCS in a production run.

The consideration of the overall positional and orientational dependence of the chain formation requires us to redefine a suitable coordinate system for every new configuration generated. While the simulation was done on a static coordinate system, during the course of a Monte Carlo run, the entire chain moves on the spherical surface and the desired symmetry axes associated with the conformational properties drift together with the chain motion. Within a new coordinate system where the symmetry properties are maintained (Fig. 3.2), we need to specify the location of the i-th bond (described by the polar and azimuthal angles, Θ_i and Φ_i) and the the associated orientation (described by the angle θ_i that $\mathbf{u}_i$ makes with respect to a latitude circle). The selection of a new z-direction as a reference axis becomes a critical step in determination of Θ_i for bond i. In this work, we defined the z-axis of a configuration to coincide with the vector

$$\mathbf{w} = \frac{1}{N_b - 1} \sum_{i=1}^{N_b - 1} \left(\frac{\mathbf{u}_i \times \mathbf{u}_{i+1}}{|\mathbf{u}_i \times \mathbf{u}_{i+1}|} \right), \tag{3.3}$$

which is invariant with respect to the choice of the static coordinate system. In a perfect helicoidal configuration, directions of the unit vectors defined by the above parentheses converge to one direction, i.e., the new z-axis. The selection of the z-axis allows the definition of a helicoidal order parameter

$$S = \frac{1}{N_b}\sum_{i=1}^{N_b}\cos 2\theta_i = \frac{1}{N_b}\sum_{i=1}^{N_b}\Big\{2\big[\mathbf{u}_i\cdot\hat{\Phi}(\Theta_i,\Phi_i)\big]^2 - 1\Big\}. \tag{3.4}$$

One can also show that in an isotropic state where $\mathbf{u}_i$ vectors are random, the above definition yields a vanishing S for large N_b, and that in a helicoidal or tennis-ball state, S in nonzero. None of these two, $\mathbf{w}$ or S, can be used to distinguish a tennis-ball structure from a perfect helicoidal structure.

To uniquely pin-point the existence of a tennis-ball state, two additional order parameters are defined for the tennis-ball texture in this work. The selection of the z-axis determines the location of the north and south poles of the sphere, but the order parameters for a tennis-ball state also require the determination of the azimuthal angle Φ_i for bond i which consequently requires the selection of the x-axis. For this purpose, we divide the spherical surface into north and south hemispheres cutting across the equator plane. As the first step, all bond vectors $\mathbf{u}_i$ in the north hemisphere were projected onto the equator plane to form a new set of two-dimensional vectors, $\mathbf{v}_i$; renormalization was then performed to ensure that each $\mathbf{v}_i$ is a unit vector. A 2×2 traceless matrix was constructed following the normalization,

$$\mathcal{B} = \frac{1}{M}\sum_i\left(2\mathbf{v}_i\mathbf{v}_i - \mathbf{I}\right), \tag{3.5}$$

where the summation runs over all polymer bonds in the north hemisphere, M is the total number of these bonds, and $\mathbf{I}$ is a 2×2 identity matrix. The eigenvector of $\mathcal{B}$ corresponding to the positive eigenvalue defines a new unit vector $\mathbf{A}_{\mathrm{N}}$ lying on the equator plane. A similar procedure analyzing bond vectors in the south hemisphere yields another unit vector $\mathbf{A}_{\mathrm{S}}$. A tennis-ball *axial* order parameter can then be defined,

$$P = 2\left|\mathbf{A}_{\mathrm{N}}\times\mathbf{A}_{\mathrm{S}}\right|^2 - 1. \tag{3.6}$$

In an ideal tennis-ball phase, $\mathbf{A}_{\mathrm{N}}$ and $\mathbf{A}_{\mathrm{S}}$ are always perpendicular to each other, hence $\langle P\rangle = 1$. In an isotropic or perfect helicoidal phase, $\langle P\rangle = 0$. Here and in the

rest of this chapter, $\langle \cdots \rangle$ represents the overall statistical average obtained from the Monte Carlo measurements.

We also introduce a second tennis-ball order parameter, used to reveal the magnitude of the tennis-ball order, directly from

$$\tau = \frac{1}{N_b} \sum_{i=1}^{N_b} P_2^2(\cos \Theta_i) \sin 2\Phi_i \sin 2\theta_i, \tag{3.7}$$

where P_l^m is the (l, m)-th rank associated Legendre function [4]. This definition contains leading factors, in terms of a combined spherical-harmonic expansion and Fourier expansion, that survive from the symmetry operation given in Eq. 3.1. To use the definition, the x-axis (hence the Φ_i measurement) was identified in our simulation to be along the direction of $\mathbf{A}_{\mathrm{N}}$. The coupled position and direction order in a tennis-ball phase is reflected by the presence of all three variables, Θ_i, Φ_i, and θ_i, in the above definition.

One can show through an analytic treatment that the persistence length $\ell_p = 2\beta\varepsilon b$ for a wormlike chain (without the excluded-volume interaction) embedded in a flat two-dimensional space (see Appendix E), which can be contrasted with $\ell_p = \beta\varepsilon b$ in a three-dimensional space [72]. We use a bare persistence length

$$\ell_p = 2\beta\varepsilon b \tag{3.8}$$

in the following analysis; although strictly speaking a spherical surface is different from a flat surface.

In the model here, there are three important length scales specifying the system, the total length of the polymer $L = N_b b$, the radius of the confining sphere R, and the reduced bending energy $\beta\varepsilon$ defining a bare persistence length ℓ_p. The anisotropic ordering in this lyotropic system is driven by an increasing number of persistent segments per unit area, $\rho = (L/\ell_p)/(4\pi R^2)$, in the same spirit as the formation of the nematic state in a flat, two-dimensional lyotropic system [61, 27]. Consider two segments of persistence length ℓ_p; the excluded-volume interaction between monomers in the system manifests itself into an excluded area, with an average size of order ℓ_p^2. Note that this size is independent of the monomer excluding diameter d in the limit of $\ell_p \gg d$; most cases considered in this work are within this

approximation. Hence, the relevant physical quantity in this system is the reduced segment density $\rho\ell_p^2$, which can also be written as

$$\rho\ell_p^2 = \frac{1}{4\pi}\frac{L}{R}\frac{\ell_p}{R}, \tag{3.9}$$

proportional to the product of two ratios, L/R and ℓ_p/R. The fact that $\rho\ell_p^2$ is the relevant physical quantity can also be shown more rigorously through an analytic treatment based on the Onsager interaction of polymer segments [90].

3.3 Results

3.3.1 Order parameters

We conducted a separate Monte Carlo simulation for a given set of three parameters L, R, and ℓ_p. In the following we analyze the data by organizing the data points that have a fixed ratio L/R and examine the behavior of order parameters $\langle S\rangle$, $\langle P\rangle$, and $\langle\tau\rangle$ and the second moment $\langle S^2\rangle - \langle S\rangle^2$ as functions of the reduced density $\rho\ell_p^2$ or equivalently as functions of ℓ_p/R. As an example we show in Fig. 3.4 the data for $L/R = 10$, produced from $[N_b, R/b] = [100, 10]$, $[200, 20]$, $[300, 30]$, and $[400, 40]$. The four sets of data of different $[N_b, R/b]$ asymptotically approach a common trend (valid for a "continuous" polymer chain at $R/b \gg 1$) as the system grows (N_b increases) and finite size effects reduce. Similar plots are also available for $L/R = 20, 30, 40, 50, 60, 70, 80, 90$, and 100 (Figs. 3.5-3.13), each producing an asymptotic curve unique to a given value of L/R.

A number of interesting physical features emerge from this analysis. In the low-density regime $\langle S\rangle$ is close to 0, corresponding to an isotropic state; beyond a transition region in density $\langle S\rangle$ increases significantly, indicating the formation of an anisotropic state. Moreover, in high-density regime, $\langle S\rangle$ is close to 1, which demonstrates a near-helicoidal conformation. In a system where $\ell_p \gg R$, the correlation between segmental orientations can persist in a few rounds of wrapping [77, 57, 12, 43]. This can be used to, for example, qualitatively interpret the wrapping of DNA around histone where the persistence length of DNA is around 50nm [11] and the radius of histone is around 5nm[39, 24]. Our numerical evidence above shows that in systems where $\ell_p \lesssim R$, an anisotropic state can also form, driven by the excluded-volume interaction, not the orientational correlation. An example is the system $L/R = 100$ where the isotropic-anisotropic transition occurs approximately at $\ell_p/R \approx 0.6$. Although the study in this thesis is for a polymer on a spherical surface, the observation can be compared to the conformation of a DNA molecule (with the persistence length approximately 50nm [11]) helically packaged in a capsid, where the length scale of a typical capsid is also around 50nm [23, 13].

From Figs. 3.4(B)-3.13(B) we can see that once the system enters into the

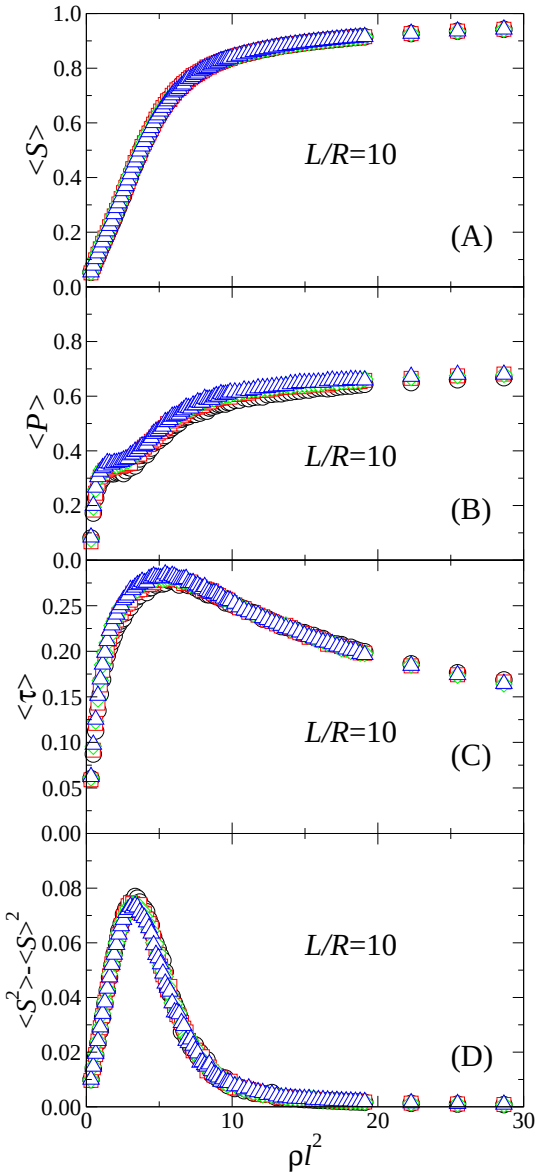

Figure 3.4: (A) Helicoidal order parameter $\langle S \rangle$, (B) tennis-ball axial parameter $\langle P \rangle$, (C) tennis-ball order parameter $\langle \tau \rangle$, and (D) second moment of S are plotted as functions of the reduced density $\rho \ell_p^2$ for the case $L/R = 10$. Four curves in each figure represent four different system sizes, respectively: black circles for $R = 10b$, rad squares for $R = 20b$, green diamonds for $R = 30b$, and blue triangles for $R = 40b$.

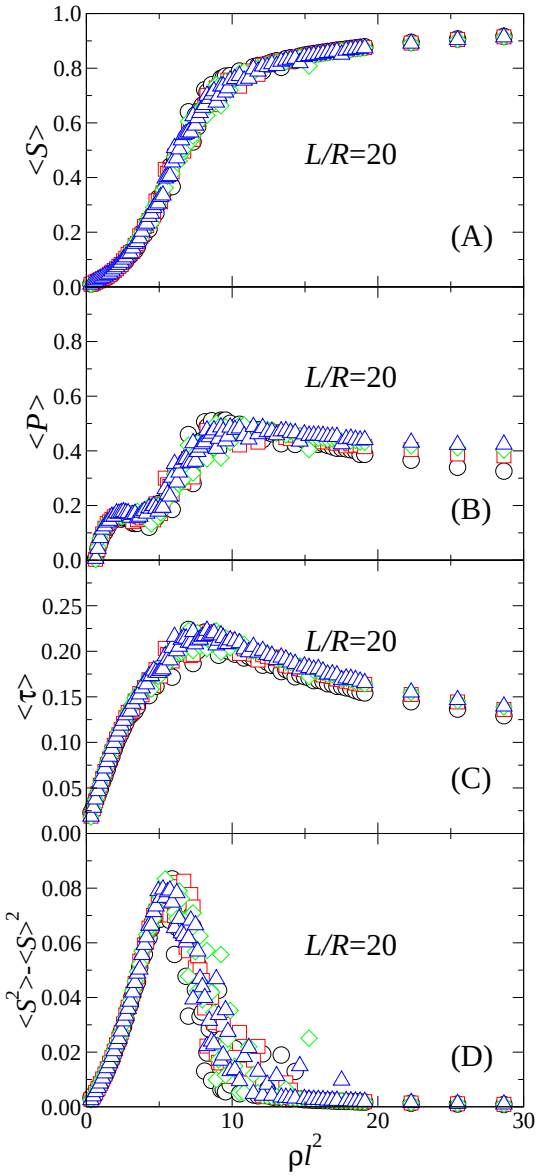

Figure 3.5: (A) Helicoidal order parameter $\langle S \rangle$, (B) tennis-ball axial parameter $\langle P \rangle$, (C) tennis-ball order parameter $\langle \tau \rangle$, and (D) second moment of S are plotted as functions of the reduced density $\rho \ell_p^2$ for the case $L/R = 20$. Four curves in each figure represent four different system sizes, respectively: black circles for $R = 10b$, rad squares for $R = 20b$, green diamonds for $R = 30b$, and blue triangles for $R = 40b$.

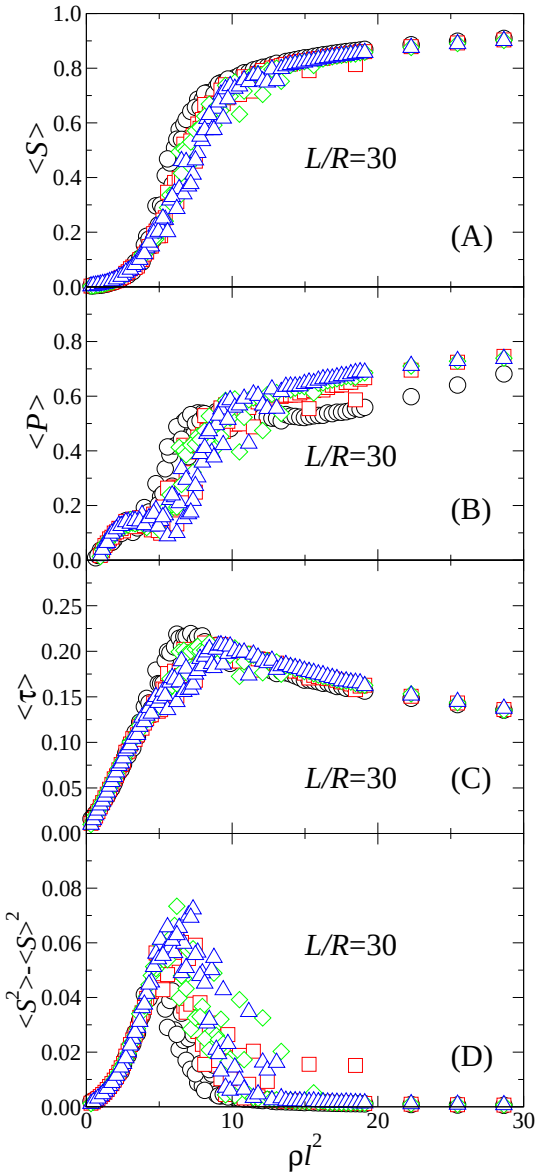

Figure 3.6: (A) Helicoidal order parameter $\langle S \rangle$, (B) tennis-ball axial parameter $\langle P \rangle$, (C) tennis-ball order parameter $\langle \tau \rangle$, and (D) second moment of S are plotted as functions of the reduced density $\rho \ell_p^2$ for the case $L/R = 30$. Four curves in each figure represent four different system sizes, respectively: black circles for $R = 10b$, rad squares for $R = 20b$, green diamonds for $R = 30b$, and blue triangles for $R = 40b$.

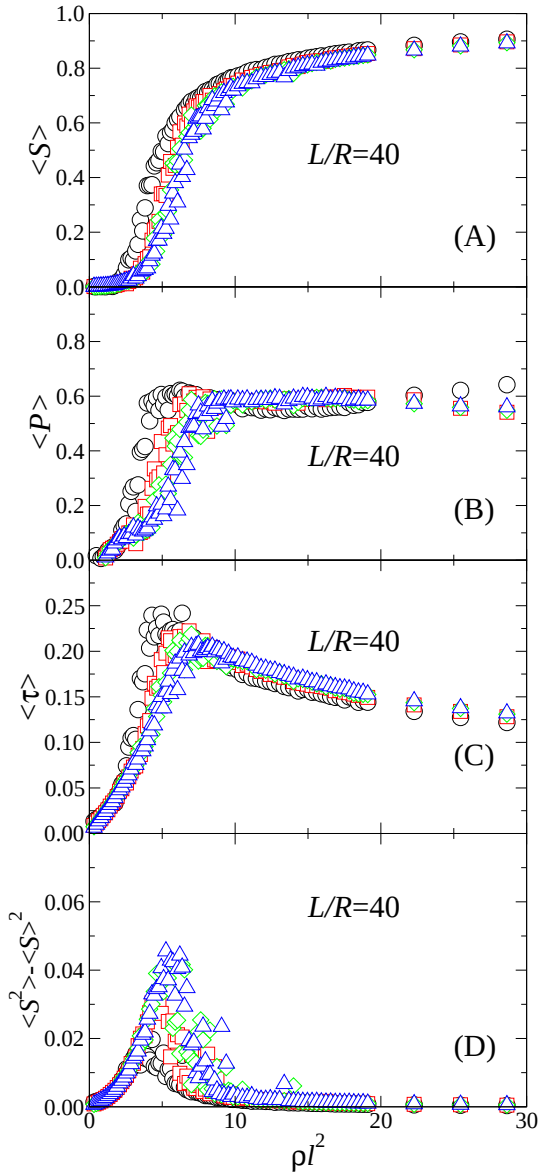

Figure 3.7: (A) Helicoidal order parameter $\langle S \rangle$, (B) tennis-ball axial parameter $\langle P \rangle$, (C) tennis-ball order parameter $\langle \tau \rangle$, and (D) second moment of S are plotted as functions of the reduced density $\rho \ell_p^2$ for the case $L/R = 40$. Four curves in each figure represent four different system sizes, respectively: black circles for $R = 10b$, rad squares for $R = 20b$, green diamonds for $R = 30b$, and blue triangles for $R = 40b$.

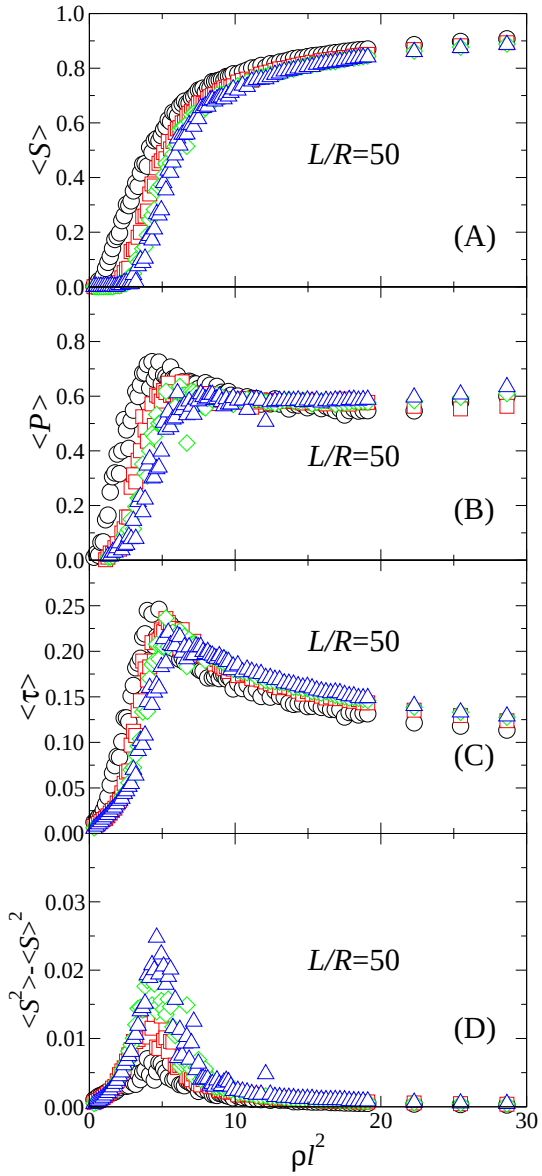

Figure 3.8: (A) Helicoidal order parameter $\langle S \rangle$, (B) tennis-ball axial parameter $\langle P \rangle$, (C) tennis-ball order parameter $\langle \tau \rangle$, and (D) second moment of S are plotted as functions of the reduced density $\rho \ell_p^2$ for the case $L/R = 50$. Four curves in each figure represent four different system sizes, respectively: black circles for $R = 10b$, rad squares for $R = 20b$, green diamonds for $R = 30b$, and blue triangles for $R = 40b$.

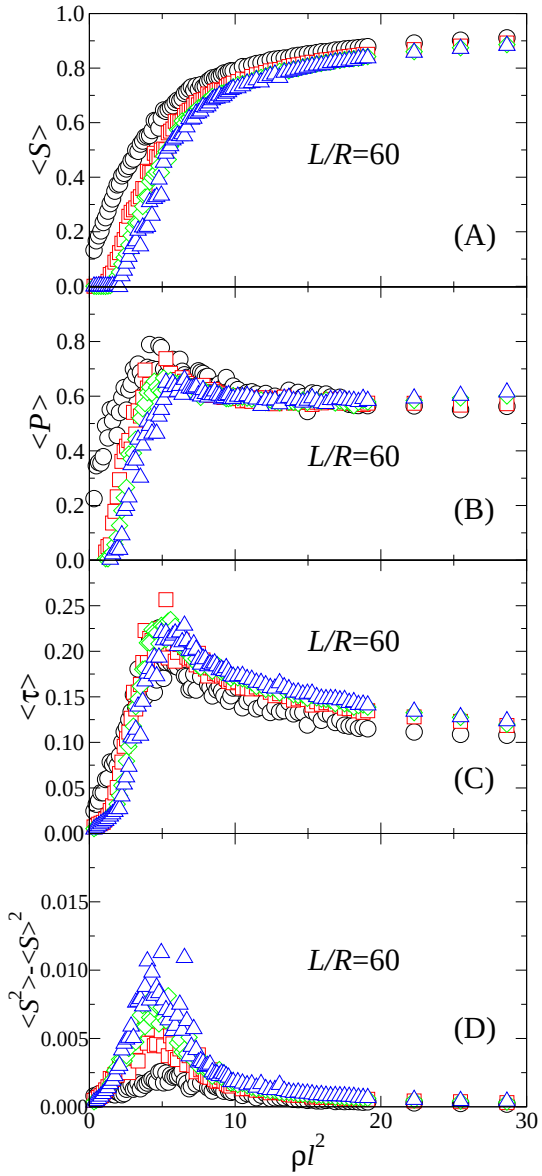

Figure 3.9: (A) Helicoidal order parameter $\langle S \rangle$, (B) tennis-ball axial parameter $\langle P \rangle$, (C) tennis-ball order parameter $\langle \tau \rangle$, and (D) second moment of S are plotted as functions of the reduced density $\rho \ell_p^2$ for the case $L/R = 60$. Four curves in each figure represent four different system sizes, respectively: black circles for $R = 10b$, rad squares for $R = 20b$, green diamonds for $R = 30b$, and blue triangles for $R = 40b$.

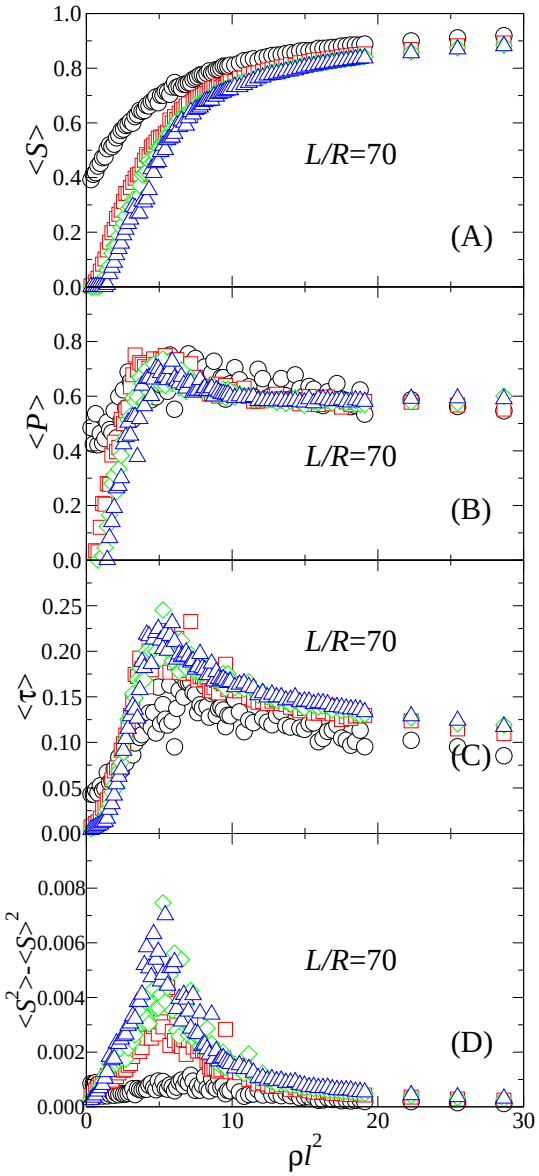

Figure 3.10: (A) Helicoidal order parameter $\langle S \rangle$, (B) tennis-ball axial parameter $\langle P \rangle$, (C) tennis-ball order parameter $\langle \tau \rangle$, and (D) second moment of S are plotted as functions of the reduced density $\rho \ell_p^2$ for the case $L/R = 70$. Four curves in each figure represent four different system sizes, respectively: black circles for $R = 10b$, rad squares for $R = 20b$, green diamonds for $R = 30b$, and blue triangles for $R = 40b$.

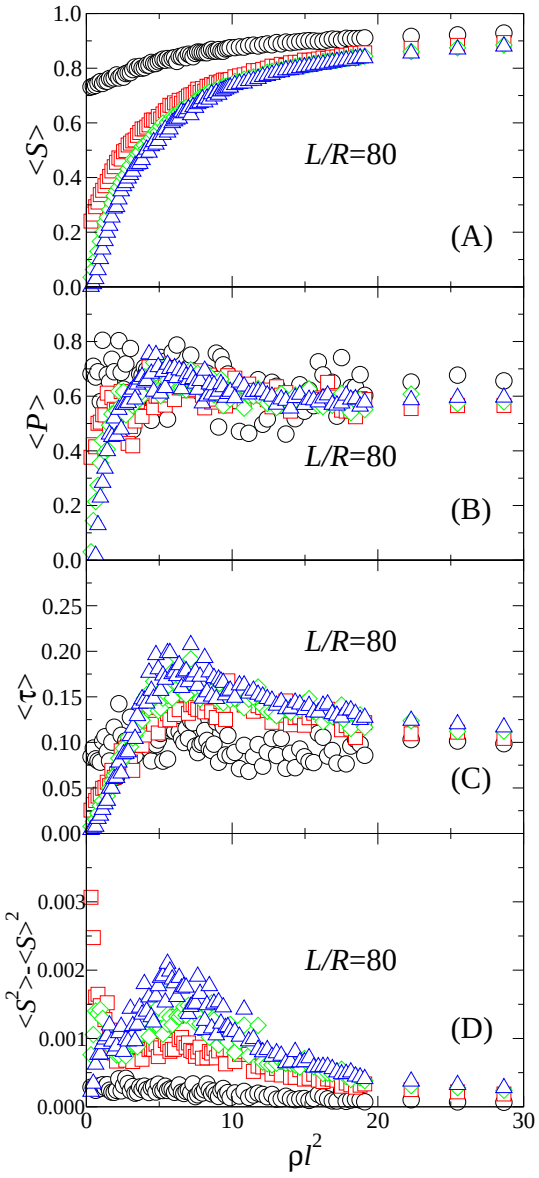

Figure 3.11: (A) Helicoidal order parameter $\langle S \rangle$, (B) tennis-ball axial parameter $\langle P \rangle$, (C) tennis-ball order parameter $\langle \tau \rangle$, and (D) second moment of S are plotted as functions of the reduced density $\rho \ell_p^2$ for the case $L/R = 80$. Four curves in each figure represent four different system sizes, respectively: black circles for $R = 10b$, rad squares for $R = 20b$, green diamonds for $R = 30b$, and blue triangles for $R = 40b$.

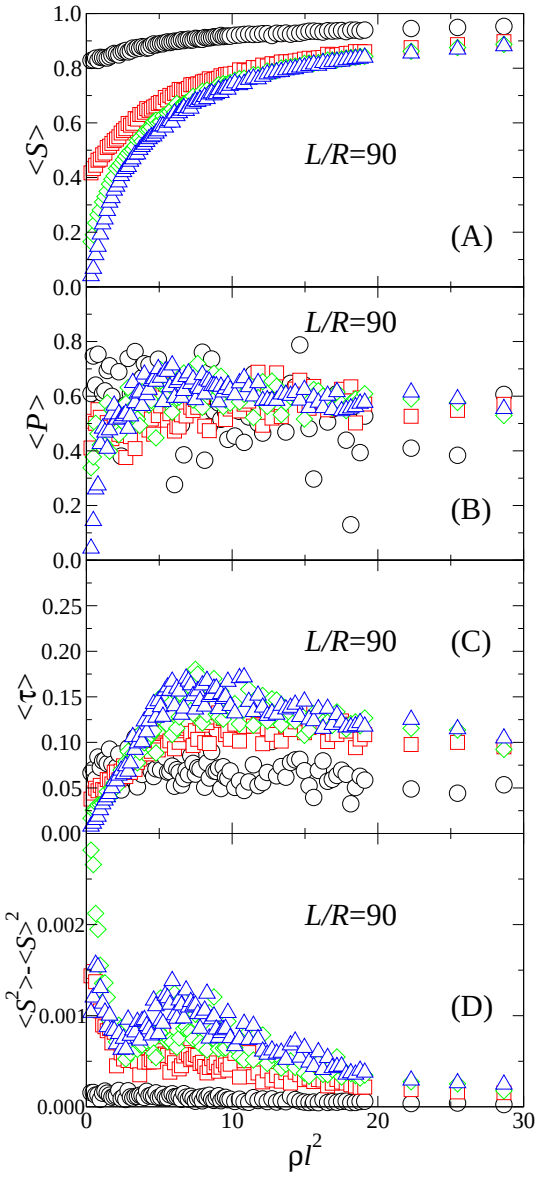

Figure 3.12: (A) Helicoidal order parameter $\langle S \rangle$, (B) tennis-ball axial parameter $\langle P \rangle$, (C) tennis-ball order parameter $\langle \tau \rangle$, and (D) second moment of S are plotted as functions of the reduced density $\rho \ell_p^2$ for the case $L/R = 90$. Four curves in each figure represent four different system sizes, respectively: black circles for $R = 10b$, rad squares for $R = 20b$, green diamonds for $R = 30b$, and blue triangles for $R = 40b$.

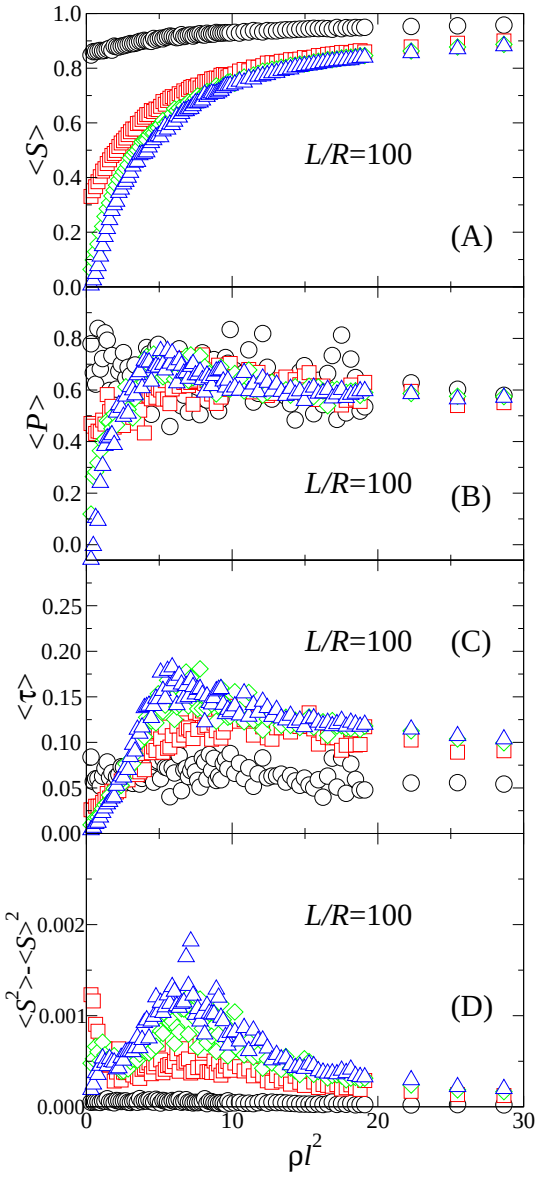

Figure 3.13: (A) Helicoidal order parameter $\langle S \rangle$, (B) tennis-ball axial parameter $\langle P \rangle$, (C) tennis-ball order parameter $\langle \tau \rangle$, and (D) second moment of S are plotted as functions of the reduced density $\rho \ell_p^2$ for the case $L/R = 100$. Four curves in each figure represent four different system sizes, respectively: black circles for $R = 10b$, rad squares for $R = 20b$, green diamonds for $R = 30b$, and blue triangles for $R = 40b$.

transition region from the low-density side, a small value of the tennis-ball axial order parameter $\langle P \rangle$ can be observed. Because of the renormalization procedure used in producing unit vectors $\mathbf{A}_{\mathrm{N}}$ and $\mathbf{A}_{\mathrm{S}}$, $\langle P \rangle$ has an artificial plateau in the transition region and jumps to a higher plateau after reaching the anisotropic region. As $\rho\ell_p^2$ increases further, passing the transition region, not only does the helicoidal order become intensified to accommodate the packing requirement of the polymer chain [Figs. 3.4(A)-3.13(A)], but the angle between $\mathbf{A}_{\mathrm{N}}$ and $\mathbf{A}_{\mathrm{S}}$ of the tennis-ball state in the north and south hemispheres also move towards a right angle, reflected by an increasing $\langle P \rangle$; note that as $P \geq 0.6$ the system actually has $|\mathbf{A}_{\mathrm{N}} \times \mathbf{A}_{\mathrm{S}}| \geq 0.9$. This indicates that *the anisotropic state always displays the tennis-ball symmetry.*

To examine the magnitude of the orientational property we use the tennis-ball order parameter $\langle \tau \rangle$ (Eq. 3.7), plotted in Figs. 3.4(C)-3.13(C) as a function of reduced density. In our definition, because the x-axis is always selected to be the eigenvector of the positive eigenvalue of $\mathcal{B}$ (Eq. 3.5), even in the isotropic region we already see a nonzero $\langle \tau \rangle$. Accompanying the increase of $\langle S \rangle$ and $\langle P \rangle$, $\langle \tau \rangle$ climbs to a maximal value in the transition region. No intermediate plateau such as the one in the axial order parameter, $\langle P \rangle$, is observable for $\langle \tau \rangle$ (Figs. 3.4(C)-3.13(C)). As $\rho\ell_p^2$ passes the transition region, the magnitude of the tennis-ball ordering, $\langle \tau \rangle$, starts to *decrease*, remaining significant in the entire anisotropic region. The gradual weakening of the tennis-ball texture is caused by the fact that polymer segments need to compress against each other further to accommodate the packing requirement in high reduced density. Such compression prefers a more perfect helicoidal configuration in high densities over a tennis-ball configuration which is less packing efficient.

3.3.2 Visualization of the tennis-ball conformation

To unveil the segmental conformation of the tennis-ball state in visualization, where the orientational property is coupled with positional coordinates, we plot the density distribution function, $\varrho(\Theta, \Phi; \theta)$ in a map form in Fig. 3.14. The distribution was taken from the Monte Carlo simulation measured from a system with parameters $N_b = 300, R = 10b, \ell_p = 26.4b$ and was normalized after integrating over all three

variables. This set of parameters corresponds to a reduced density $\rho\ell_p^2 \approx 6.3$, which is just beyond the transition density in Fig. 3.6. Fig. 3.14 contains 20×20 cells divided by black lines and each cell can be mapped back to the location Θ and Φ on the surface of a sphere (Fig. 3.14(inset)) by using the values of the vertical and horizontal coordinates in Fig. 3.14. Within every cell we consider the orientational distribution for the location about Θ and Φ; starting from the center of the cell we draw multiple radial staight lines where the angular spacing of these lines are uniform; each line corresponds to given value of θ, specifying the angle between the line and the positive horizontal axis; for illustration purpose we have also used a color code to draw these lines according to the magnitude of $\varrho(\Theta, \Phi; \theta)$: red, yellow, green, cyan, and blue colors correspond to very strong, strong, intermediate, weak, and very weak ϱ. At $\Phi = 0$, $\pi/2$, and π, the segments prefer an alignment along $\theta = 0$. In the region of $\Phi = (0, \pi/4)$, the segments prefer an alignment in a direction of nonzero θ, which goes up from 0 to a nontrivial value; in the region of $\Phi = (\pi/4, \pi/2)$, the alignment direction is also nonzero and eventually goes back to $\theta = 0$. The equator region $\Theta \sim \pi/2$ is where these directional alignments display the most anisotropic texture. The distribution function obtained from the simulation follows the symmetry properties described by Eq. 3.1, which are the characteristics of a tennis-ball texture.

3.3.3 Isotropic-anisotropic transition

The transition region between the isotropic and anisotropic states in Figs. 3.4(A)-3.13(A) is narrow but not trivially small. To study the order of the phase transition, in Fig. 3.15(A), we further plot the distribution function $h(S)$ collected from Monte Carlo simulations for various values of the density across the transition region. The distribution of S has only one peak in the relatively low or high densities, and there is a crossover between these peaks in the transition region. This behavior is even more revealing in Fig. 3.15(B), where the distribution function $g(|\mathbf{w}|)$ is plotted. Note that $|\mathbf{w}|$ is always positive by definition and therefore has a residual positive value in the isotropic phase. In the transition region, the distribution distinctively displays two peaks, which can be labeled isotropic and anisotropic, respectively. Such a two-peak distribution is commonly seen in a first-order phase transition.

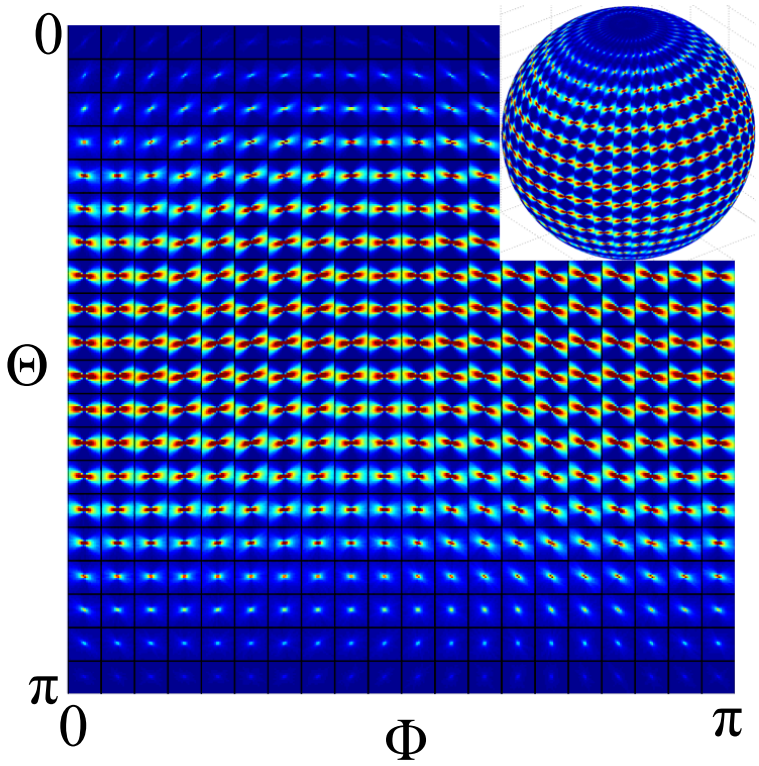

Figure 3.14: Monte Carlo result for the segmental density distribution function $\varrho(\Theta, \Phi; \theta)$ plotted in a $[\Theta, \Phi]$ map divided into cells by black lines for $\rho\ell_p^2 = 6.3$ and $L/R = 30$. The map repeats in the $\Phi = [\pi, 2\pi]$ region almost identically. Within each cell, the direction of the orientational preference is visualized by using a color scheme (see text). This figure demonstrates a tennis-ball state found in the simulations.

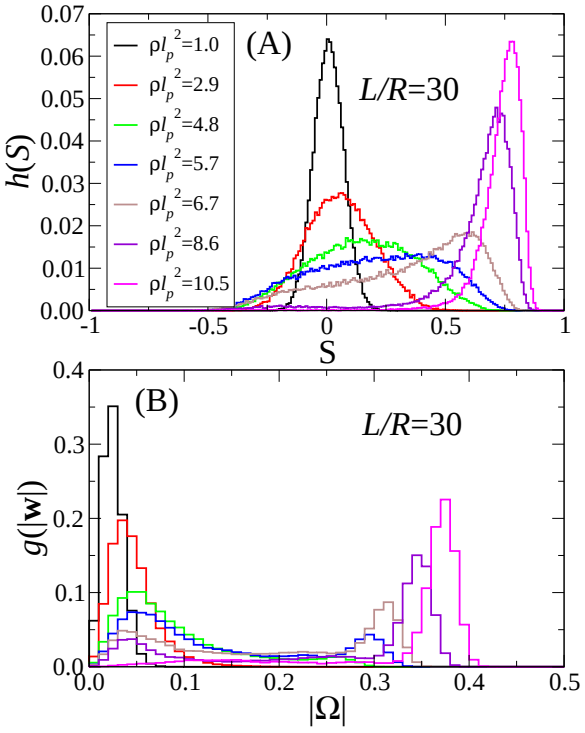

Figure 3.15: Probability distributions of (A) S and (B) $|\mathbf{w}|$ for the case $L/R = 30$.

Hence, the isotropic-anisotropic transition observed in this work has a first-order phase transition characteristic.

In an isotropic-nematic transition, two characteristic densities, one representing the isotropic state and the other nematic state, are identified at the first-order transition boundary [34]. In the current system we should have determined two transition densities in a similar way. These densities correspond to the beginning and ending points of the transition region in plots such as Figs. 3.4(A, B, C)-3.13(A, B, C). Because of less-than-ideal data points in Fig. 3.4(A, B, C)-3.13(A, B, C), we opt to determine of a characteristic transition density, $\rho_c \ell_p^2$, from the peak location of $\langle S^2 \rangle - \langle S \rangle^2$, given in Figs. 3.4(D)-3.13(D).

From an analysis based on a mean-field theory of the current system, we can show that $\rho_c \ell_p^2$ is a universal constant, independent of both L/R and ℓ/R in the system, as long as L/R is relatively large and ℓ_p/R relatively small. In Fig. 2.27 we display the characteristic transition density $\rho_c \ell_p^2$ for all L/R cases considered in

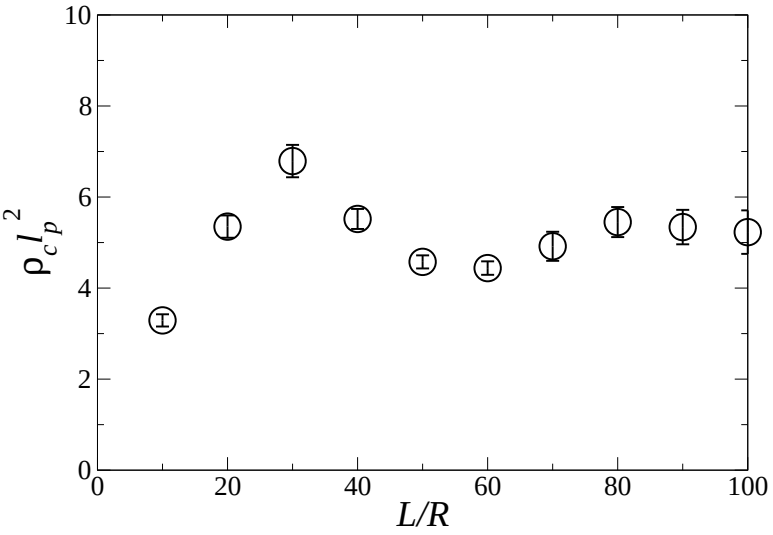

Figure 3.16: Reduced transition density $\rho_c \ell_p^2$ as a function of L/R.

this work, with error estimates. The data points for the large L/R systems indeed approach an asymptotically common value.

If we conceptually regard the polymer chain as a collection of fragments of length ℓ_p, the isotropic-anisotropic transition point can be qualitatively compared with a fluid of hard rods in a flat two-dimensional space. Using Monte Carlo simulations, Frenkel et. al. [27] demonstrated that the isotropic-nematic phase transition of a two-dimensional fluid of hard rods is a Kosterlitz-Thouless transition occurring at $\rho_c \ell_p^2 \approx 7$. The mean field theory predicts the critical density $\rho_c \ell_p^2 = 3\pi/2 \approx 4.7$ [33] for rods, and $\rho_c \ell_p^2 = 6\pi$ for long wormlike chains [15]. Our determination of $\rho_c \ell_p^2$ in Fig. 2.27 is comparable to these values.

Angelescu et. al. [20] have recently studied a system similar to that in this chapter, where they have further added electrostatic interaction between monomers. A transition to an anisotropic state was also observed; through an analysis of $|\mathbf{\Omega}|$, they claimed that their observed anisotropic state is a tennis-phase. As stressed earlier in this letter, the definition of $\mathbf{w}$ lacks the tennis-ball symmetries listed in Eq. 3.1 hence cannot be used for distinguishing the tennis-ball symmetry from a helicoidal symmetry.

3.4 Conclusion

In this chapter, we investigated the equilibrium conformations of a self-avoiding semiflexible polymer chain confined to a spherical surface using Monte Carlo simulations; we concluded that an anisotropic state exists at a sufficiently high surface density. The transition can occur at physical parameters where the orientational correlation in a wormlike chain due to persistency is no longer important; the transition is entirely caused by the excluded-volume interaction. In the anisotropic state, the polymer chain always wraps around the spherical surface in a tennis-ball configuration, which is a distortion of a helicoidal configuration. The analysis was performed in light of the symmetry properties of these states.

Chapter 4

Towards a Perfect Tetrahedral Tennis-ball Configuration

4.1 Introduction

Nelson suggested the tetrahedral tennis-ball configurations on the basis of the one Frank constant approximation, $K_1 \approx K_3$, applied to the Frank continuum theory [58]. However, according to the discussions in Chapter 2, we ruled out the existence of tennis-ball configurations for *rigid* rods confined on a spherical surface, because the Frank constants of rigid rods have $K_1 \ll K_3$ [81, 73] which is not consistent with the one Frank constant approximation. Meanwhile, for the long self-avoiding wormlike chain confined on a spherical surface discussed in Chapter 3, although the semiflexibility of the chain reduces the tennis-ball symmetry, the perfect tetrahedral tennis-ball configuration could not be achieved since we have approached another limit of $K_1 \gg K_3$ for long polymer chains [41]. Therefore, to build up the tetrahedral tennis-ball configurations of particular interest, we must consider a system of semiflexible polymer chains on a spherical surface. The reason is that, if the persistence length of a semiflexible chain is comparable to its contour length, $K_1 \approx K_3$ is possibly satisfied. To model the system of semiflexible polymer chains, we have two approaches, Monte Carlo simulation on the wormlike chains discussed in Chapter 3 and Onsager model discussed in Chapter 2.

4.2 Monte Carlo simulation on wormlike chains confined to a spherical surface

On the basis of bead-bond model discussed in Chapter 3, we may also consider the system of many semiflexible chains with the contour length L and persistence length ℓ_p for each chain. We conducted Monte Carlo simulations on such system of N chains confined on a spherical surface with the radius surface $R = 40b$, where b is the length of a bond as the unit of length in this research. The persistence length of each chain is fixed at $\ell_p = 80b$; the contour length L of each chain can be altered, $L = N_b b$, while keeping $NL \approx 4000b$ approximately fixed, where N_b is the number of bonds per chain.

For a perfect tetrahedral tennis-ball configuration, the bond vectors, $\mathbf{u}$'s, also form a tetrahedron. Therefore, to measure the tetrahedral symmetry of the tennis-ball configuration, we build up the tetrahedral parameter Q_3 [78],

$$Q_3 = \left[\frac{4\pi}{7} \sum_{m=-3}^{3} \left| \bar{Q}_{3m} \right|^2 \right]^{1/2}, \tag{4.1}$$

which is invariant to the coordinate system. In the above, $\left| \bar{Q}_{lm} \right|$ is the averaged spherical harmonics with the index $l = 3$,

$$\left| \bar{Q}_{lm} \right| = \frac{1}{N_b} \sum_{i=1}^{N_b} \left| Y_{lm}(\mathbf{u}) \right|. \tag{4.2}$$

According to Fig. 4.1 where Q_3 is plotted as a function of the ratio L/ℓ_p, we can find a peak around $L/\ell_p = 1$. The fact indicates that the configuration of semiflexible chains is closest to perfectly tetrahedral tennis-ball if ℓ is comparable to ℓ_p. We also plot a snapshot the data point shown in Fig. 4.1 at $L/\ell_p = 1$ in Fig. 4.2, where we can locate four defects on the four vertices of a tetrahedron. This perfect tetrahedral tennis-ball configuration hasn't been encountered with chain model before.

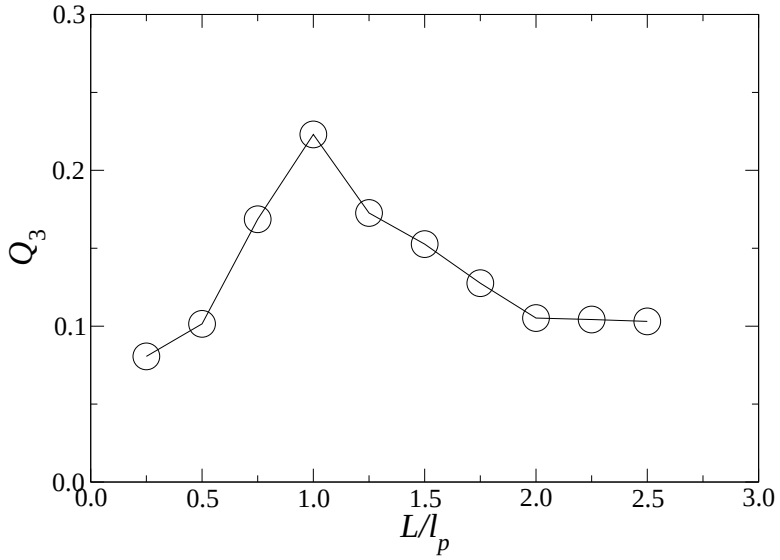

Figure 4.1: The tetrahedral parameter Q_3 is plotted as a function of L/ℓ_p for a case of $R = 40b$, $\ell_p = 60b$, and $NL \approx 4000b$.

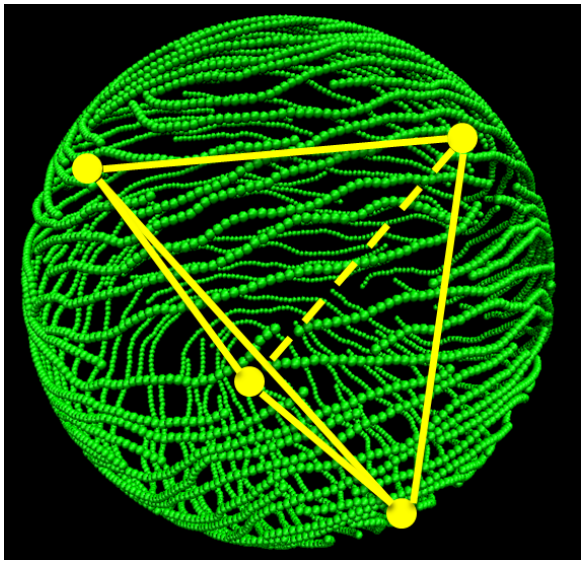

Figure 4.2: A snapshot of Monte Carlo simulation for semiflexible chains confined on a spherical surface with $L = \ell_p = 60b$, $R = 40b$, and $N = 67$.

4.3 Onsager model on semiflexible chains on a spherical surface

4.3.1 Free energy functional and modified diffusion equation

Based on the Onsager model, the free energy functional of a system of N semiflexible polymer chains can be written as,

$$\beta F = \ln N! - N \ln Q - \int \varrho(\mathbf{r},\mathbf{u})\omega(\mathbf{r},\mathbf{u})\mathrm{d}\mathbf{r}\mathrm{d}\mathbf{u} + \frac{\ell_p^2}{2}\int \varrho(\mathbf{r},\mathbf{u})|\mathbf{u}\times\mathbf{u}'|\varrho(\mathbf{r},\mathbf{u}')\mathrm{d}\mathbf{r}\mathrm{d}\mathbf{u}\mathrm{d}\mathbf{u}', \tag{4.3}$$

where Q is the partition function per chain and ℓ_p is the persistence length. Let L be the contour length of a chain, $N_p = L/\ell_p$ is the number of segments per chain. The position $\mathbf{r}$ of a segment can be defined by the solid angle Ω on the spherical surface with the radius R; the direction $\mathbf{u}$ as the tangent vector of a segment is described by the angle, θ, that $\mathbf{u}$ makes with respect to the latitudinal line. Therefore, the free energy can be rewritten in the chosen coordinate system,

$$\begin{aligned}\beta F = \ln N! - N\ln Q - R^2\int \varrho(\Omega,\theta)\omega(\Omega,\theta)\mathrm{d}\Omega\mathrm{d}\theta \\ + \frac{\ell_p^2 R^2}{2}\int \varrho(\Omega,\theta)\big|\sin(\theta-\theta')\big|\varrho(\Omega,\theta')\mathrm{d}\Omega\mathrm{d}\theta\mathrm{d}\theta'.\end{aligned} \tag{4.4}$$

In the above, the free energy is a functional of the density distribution function $\varrho(\Omega,\theta)$. Since the density distribution function ϱ satisfies the normalization,

$$R^2\int \varrho(\Omega,\theta)\mathrm{d}\Omega\mathrm{d}\theta = NN_p, \tag{4.5}$$

we can define the probability distribution function $f(\Omega,\theta)$ as,

$$f(\Omega,\theta) \equiv R^2\varrho(\Omega,\theta)/(NN_p), \tag{4.6}$$

then f is normalized to 1 and the free energy function can be expressed in terms of f as

$$\frac{F}{k_BT} = \ln N! - N\ln Q - NN_p\int f(\Omega,\theta)\omega(\Omega,\theta)\mathrm{d}\Omega\mathrm{d}\Theta + \frac{\ell_p^2N_p^2N^2}{2R^2}\int f(\Omega,\theta)|\sin(\theta-\theta')|f(\Omega,\theta')\mathrm{d}\Omega\mathrm{d}\theta\mathrm{d}\theta'. \quad (4.7)$$

Let $w(\Omega,\theta) = N_p\omega(\Omega,\theta)$ and $C = N\ell_p^2N_p^2/4\pi R^2$, then the free energy per chain can be written as,

$$\frac{F}{Nk_BT} = \ln\frac{C}{Q} - \int f(\Omega,\theta)w(\Omega,\theta)\mathrm{d}\Omega\mathrm{d}\theta + 2\pi C\int f(\Omega,\theta)|\sin(\theta-\theta')|f(\Omega,\theta')\mathrm{d}\Omega\mathrm{d}\theta\mathrm{d}\theta', \quad (4.8)$$

where the free energy is shifted by a constant number $\ln(L^2/4\pi R^2)$. To minimize the free energy functional with respect to $f(\Omega,\theta)$, we need to consider the saddle point equations,

$$w(\Omega,\theta) = 2\pi C\int|\sin(\theta-\theta')|f(\Omega,\theta')\mathrm{d}\theta'; \quad (4.9a)$$

$$f(\Omega,\theta) = \frac{\int_0^1 q(\Omega,\theta;s)q^*(\Omega,\pi+\theta;1-s)\mathrm{d}s}{\int\mathrm{d}\Omega\mathrm{d}\theta\int_0^1 q(\Omega,\theta;s)q^*(\Omega,\pi+\theta;1-s)\mathrm{d}s}, \quad (4.9b)$$

where q and q^* satisfy the modified diffusion equations

$$\frac{\partial}{\partial s}q(\mathbf{r},\mathbf{u};s) = \left[\frac{L}{\ell}\nabla_{\mathbf{u}}^2 - L\mathbf{u}\cdot\nabla_{\mathbf{r}} - w(\mathbf{r},\mathbf{u})\right]q(\mathbf{r},\mathbf{u};s); \quad (4.10a)$$

$$\frac{\partial}{\partial s}q^*(\mathbf{r},\mathbf{u};s) = \left[-\frac{L}{\ell}\nabla_{\mathbf{u}}^2 - L\mathbf{u}\cdot\nabla_{\mathbf{r}} + w(\mathbf{r},\mathbf{u})\right]q^*(\mathbf{r},\mathbf{u};s). \quad (4.10b)$$

The second equation in the above can be taken with a symmetry operation, $\mathbf{u}\to-\mathbf{u}$,

$$\frac{\partial}{\partial s}q(\mathbf{r},\mathbf{u};s) = \left[\frac{L}{\ell}\nabla_{\mathbf{u}}^2 - L\mathbf{u}\cdot\nabla_{\mathbf{r}} - w(\mathbf{r},\mathbf{u})\right]q(\mathbf{r},\mathbf{u};s); \quad (4.11a)$$

$$\frac{\partial}{\partial s}q^*(\mathbf{r},-\mathbf{u};s) = \left[-\frac{L}{\ell}\nabla_{\mathbf{u}}^2 + L\mathbf{u}\cdot\nabla_{\mathbf{r}} + w(\mathbf{r},\mathbf{u})\right]q^*(\mathbf{r},-\mathbf{u};s). \quad (4.11b)$$

They can also be written as,

$$\frac{\partial}{\partial s}q(\mathbf{r},\mathbf{u};s) = \left[\frac{L}{\ell}\nabla^2_{\mathbf{u}} - L\mathbf{u}\cdot\nabla_{\mathbf{r}} - w(\mathbf{r},\mathbf{u})\right]q(\mathbf{r},\mathbf{u};s); \tag{4.12a}$$

$$\frac{\partial}{\partial s}q^*(\mathbf{r},-\mathbf{u};s) = -\left[\frac{L}{\ell}\nabla^2_{\mathbf{u}} - L\mathbf{u}\cdot\nabla_{\mathbf{r}} - w(\mathbf{r},\mathbf{u})\right]q^*(\mathbf{r},-\mathbf{u};s). \tag{4.12b}$$

Finally, we express the two equations within our chosen coordinate system,

$$\frac{\partial}{\partial s}q(\Omega,\theta;s) = \left[\frac{L}{\ell}\frac{\partial^2}{\partial\theta^2} + L\Big(\sin\theta\frac{\partial}{\partial\Theta} - \frac{\cos\theta}{\sin\Theta}\frac{\partial}{\partial\Phi}\Big) - w(\Omega,\theta)\right]q(\Omega,\theta;s); \tag{4.13a}$$

$$\frac{\partial}{\partial s}q^*(\Omega,\pi+\theta;s) = -\left[\frac{L}{\ell}\frac{\partial^2}{\partial\theta^2} + L\Big(\sin\theta\frac{\partial}{\partial\Theta} - \frac{\cos\theta}{\sin\Theta}\frac{\partial}{\partial\Phi}\Big) - w(\Omega,\theta)\right]q^*(\Omega,\pi+\theta;s). \tag{4.13b}$$

Therefore, to minimize the free energy functional with respect to the probability distribution function $f(\Omega,\theta)$, we consider the iteration. First, an initial guess of f gives w according to the first saddle point equation (Eq. 4.9a); solve the two modified diffusion equations for q and q^* with a known w; then find a new f on the basis of the second saddle point equation (Eq. 4.9b). To do this, we may expand every function in a function space spanned by a set of orthonormal functions defined in Appendix A.

4.3.2 Representation of basis functions

With the basis functions $\psi_i(\Theta,\Phi,\theta)$ in Appendix A, where each index combination $\{lmn\}$ is rewritten as a single notation $\{i\}$, we have the expansions for f, w, q, and q^* as,

$$f(\Theta,\Phi,\theta) = f_i\psi_i(\Theta,\Phi,\theta), \tag{4.14}$$

$$w(\Theta,\Phi,\theta) = w_i\psi_i(\Theta,\Phi,\theta), \tag{4.15}$$

$$q(\Theta,\Phi,\theta;s) = q_{(s)}i\psi_i(\Theta,\Phi,\theta), \tag{4.16}$$

$$q^*(\Theta,\Phi,\pi+\theta;s) = q^*_i(s)\psi_i(\Theta,\Phi,\theta). \tag{4.17}$$

Eq. 4.9a comes to be

$$\begin{aligned} w_i &= \int w(\Theta,\Phi,\theta)\psi_i(\Theta,\Phi,\theta)\sin\Theta \mathrm{d}\Theta\mathrm{d}\Phi\mathrm{d}\theta \\ &= 2\pi C\int \psi_i(\Theta,\Phi,\theta)|\sin(\theta-\theta')|f(\Theta,\Phi,\theta')\sin\Theta\mathrm{d}\Theta\mathrm{d}\Phi\mathrm{d}\theta\mathrm{d}\theta' \\ &= 2\pi C A_{ij} f_j, \end{aligned} \tag{4.18}$$

where

$$A_{ij} = \int \psi_i(\Theta,\Phi,\theta)|\sin(\theta-\theta')|\psi_j(\Theta,\Phi,\theta')\sin\Theta d\Theta d\Phi d\theta d\theta'. \tag{4.19}$$

Eq. 4.9b can be rewritten under the expansions as

$$\begin{aligned} f_i &= \int f(\Theta,\Phi,\theta)\psi_i(\Theta,\Phi,\theta)\sin\Theta d\Theta d\Phi d\theta \\ &= \frac{\int \mathrm{d}s\int q(\Theta,\Phi,\theta;s)q^*(\Theta,\Phi,\pi+\theta;1-s)\psi_i(\Theta,\Phi,\theta)\sin\Theta d\Theta d\Phi d\theta}{\int \mathrm{d}s\int q(\Theta,\Phi,\theta;s)q^*(\Theta,\Phi,\pi+\theta;1-s)\sin\Theta d\Theta d\Phi d\theta} \\ &= \frac{Q_{ijk}\int q_j(s)q_k^*(1-s)\mathrm{d}s}{\int q_d(s)q_d^*(1-s)\mathrm{d}s}, \end{aligned} \tag{4.20}$$

where

$$Q_{ijk} = \int \psi_i(\Theta,\Phi,\theta)\psi_j(\Theta,\Phi,\theta)\psi_k(\Theta,\Phi,\theta)\sin\Theta d\Theta d\Phi d\theta. \tag{4.21}$$

Taking q as an example, the modified diffusion equation becomes

$$\begin{aligned} \frac{\mathrm{d}}{\mathrm{d}s}q_i(s) = \Bigg[&\frac{L}{\ell}\int \psi_i(\Theta,\Phi,\theta)\frac{\partial^2}{\partial\theta^2}\psi_j(\Theta,\Phi,\theta)\sin\Theta d\Theta d\Phi d\theta \\ &+L\int \psi_i(\Theta,\Phi,\theta)\left(\sin\theta\frac{\partial}{\partial\Theta}-\frac{\cos\theta}{\sin\Theta}\frac{\partial}{\partial\Phi}\right)\psi_j(\Theta,\Phi,\theta)\sin\Theta d\Theta d\Phi d\theta \\ &-\int \psi_i(\Theta,\Phi,\theta)w(\Theta,\Phi,\theta)\psi_j(\Theta,\Phi,\theta)\sin\Theta d\Theta d\Phi d\theta\Bigg] q_j(s), \end{aligned} \tag{4.22}$$

which can also written as,

$$\frac{\mathrm{d}}{\mathrm{d}s}q_i(s) = \left(-\frac{L}{\ell}n_j^2\delta_{ij} + LB_{ij} - Q_{ijk}w_k\right)q_j(s), \tag{4.23}$$

with the definition B_{ij},

$$B_{ij} = \int \psi_i(\Theta,\Phi,\theta)\left(\sin\theta\frac{\partial}{\partial\Theta}-\frac{\cos\theta}{\sin\Theta}\frac{\partial}{\partial\Phi}\right)\psi_j(\Theta,\Phi,\theta)\sin\Theta d\Theta d\Phi d\theta, \tag{4.24}$$

Finally, we define a matrix H_{ij},

$$H_{ij} = -\frac{L}{\ell} n_j^2 \delta_{ij} + LB_{ij} - Q_{ijk} w_k, \tag{4.25}$$

and write Eq. 4.23 as,

$$\frac{\mathrm{d}}{\mathrm{d}s} q_i(s) = H_{ij} q_j(s), \tag{4.26}$$

If the matrix H_{ij} can be diagonalized as $\mathbf{HU} = \mathbf{UD}$, we have the solution of the diffusion equation,

$$q_i(s) = U_{ij} \exp\left(D_j s\right) U_{j0}^{-1}. \tag{4.27}$$

The matrices, A_{ij}, B_{ij}, and Q_{ijk}, showing up in the saddle point equations and the modified diffustion equations can be accessed analytically and evaluated in Appendix F.

Therefore, the probability distribution function f can be solved from the iteration combining the expansions of the saddle point equations and the modified diffusion equations.Although we didn't have a chance to work on the numerical solutions, we expect that the Onsager model of semiflexible chains will display a conformation close to the perfect tetrahedral tennis-ball configuration.

Chapter 5

Summary

This thesis studied the conformation of 2-fold anisotropic molecules — including rigid rods and polymer chains — confined on a spherical surface. At low surface densities, the system is homogeneous and isotropic to maximize the positional and orientational entropies. Beyond a transition density, a configurational texture with coupled positional and orientational orderings emerges. Researchers have predicted the existence of several possible conformations of rigid rods on the spherical surface — tennis-ball, rectangle, and cut-and-rotate splay; all of them contain four +1/2 defects. However, in Chapter 2 of this thesis, the numerical solutions of Onsager model on thin rods confined on the spherical surface confirmed that the splay state with two +1 defects is the only stable state for such system. In Chapter 3, Monte Carlo simulations on the bead-bond model of self-avoiding semiflexible polymer chain was discussed and the results yielded solid evidence to prove that the ordered state always displays the tennis-ball symmetry. However, the tennis-ball configuration displayed by a long semiflexible chain may not have perfect tetrahedral symmetry with four defects located on the four vertices of a tetrahedron. Therefore, we considered a system of many semiflexible chains confined to a spherical surface in Chapter 4. Although Chapter 4 is not entirely finished, we can still conclude that, if the persistence length is comparable to the contour length for each semiflexible chain, the system may display a perfect tetrahedral tennis-ball configuration. Hence, to build up the tennis-ball symmetry for particular interest

and applications, one may try to coat the semiflexible polymer chains around the sphere.

For the system of rods or polymer chains, the disorder-order transition was also studied, which is comparable to the continuous isotropic-nematic transition of a fluid of hard rods embedded in a flat two-dimensional space. Based on the Onsager model of rigid rods confined on the spherical surface, the transition density in the limit of flat two-dimensional space agrees with the critical density predicted by the mean field theory for the hard-rod fluid in flat two dimensions . Away from the limit, the transition density deviates from the critical density of flat system due to the curvature of the spherical surface and the inhomogeneous distribution of rods on the sphere. Moreover, unlike the continuous transition of hard rods in flat two dimensions, the disorder-order transition was confirmed to have first-order characteristics for both the system of rigid rods and the system of polymer chains confined on the spherical surface.

For the purpose to look for the tennis-ball conformation, we conducted the theoretical research on the Onsager model of rigid rods confined to a spherical surface. On the basis of this research, we would like to open up new avenues to investigate the system of 2-fold anisotropic molecules confined on curved surfaces within an established area by presenting a straightforward numerical technique. First, although the research on rigid rods rules out the existence of tennis-ball configuration, we may further apply the Onsager model to the semiflexible chains; the mathematical preparation for such research has been fully established in Chapter 4. Accordingly, we may unveil the influence of semiflexibility of chains to their configuration on a curved surface, which is a perfect example to illustrate that not only the geometry of confinement but also the internal property of molecules may affect the configuration. Furthermore, another meaningful series of investigations based on the research in this thesis may be addressed to further study the 2-fold anisotropic molecules confined within a three dimensional geometry. One of the examples is the system of liquid crystals confined in a shell, which is closer to the experimental study on the nematic shell in double emulsion. Finally and most significantly, the researches of anisotropic molecules in confined geometries provides scientists and engineers a new horizon to build up various complex materials which can have a variety of

structures and properties and can be widely applied to chemistry, material science, biology, and so on.

Appendix A

Basis functions

In Chapter 2, to examine the Onsager model of rigid rods confined on a spherical surface, a set of orthonormal basis functions needs to be chosen for the purpose to expand the free energy. Here, the basis function is defined as combination of spherical harmonics $Y_{lm}(\Theta, \Phi)$ and Fourier basis $U_n(\theta)$. We have adopted the real version of the spherical harmonics [88],

$$Y_{lm}(\Theta,\Phi) = \begin{cases} \sqrt{2}\sqrt{\frac{2l+1}{4\pi}\frac{(l-m)!}{(l+m)!}}P_l^m(\cos\Theta)\cos(m\Phi) & \text{if } m > 0, \\ \sqrt{\frac{2l+1}{4\pi}}P_l^0(\cos\Theta) & \text{if } m = 0, \\ \sqrt{2}\sqrt{\frac{2l+1}{4\pi}\frac{(l+m)!}{(l-m)!}}P_l^{|m|}(\cos\Theta)\sin(|m|\Phi) & \text{if } m < 0, \end{cases} \tag{A.1}$$

where P_l^m is the associate Legendre function of the l-th and m-th rank [4]. Sinusoidal functions are used in a real Fourier expansion; the n-th rank basis $U_n(\theta)$ is,

$$U_n(\theta) = \begin{cases} \frac{1}{\sqrt{\pi}}\cos(n\theta) & \text{if } n > 0, \\ \frac{1}{\sqrt{2\pi}} & \text{if } n = 0, \\ \frac{1}{\sqrt{\pi}}\sin(|n|\theta) & \text{if } n < 0. \end{cases} \tag{A.2}$$

Appendix B

Symmetries of various states

In this thesis, we considered and compared four different configurations for the model system of rigid rods confined on a spherical surface, which are characterized by the symmetry properties of the distribution functions $\varrho(\Theta, \Phi, \theta)$:

$$\varrho(\Theta, \Phi; \theta) = \varrho(\Theta, \Phi; \theta + \pi), \tag{B.1}$$

$$\varrho(\Theta, \Phi; \theta) = \varrho(\Theta, \Phi + \pi; \theta), \tag{B.2}$$

$$\varrho(\Theta, \Phi; \theta) = \varrho(\Theta, -\Phi; -\theta), \tag{B.3}$$

$$\varrho(\Theta, \Phi; \theta) = \varrho(\pi - \Theta, \Phi + \pi/2; \pi - \theta), \tag{B.4}$$

$$\varrho(\Theta, \Phi; \theta) = \varrho(\pi - \Theta, \Phi; \pi - \theta), \tag{B.5}$$

$$\varrho(\Theta, \Phi; \theta) = \varrho(\pi - \Theta, \pi - \Phi; \pi + \theta), \tag{B.6}$$

$$\partial\varrho(\Theta, \Phi; \theta)/\partial\Phi = 0. \tag{B.7}$$

The table below summarizes the symmetry properties for each possible state,

State	(B.1)	(B.2)	(B.3)	(B.4)	(B.5)	(B.6)	(B.7)
Splay	√	√	√	√	√	√	√
Tennis-ball	√	√	√	√			
Rectangle	√	√	√		√		
Cut-and-rotate-splay	√	√				√	

Note that the distribution function of a splay state is Φ-independent.

Appendix C

Excluded volume of two rods on a spherical surface

To evaluate the excluded volume of two rigid rods, modeled as geodesic segments on the spherical surface, we put one rod on the equator for convenience and consider the area on the spherical surface that the center of the other rod cannot enter, which is actually $2S_{ABCD}$ shown in Fig. C.1. Assume that the angle between the two rods is γ. Let α be the latitude of the point C (or D); it satisfies

$$\sin\alpha = \sin\frac{\widehat{CP}}{R} = \sin\frac{\widehat{BC}}{R}\sin\gamma = \sin\frac{\ell}{2R}\sin\gamma \tag{C.1}$$

according to the knowledge of spherical trigonometry, where R is the radius of the sphere and arc $\widehat{CP}$ is perpendicular to arc $\widehat{AB}$.

Then we have

$$S_{ABCD} = R^2 \int_{\pi/2-\alpha}^{\pi/2} \sin\Theta \mathrm{d}\Theta \int_{B}^{A} \mathrm{d}\Phi = R^2 \sin\alpha \cdot \frac{\ell}{R}. \tag{C.2}$$

Therefore, the excluded volume becomes

$$2S_{ABCD} = 2R^2 \sin\frac{\ell}{2R}\sin\gamma \cdot \frac{\ell}{R} = \ell^2 \mathrm{sinc}\frac{\ell}{2R}\sin\gamma. \tag{C.3}$$

If we consider two orthogonal rods, the excluded volume is $\ell^2\mathrm{sinc}(\ell/2R)$. This derivation is only valid if $\widehat{BC}\ /R = \ell/2R \leq \pi/2$, i.e. $\ell/R \leq \pi$.

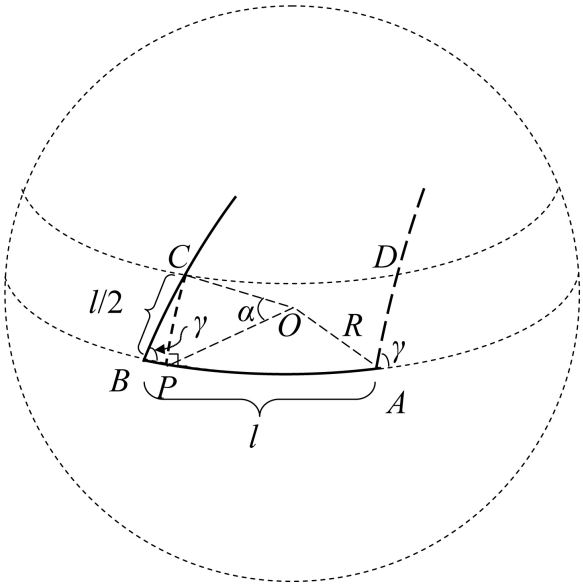

Figure C.1: To evaluate the excluded volume of two rods on a spherical surface, we set the angle between them to be γ and one of the rods (Arc $\widehat{AB}$) on the equator. So the surface area where the center of the other rod cannot enter is $2S_{ABCD}$.

Appendix D

Theoretical Evaluation of the elements of matrix W

In this appendix, we analytically evaluate $W_{l0n,l'0n'}$, i.e. the elements of matrix W (Eq. 2.11b), which is written as

$$W_{l0n,l'0n'} = \frac{4\pi R^2}{\ell^2} \int \left[N_{ln} P_l(\cos\Theta)\cos n\theta\right]\, w(\Theta,\Phi,\theta,\Theta',\Phi',\theta') \cdot \left[N_{l'n'} P_{l'}(\cos\Theta')\cos n'\theta'\right]\, \sin\Theta\sin\Theta'\, \mathrm{d}\Theta\mathrm{d}\Phi\mathrm{d}\theta\, \mathrm{d}\Theta'\mathrm{d}\Phi'\mathrm{d}\theta', \quad \text{(D.1)}$$

where N_{ln} is the normalization factor for the basis function $P_l(\cos\Theta)\cos n\theta$. We consider the integration $\int N_l P_l(\cos\Theta) w(\Theta,\Phi,\theta,\Theta',\Phi',\theta')\sin\Theta\mathrm{d}\Theta\mathrm{d}\Phi$ first, which is the excluded volume (coupled by $P_l(\cos\Theta)$) where rod 1 (direction fixed by θ) is excluded by rod 2 (position fixed on (Θ',Φ') and direction fixed by θ') on the unit sphere. We can write

$$\int N_{ln} P_l(\cos\Theta) w(\Theta,\Phi,\theta,\Theta',\Phi',\theta')\sin\Theta\mathrm{d}\Theta\mathrm{d}\Phi = \int_{-\ell/2R}^{\ell/2R} \frac{\ell}{R}\left|\sin\left[\theta-\tilde{\theta}'(\epsilon)\right]\right| N_{ln} P_l\big(\cos\tilde{\Theta}'(\epsilon)\big)\mathrm{d}\epsilon, \quad \text{(D.2)}$$

where ϵ is the length of arc on the rod 2 from the center of rod 2. $\tilde{\theta}'(\epsilon)$, a function of ϵ, is the angle locally between the longitudinal line and the segment of arc of rod

2 that ϵ locates, and we also define $\tilde{\Theta}'(\epsilon)$ as the polar angle of the segment specified by ϵ. According to the spherical trigonometry, one can have that

$$\frac{\sin\tilde{\theta}'}{\sin\Theta'} = \frac{\sin\theta'}{\sin\tilde{\Theta}'} \tag{D.3}$$

$$\cos\tilde{\Theta}' = \cos\Theta'\cos\epsilon + \sin\Theta'\sin\epsilon\cos\theta'. \tag{D.4}$$

By expanding the above equations with respect to small ϵ, we have

$$\cos\tilde{\Theta}' = \cos\Theta' + \epsilon\sin\Theta'\cos\theta' - \frac{\epsilon^2}{2}\cos\Theta' + \mathcal{O}(\epsilon^3) \tag{D.5}$$

$$\tilde{\Theta}' = \Theta' - \epsilon\cos\theta' + \frac{\epsilon^2}{2}\cot\Theta'\sin^2\theta' + \mathcal{O}(\epsilon^3) \tag{D.6}$$

$$\sin\tilde{\Theta}' = \sin\Theta' - \epsilon\cos\Theta'\cos\theta' + \frac{\epsilon^2}{2}\left(\cot\Theta'\cos\Theta'\sin^2\theta' - \sin\Theta'\cos^2\theta'\right) + \mathcal{O}(\epsilon^3) \tag{D.7}$$

$$\frac{\sin\tilde{\theta}'}{\sin\theta'} = 1 + \epsilon\cot\Theta'\cos\theta' - \frac{\epsilon^2}{2}\left(\cot^2\Theta'\sin^2\theta' - \cos^2\theta'\right) + \mathcal{O}(\epsilon^3) \tag{D.8}$$

$$\tilde{\theta}' = \theta' + \epsilon\cot\Theta'\sin\theta' + \frac{\epsilon^2}{2}\sin\theta'\cos\theta' + \mathcal{O}(\epsilon^3) \tag{D.9}$$

Then, we can also expand the integration D.2 as

$$
\begin{aligned}
&\int N_{ln}P_l(\cos\Theta)w(\Theta,\Phi,\theta,\Theta',\Phi',\theta')\sin\Theta\mathrm{d}\Theta\mathrm{d}\Phi \\
&= \int_{-\ell/2R}^{\ell/2R} \frac{\ell}{R}\left|\sin\left[\theta-\tilde{\theta}'(\epsilon)\right]\right| N_{ln}P_l(\cos\tilde{\Theta}'(\epsilon))\mathrm{d}\epsilon \\
&= \int_{-\ell/2R}^{\ell/2R} \frac{\ell}{R}\left|\sin\left[\theta-\theta'-\epsilon\cot\Theta'\sin\theta'-\frac{\epsilon^2}{2}\sin\theta'\cos\theta'+\mathcal{O}(\epsilon^3)\right]\right| \\
&\qquad \cdot N_{ln}P_l\left(\cos\Theta'+\epsilon\sin\Theta'\cos\theta'-\frac{\epsilon^2}{2}\cos\Theta'+\mathcal{O}(\epsilon^3)\right)\mathrm{d}\epsilon \\
&= \int_{-\ell/2R}^{\ell/2R} \frac{\ell}{R}\left|\sin(\theta-\theta')+\mathcal{A}_1(\Theta',\theta,\theta')\epsilon+\mathcal{A}_2(\Theta',\theta,\theta')\epsilon^2+\mathcal{O}(\epsilon^3)\right| \\
&\qquad \cdot N_{ln}\left[P_l(\cos\Theta')+\mathcal{B}_1(\Theta',\theta')\epsilon+\mathcal{B}_2(\Theta',\theta')\epsilon^2+\mathcal{O}(\epsilon^3)\right]\mathrm{d}\epsilon \\
&= \int_{-\ell/2R}^{\ell/2R} \frac{\ell}{R}\Big[\,|\sin(\theta-\theta')|\,N_{ln}P_l(\cos\Theta')+\mathcal{C}_1(\Theta',\theta,\theta')\epsilon+\mathcal{C}_2(\Theta',\theta,\theta')\epsilon^2+\mathcal{O}(\epsilon^3)\Big]\mathrm{d}\epsilon \\
&= \left(\frac{\ell}{R}\right)^2|\sin(\theta-\theta')|\,N_{ln}P_l(\cos\Theta')+\left(\frac{\ell}{R}\right)^4\mathcal{D}(\Theta',\theta,\theta')+\mathcal{O}\left[\left(\frac{\ell}{R}\right)^6\right],
\end{aligned}
\tag{D.10}
$$

where $\mathcal{A}_1$, $\mathcal{A}_2$, $\mathcal{B}_1$, $\mathcal{B}_2$, $\mathcal{C}_1$, $\mathcal{C}_2$, and $\mathcal{D}$ are funcions of Θ', θ, and θ'.

By substituting the expansion of the integration D.2 to the integral of $W_{l0n,l'0n'}$ (Eq. D.1), we have

$$
\begin{aligned}
W_{l0n,l'0n'} &= 4\pi\int N_{ln}P_l(\cos\Theta')\cos n\theta\left\{|\sin(\theta-\theta')|+\left(\frac{\ell}{R}\right)^2\mathcal{D}(\Theta',\theta,\theta')\right. \\
&\qquad \left.+\mathcal{O}\left[\left(\frac{\ell}{R}\right)^4\right]\right\}N_{l'n'}P_{l'}(\cos\Theta')\cos n'\theta'\ \sin\Theta'\mathrm{d}\Theta'\mathrm{d}\Phi'\mathrm{d}\theta\mathrm{d}\theta' \\
&= \frac{16\pi}{1-n^2}\delta_{ll'}\delta_{nn'}+\left(\frac{\ell}{R}\right)^2\mathfrak{F}(l,l',n,n')+\mathcal{O}\left[\left(\frac{\ell}{R}\right)^4\right],
\end{aligned}
\tag{D.11}
$$

where $\mathfrak{F}(l, l', n, n')$ is a function of l, l', n, and n'.

Especially, we can evaluate $W_{00n,00n'}$ with the excluded volume of two rods uniformly distributed on the sphercial surface which is derived in Appendix C:

$$\begin{aligned} W_{00n,00n'} &= \frac{4\pi R^2}{\ell^2} \int \frac{1}{\sqrt{\pi}} \cos n\theta \left(\frac{\ell}{R}\right)^2 \mathrm{sinc}\frac{\ell}{2R} \Big| \sin(\theta - \theta') \Big| \frac{1}{\sqrt{\pi}} \cos n'\theta' \mathrm{d}\theta \mathrm{d}\theta' \\ &= \frac{16\pi}{1-n^2} \mathrm{sinc}\frac{\ell}{2R} \delta_{nn'}. \end{aligned} \tag{D.12}$$

Appendix E

Persistence Length of Wormlike Chain in Two Dimensional Space

In this appendix, we discuss the persistence length of a wormlike chain embedded in flat two-dimensional space. Let $q(\mathbf{r}, \mathbf{u}; s)$ be the probability of a chain ending at the position $\mathbf{r}$ and with an ending vector $\mathbf{u}$, where s is its contour length. By taking an integral over all the position $\mathbf{r}$, it gives us

$$\int q(\mathbf{r}, \mathbf{u}; s)\, \mathrm{d}\mathbf{r} = Q(\mathbf{u}; s). \tag{E.1}$$

$Q(\mathbf{u}; s)$ means the probability for finding a chain with an ending vector $\mathbf{u}$ disregarding the position of its end. If we assume a Hamiltonian of a wormlike chain in two dimensions as

$$H = \frac{\varepsilon}{2} \int_0^L \left| \frac{\partial \mathbf{u}}{\partial s} \right|^2 ds, \tag{E.2}$$

the probability function $Q(\mathbf{u}; s)$ satisfies a diffusion-like equation

$$\frac{\partial}{\partial s} Q(\mathbf{u}; s) = \frac{1}{2\beta\varepsilon} \nabla_{\mathbf{u}}^2 Q(\mathbf{u}; s), \tag{E.3}$$

which can be written as

$$\frac{\partial}{\partial s} Q(\theta; s) = \frac{1}{2\beta\varepsilon} \frac{\partial^2}{\partial \theta^2} Q(\theta; s), \tag{E.4}$$

where θ is the angle that $\mathbf{u}$ makes with respect to a reference, say x-axis. The function $Q(\theta; s)$ can be expanded in terms of Fourier basis functions

$$Q(\theta; s) = \sum_m a_m(s) \frac{1}{\sqrt{2\pi}} e^{im\theta}, \tag{E.5}$$

which can be then substituted back to the diffusion-like equation

$$\sum_m \frac{\partial}{\partial s} a_m(s) \frac{1}{\sqrt{2\pi}} e^{im\theta} = \sum_m \frac{-m^2}{2\beta\varepsilon} a_m(s) \frac{1}{\sqrt{2\pi}} e^{im\theta}. \tag{E.6}$$

Then we must have the solution

$$a_m(s) \propto e^{\frac{-m^2 s}{2\beta\varepsilon}}. \tag{E.7}$$

The Green's function is then

$$G(\theta, \theta'; s) = \frac{1}{2\pi} \sum_m e^{im\theta} e^{-im\theta'} e^{\frac{-m^2|s|}{2\beta\varepsilon}}. \tag{E.8}$$

Now, for the purpose to determine the persistence length, we can evaluate the correlation function $\langle \mathbf{u}(s) \cdot \mathbf{u}'(s') \rangle$ as

$$\begin{aligned}
& \langle \mathbf{u}(s) \cdot \mathbf{u}'(s') \rangle \\
= \; & \frac{1}{2\pi} \int d\theta \int d\theta' \cos(\theta - \theta') G(\theta, \theta'; s - s') \\
= \; & \frac{1}{4\pi^2} \int d\theta \int d\theta' \cos(\theta - \theta') \sum_m e^{im(\theta - \theta')} e^{\frac{-m^2|s-s'|}{2\beta\varepsilon}} \\
= \; & \frac{1}{4\pi^2} \int d\theta \sum_m (\pi\delta_{m,1} + \pi\delta_{m,-1}) e^{\frac{-m^2|s-s'|}{2\beta\varepsilon}} \\
= \; & e^{\frac{-|s-s'|}{2\beta\varepsilon}}.
\end{aligned} \tag{E.9}$$

Hence, the persistence length is

$$\ell_p = 2\beta\varepsilon. \tag{E.10}$$

To prove the relationship above, the Monte Carlo simulation is also taken for a polymer chain confined on a two dimensional flat space. According to Fig. E.1, ℓ_p is linear to $\beta\varepsilon$ and the slope is 2.

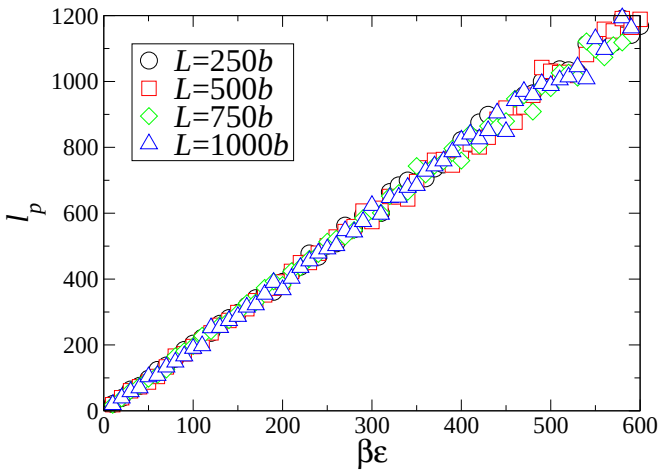

Figure E.1: Monte Carlo simulation shows that, for a polymer chain embedded in flat two dimensions, the slope of ℓ_p as a function of $\beta\varepsilon$ is 2.

Appendix F

Matrices in the Saddle Point and Modified Diffusion Equations

Here we derive the elements of A, B, and Q required to numerically solve the saddle point equations and the modified diffusion equations of Onsager model on the semiflexible chains confined to a spherical surface.

Recall the basis function,

$$\begin{aligned} &\psi_i(\Theta, \Phi, \theta) \\ &= Y_{l_i}^{m_i}(\Theta, \Phi) U_{n_i}(\theta) \\ &= N_{l_i|m_i|} P_{l_i}^{|m_i|}(\cos\Theta) U_{m_i}(\Phi) U_{n_i}(\theta), \end{aligned} \tag{F.1}$$

where $Y_{l_i}^{m_i}(\Theta, \Phi) = N_{l_i|m_i|} P_{l_i}^{|m_i|}(\cos\Theta) U_{m_i}(\Phi)$ is the real spherical harmonic and $U_{n_i}(\theta)$ is Fourier basis function, $\cos n\theta$ or $\sin n\theta$, and the normalization factor $N_{lm} = \sqrt{\frac{2l+1}{2}\frac{(l-m)!}{(l+m)!}}$.

First, we show the derivation of the matrix A,

$$
\begin{aligned}
&A_{ij} \\
&= \int \psi_i(\Theta,\Phi,\theta)|\sin(\theta-\theta')|\psi_j(\Theta,\Phi,\theta')\sin\Theta d\Theta d\Phi d\theta d\theta' \\
&= \delta_{l_i l_j}\delta_{m_i m_j}\int U_{n_i}(\theta)|\sin(\theta-\theta')|U_{n_j}(\theta')d\theta d\theta' \\
&= \delta_{l_i l_j}\delta_{m_i m_j}\int d\theta U_{n_i}(\theta)\int_0^{2\pi}|\sin x|U_{n_j}(\theta+x)dx \\
&= \delta_{l_i l_j}\delta_{m_i m_j}\int d\theta U_{n_i}(\theta)\left(\int_0^{\pi}\sin x U_{n_j}(\theta+x)dx - \int_{\pi}^{2\pi}\sin x U_{n_j}(\theta+x)dx\right) \\
&= \delta_{l_i l_j}\delta_{m_i m_j}\int d\theta U_{n_i}(\theta)\left(\int_0^{\pi}\sin x U_{n_j}(\theta+x)dx - \int_0^{\pi}\sin(x+\pi) U_{n_j}(\theta+x+\pi)dx\right) \\
&= \delta_{l_i l_j}\delta_{m_i m_j}\int d\theta U_{n_i}(\theta)\left(\int_0^{\pi}\sin x U_{n_j}(\theta+x)dx + \int_0^{\pi}\sin x U_{n_j}(\theta+x+\pi)dx\right) \\
&= \delta_{l_i l_j}\delta_{m_i m_j}\left(1+(-1)^{n_j}\right)\int d\theta U_{n_i}(\theta)\int_0^{\pi}\sin x U_{n_j}(\theta+x)dx \\
&= \delta_{l_i l_j}\delta_{m_i m_j}\left(1+(-1)^{n_j}\right)\int_0^{\pi}dx\sin x\int_0^{2\pi}U_{n_i}(\theta)U_{n_j}(\theta+x)d\theta \\
&= \delta_{l_i l_j}\delta_{m_i m_j}\left(1+(-1)^{n_j}\right)\delta_{n_i n_j}\frac{2}{1-n_i^2} \\
&= \frac{2\left(1+(-1)^{n_i}\right)}{1-n_i^2}\delta_{l_i l_j}\delta_{m_i m_j}\delta_{n_i n_j} \\
&= a_{(i)}\delta_{ij}
\end{aligned}
\tag{F.2}
$$

where $a_{(i)} = \frac{2}{1-n_i^2}\left(1+(-1)^{n_i}\right)$.

Second, we consider Q_{ijk}, which can be split into $Q_{ijk} = \Upsilon_{l_i l_j l_k}^{m_i m_j m_k}\mu_{n_i n_j n_k}$. For

$\mu_{n_i n_j n_k}$, we have,

$$
\begin{aligned}
&\mu_{n_i n_j n_k} \\
&= \int_0^{2\pi} U_{n_i}(\theta) U_{n_j}(\theta) U_{n_k}(\theta) d\theta \\
&= \begin{cases}
\frac{1}{\sqrt{2\pi}} \delta_{n_i n_j} & \text{if } n_k = 0 \\
\dfrac{1}{2\sqrt{\pi}^3} \displaystyle\int_0^{2\pi} \cos n_i\theta \left[\cos(n_j - n_k)\theta + \cos(n_j + n_k)\theta\right] d\theta & \\
= \dfrac{1}{2\sqrt{\pi}} \delta_{n_i, n_j + n_k} & \text{if } n_i \geq n_j \geq n_k > 0 \\
\dfrac{1}{2\sqrt{\pi}^3} \displaystyle\int_0^{2\pi} \cos n_i\theta \left[\cos(|n_j| - |n_k|)\theta - \cos(|n_j| + |n_k|)\theta\right] d\theta & \\
= \dfrac{1}{2\sqrt{\pi}} \left(\delta_{n_i, |n_j| - |n_k|} - \delta_{n_i, |n_j| + |n_k|}\right) & \text{if } n_i > 0 > n_k \geq n_j
\end{cases}
\end{aligned}
\tag{F.3}
$$

For $\Upsilon_{l_i l_j l_k}^{m_i m_j m_k}$, it is well known that, where Y_l^m is the complex spherical harmonic function,

$$
\begin{aligned}
&\int Y_{l_i}^{m_i *} Y_{l_j}^{m_j} Y_{l_k}^{m_k} d\Omega \\
&= \int_{-1}^{1} N_{l_i m_i} N_{l_j m_j} N_{l_k m_k} P_{l_i}^{m_i} P_{l_j}^{m_j} P_{l_k}^{m_k} dx \\
&\qquad \times \left(\frac{1}{\sqrt{2\pi}}\right)^3 \int_0^{2\pi} e^{-im_i\phi} e^{im_j\phi} e^{im_k\phi} d\phi \\
&= \int_{-1}^{1} N_{l_i m_i} N_{l_j m_j} N_{l_k m_k} P_{l_i}^{m_i} P_{l_j}^{m_j} P_{l_k}^{m_k} dx \cdot \frac{1}{\sqrt{2\pi}} \delta_{m_i, m_j + m_k} \\
&= (-1)^{m_i} \sqrt{\frac{(2l_i+1)(2l_j+1)(2l_k+1)}{4\pi}} \begin{pmatrix} l_i & l_j & l_k \\ 0 & 0 & 0 \end{pmatrix} \begin{pmatrix} l_i & l_j & l_k \\ -m_i & m_j & m_k \end{pmatrix}
\end{aligned}
\tag{F.4}
$$

which implies that, if $m_i = m_j + m_k$, then

$$
\begin{aligned}
&\int_{-1}^{1} N_{l_i m_i} N_{l_j m_j} N_{l_k m_k} P_{l_i}^{m_i} P_{l_j}^{m_j} P_{l_k}^{m_k} dx \\
&\qquad = (-1)^{m_i} \sqrt{\frac{(2l_i+1)(2l_j+1)(2l_k+1)}{2}} \begin{pmatrix} l_i & l_j & l_k \\ 0 & 0 & 0 \end{pmatrix} \begin{pmatrix} l_i & l_j & l_k \\ -m_i & m_j & m_k \end{pmatrix}
\end{aligned}
\tag{F.5}
$$

By substituting $\mu_{m_i m_j m_k}$, we write down $\Upsilon_{l_i l_j l_k}^{m_i m_j m_k}$ by integrating three real spherical harmonics as

$$
\begin{aligned}
&\Upsilon_{l_i l_j l_k}^{m_i m_j m_k} \\
&= \int_{S^2} Y_{l_i}^{m_i} Y_{l_j}^{m_j} Y_{l_k}^{m_k} d\Omega \\
&= \int_{-1}^{1} N_{l_i|m_i|} N_{l_j|m_j|} N_{l_k|m_k|} P_{l_i}^{|m_i|} P_{l_j}^{|m_j|} P_{l_k}^{|m_k|} dx \cdot \int_0^{2\pi} U_{m_i}(\phi) U_{m_j}(\phi) U_{m_k}(\phi) d\phi \\
&= \int_{-1}^{1} N_{l_i|m_i|} N_{l_j|m_j|} N_{l_k|m_k|} P_{l_i}^{|m_i|} P_{l_j}^{|m_j|} P_{l_k}^{|m_k|} dx \cdot \mu_{m_i m_j m_k} \\
&= \begin{cases}
(-1)^{m_i} \sqrt{\frac{(2l_i+1)(2l_j+1)(2l_k+1)}{2}} \begin{pmatrix} l_i & l_j & l_k \\ 0 & 0 & 0 \end{pmatrix} \begin{pmatrix} l_i & l_j & l_k \\ -|m_i| & |m_j| & 0 \end{pmatrix} \frac{1}{\sqrt{2\pi}} \delta_{m_i m_j} \\
\qquad \text{if at lease one, say } m_k = 0 \\
(-1)^{m_i} \sqrt{\frac{(2l_i+1)(2l_j+1)(2l_k+1)}{2}} \begin{pmatrix} l_i & l_j & l_k \\ 0 & 0 & 0 \end{pmatrix} \begin{pmatrix} l_i & l_j & l_k \\ -m_i & m_j & m_k \end{pmatrix} \frac{1}{2\sqrt{\pi}} \delta_{m_i, m_j + m_k} \\
\qquad \text{if } m_i \geq m_j \geq m_k > 0 \\
(-1)^{m_i+1} \sqrt{\frac{(2l_i+1)(2l_j+1)(2l_k+1)}{2}} \begin{pmatrix} l_i & l_j & l_k \\ 0 & 0 & 0 \end{pmatrix} \begin{pmatrix} l_i & l_j & l_k \\ -m_i & |m_j| & |m_k| \end{pmatrix} \frac{1}{2\sqrt{\pi}} \delta_{m_i, |m_j| + |m_k|} \\
\qquad \text{if } m_i > 0 > m_k \geq m_j \text{ and } |m_i| > |m_j| \\
(-1)^{m_j} \sqrt{\frac{(2l_i+1)(2l_j+1)(2l_k+1)}{2}} \begin{pmatrix} l_i & l_j & l_k \\ 0 & 0 & 0 \end{pmatrix} \begin{pmatrix} l_i & l_j & l_k \\ m_i & -|m_j| & |m_k| \end{pmatrix} \frac{1}{2\sqrt{\pi}} \delta_{m_i, |m_j| - |m_k|} \\
\qquad \text{if } m_i > 0 > m_k \geq m_j \text{ and } |m_i| < |m_j|
\end{cases}
\end{aligned}
\tag{F.6}
$$

where $\begin{pmatrix} l_i & l_j & l_k \\ m_i & m_j & m_k \end{pmatrix}$ is the Wigner 3-j symbol.

Finally, we figure out B_{ij}; let $B_{ij} = B_{ij}^{(1)} - B_{ij}^{(2)}$, where

$$
\begin{aligned}
&B_{ij}^{(1)} \\
&= \int \psi_i(\Theta,\Phi,\theta)\sin\theta\frac{\partial}{\partial\Theta}\psi_j(\Theta,\Phi,\theta)\sin\Theta d\Theta d\Phi d\theta \\
&= \int N_{l_i|m_i|}N_{l_j|m_j|}P_{l_i}^{|m_i|}(\cos\Theta)\frac{d}{d\Theta}P_{l_j}^{|m_j|}(\cos\Theta)\sin\Theta d\Theta\delta_{m_im_j}\sqrt{\pi}\mu_{-1,n_in_j} \\
&= N_{l_i|m_i|}N_{l_j|m_j|}\delta_{m_im_j}\sqrt{\pi}\mu_{-1,n_in_j}\int_0^{2\pi}P_{l_i}^{|m_i|}(\cos\Theta)\left(\frac{d}{d\cos\Theta}P_{l_j}^{|m_j|}(\cos\Theta)\right)\sin\Theta d\cos\Theta \\
&= -N_{l_i|m_i|}N_{l_j|m_j|}\delta_{m_im_j}\sqrt{\pi}\mu_{-1,n_in_j}\int_{-1}^{1}P_{l_i}^{|m_i|}(x)\left(\frac{d}{dx}P_{l_j}^{|m_j|}(x)\right)\sqrt{1-x^2}dx \\
&= -N_{l_i|m_i|}N_{l_j|m_j|}\delta_{m_im_j}\sqrt{\pi}\mu_{-1,n_in_j} \\
&\qquad\times\int_{-1}^{1}P_{l_i}^{|m_i|}(x)\left(-\frac{mx}{1-x^2}P_{l_j}^{|m_j|}(x)-\frac{1}{\sqrt{1-x^2}}P_{l_j}^{|m_j|+1}(x)\right)\sqrt{1-x^2}dx \\
&= N_{l_i|m_i|}N_{l_j|m_j|}\delta_{m_im_j}\sqrt{\pi}\mu_{-1,n_in_j}\int_{-1}^{1}P_{l_i}^{|m_i|}(x)\left(\frac{mx}{\sqrt{1-x^2}}P_{l_j}^{|m_j|}(x)+P_{l_j}^{|m_j|+1}(x)\right)dx \\
&= \frac{\sqrt{\pi}}{2}N_{l_i|m_i|}N_{l_j|m_j|}\delta_{m_im_j}\mu_{-1,n_in_j} \\
&\qquad\times\int_{-1}^{1}P_{l_i}^{|m_i|}(x)\left(P_{l_j}^{|m_j|+1}(x)-(l_j+|m_j|)(l_j-|m_j|+1)P_{l_j}^{|m_j|-1}(x)\right)dx
\end{aligned}
\tag{F.7}
$$

And we have the overlap integral of two associated Legendre polynomials

$$
\begin{aligned}
&N_{l_im}N_{l_j,m+1}\int_{-1}^{1}P_{l_j}^{m}(x)P_{l_j}^{m+1}(x)dx = \frac{(-1)^m}{4}\sqrt{(2l_i+1)(2l_j+1)} \\
&\times\sum_k\left(1-(-1)^k\right)(2k+1)\sqrt{\frac{(k-1)!}{(k+1)!}}\frac{\Gamma(\frac{k}{2})\Gamma(\frac{k}{2}+1)}{\frac{k-1}{2}!\Gamma(\frac{k+3}{2})}\begin{pmatrix}l_i & l_j & k\\ 0 & 0 & 0\end{pmatrix}\begin{pmatrix}l_i & l_j & k\\ -m & m+1 & -1\end{pmatrix}
\end{aligned}
\tag{F.8}
$$

where the sum is over $|l_i - l_j| \le k \le l_i + l_j$ and $k \ge 1$, and thie integral is zero unless $l_i + l_j$ is odd.

$$
\begin{aligned}
B_{ij}^{(2)} &= \int \psi_i(\Theta,\Phi,\theta)\frac{\cos\theta}{\sin\Theta}\frac{\partial}{\partial\Phi}\psi_j(\Theta,\Phi,\theta)\sin\Theta d\Theta d\Phi d\theta \\
&= \int N_{l_i|m_i|}N_{l_j|m_j|}P_{l_i}^{|m_i|}(\cos\Theta)\frac{1}{\sin\Theta}P_{l_j}^{|m_j|}(\cos\Theta)\sin\Theta d\Theta \\
&\quad \times \int U_{m_i}(\Phi)\frac{\partial}{\partial\Phi}U_{m_j}(\Phi)d\Phi\sqrt{\pi}\mu_{1,n_in_j} \\
&= -m_jN_{l_i|m_i|}N_{l_j|m_j|}\delta_{m_i,-m_j}\sqrt{\pi}\mu_{1,n_in_j}\int_{-1}^{1}P_{l_i}^{|m_i|}(x)P_{l_j}^{|m_j|}(x)\frac{dx}{\sqrt{1-x^2}}
\end{aligned}
\tag{F.9}
$$

And we have

$$
\begin{aligned}
\int_{-1}^{1}P_{l_j}^{m}(x)P_{l_j}^{m}(x)dx &= (-1)^{(l_i-l_j)/2}\frac{(l_i+m)!}{(l_i-m)!m!\frac{l_j-l_i}{2}!}\frac{\Gamma(m+\frac{1}{2})\Gamma(\frac{1}{2})\Gamma(\frac{l_i+l_j+1}{2})}{\Gamma(\frac{l_i-l_j+1}{2})\Gamma(\frac{l_i+l_j+2}{2})} \\
&\times {}_4F_3\left(\begin{matrix}\frac{1}{2}, & \frac{1}{2}, & -\frac{1}{2}(l_i-m-1), & -\frac{1}{2}(l_i-m) \\ \frac{1}{2}(l_j-l_i)+1, & -\frac{1}{2}(l_j+l_i-1), & m+1 & \end{matrix};1\right)
\end{aligned}
\tag{F.10}
$$

where $l_j \geq l_i$ and $l_i + l_j$ is even.

Appendix G

Publications

Wu-Yang Zhang, Ying Jiang, and Jeff Z. Y. Chen, *Phys. Rev. Lett.*, **108**, 057801 (2012);
Wu-Yang Zhang and Jeff Z. Y. Chen, *Europhys. Lett.*, **94**, 43001 (2011);
Ying Jiang, **Wu-Yang Zhang**, and Jeff Z. Y. Chen, *Phys. Rev. E*, **84**, 041803 (2011);
Wu-Yang Zhang, Ying Jiang, and Jeff Z. Y. Chen, *Soft Matter* (submitted).

Bibliography

[1] A. Akichina and P. Linse. *Macromolecules*, 35:5183, 2002.

[2] M. Allen and D. Tildesley. *Computer Simulation of Liquids*. Claredon, Oxford, 1987.

[3] D. G. Angelescu, R. Bruinsma, and P. Linse. *Phys. Rev. E*, 73:041921, 2006.

[4] G. B. Arfken. *Mathematical Methods for Physicists*. Academic Press, New York, 2nd edition, 1972.

[5] A. Arsenault, S. Fournier-Bidoz, B. Hatton, H. Míguez, N. Tétreault, E. Vekris, S. Wong, S. M. Yang, V. Kitaev, and G. A. Ozin. *J. Mater. Chem*, 14:781, 2004.

[6] J. Arsuage, R. K. Tan, M. Vazquez, D. Sumners, and S. C. Harvey. *Biophys. Chem.*, 101-102:475, 2002.

[7] M. A. Bates. *J. Chem. Phys.*, 128:104707, 2008.

[8] M. A. Bates, G. Skačej, and C. Zannoni. *Soft Matter*, 6:655, 2009.

[9] A. Baumgärtner. *Topics in Current Physics*, 36:145, 1984.

[10] J. D. Bunning, T. E. Faber, and P. L. Sherrell. *J. Physique*, 42:1175, 1981.

[11] C. R. Calladine, B. F. Luisi H. R. Drew, and A. A. Travars. *Understanding DNA*. Elsevier Academic Press, San Diego, 2004.

[12] J. J. Cerda, T. Sintes, and A. Chakrabarti. *Macromolecules*, 38:1469, 2005.

[13] M. E. Cerritelli, N. Cheng, A. H. Rosenborg, C. E. McPherson, F. P. Booy, and A. C. Steven. *Cell*, 91:271, 1997.

[14] Z. Y. Chen. *Phys. Rev. E*, 47:3765, 1993.

[15] Z. Y. Chen. *Phys. Rev. Lett.*, 71:93, 1993.

[16] Z. Y. Chen. *Macromolecules*, 26:3419, 1993.

[17] Z. Y. Chen and J. Noolandi. *Phys. Rev. A*, 45:2389, 1992.

[18] A. G. Cherstvy and R. G. Winkler. *J. Chem. Phys.*, 125:064904, 2006.

[19] S.-M. Cui, O. Akcakir, and Z. Y. Chen. *Phys. Rev. E*, 51:4548, 1995.

[20] T. T. Nguyen D. G. Angelescu, P. Linse and R. F. Bruinsma. *Eur. Phys. J. E*, 25:323, 2008.

[21] P.-G. de Gennes. *The Physics of Liquid Crystals*. Clarendon, Oxford, 1974.

[22] C. Jeppesen E. M. Mateescu and P. Pincus. *Europhys. Lett.*, 46:493, 1999.

[23] W. C. Earnshaw and S. C. Harrison. *Nature*, 268:598, 1977.

[24] G. Felsenfeld and M. Groudine. *Nature*, 421.

[25] A. Fernández-Nieves, V. Vitelli, A. S. Utada, D. R. Link, M. Márquez, D. R. Nelson, and D. A. Weitz. *Phys. Rev. Lett.*, 99:157801, 2007.

[26] R. Fletcher. Practical methods of optimization, 1987.

[27] D. Frenkel and R. Eppenga. *Phys. Rev. A*, 31:1776, 1985.

[28] K. M. Ho, C. T. Chang, and C. M. Soukoulis. *Phys. Rev. Lett.*, 65:3150, 1990.

[29] R. Hołyst and A. Poniewierski. *Phys. Rev. A*, 38:1527, 1988.

[30] H. Hopf. *Math. Ann.*, 96:427, 1926.

[31] M. Huber and H. Stark. *Europhys. Lett.*, 69:135, 2005.

[32] Y. Jiang and J. Z. Y. Chen. *Macromolecules*, 43:10668, 2010.

[33] R. F. Kayser and H. J. Raveché. *Phys. Rev. A*, 17:2067, 1978.

[34] A. R. Khokhlov and A. N. Semenov. *Physica A*, 108:546, 1981.

[35] A. R. Khokhlov and A. N. Semenov. *Physica A*, 112:605, 1982.

[36] H. Kimura and H. Nakano. *J. Phys. Soc. Jpn.*, 55:4186, 1986.

[37] J. Kindt, S. Tzlil, A. Ben-Shaul, and W. M. Gelbart. *Proc. Natl. Acad. Sci. U.S.A.*, 98:13671, 2001.

[38] D. L. Koch and O. G. Harlen. *Macromolecules*, 32:219, 1999.

[39] R. D. Kornberg. *Science*, 184:868, 1974.

[40] S. Kralj, R. Rosso, and E. G. Virga. *Soft Matter*, 7:670, 2010.

[41] I. M. Kulić, D. Andrienko, and M. Deserno. *Europhys. Lett.*, 67:418, 2004.

[42] K. K. Kunze and R. R. Netz. *Phys. Rev. Lett.*, 85:4389, 2000.

[43] I. Kusner and S. Srebnik. *Macromolecules*, 40:6432, 2007.

[44] J. C. LaMarque, T. L. Le, and S. C. Harvey. *Biopolymers*, 73:348, 2004.

[45] L. D. Landau and E. M. Lifshitz. *Statistical Physics*. Pergamon, London, U. K., 1969.

[46] F. Li, W. C. Yoo, M. B. Beernink, and A. Stein. *J. Am. Chem. Soc.*, 131:18548, 2009.

[47] C.-H. Lin, Y.-C. Tsai, and C.-K. Hu. *Phys. Rev. E*, 75:031903, 2007.

[48] T. Lopez-Leon, V. Koning, K. B. S. Davaiah, V. Vitelli, and A. Fernandez-Nieves. *Nature Physics*, 7:391, 2011.

[49] T. C. Lubensky and J. Prost. *J. Phys. II*, 2:371, 1992.

[50] K. Luger, A. W. Mäder, R. K. Richmond, D. F. Sargent, and T. J. Richmond. *Nature*, 389:251, 1997.

[51] W. E. McMullen. *Phys. Rev. A*, 38:6384, 1988.

[52] D. W. McQuigg, J. I. Kaplan, and P. L. Dubin. 96:1973, 1992.

[53] M. Mermin. In *Quantum Fluids and Solids,* edited by S. B. Trickey, E. D. Adams, and J. W. Dufty. Plenum Press, New York, 1977.

[54] S. Mitragotri and J. Lahann. *Nat. Mater.*, 8:15, 2009.

[55] R. P. Mondescu and M. Muthukumar. *Phys. Rev. E*, 57:4411, 1998.

[56] B. G. Moore and W. E. McMullen. *Phys. Rev. A*, 42:6042, 1990.

[57] G. Morrison and D. Thirumalai. *Phys. Rev. E*, 79:011924, 2009.

[58] D. R. Nelson. *Nano Lett.*, 2:1125, 2002.

[59] D. R. Nelson and R. A. Pelcovits. *Phys. Rev. B*, 16:2191, 1977.

[60] R. R. Netz and J. Joanny. *Macromolecules*, 32:9026, 1999.

[61] T. Odijk. *Macromolecules*, 19:2313, 1986.

[62] T. Odijk. *Biophys. J.*, 75:1223, 1998.

[63] A. L. Olins and D. E. Olins. *Science*, 183:330, 1974.

[64] N. H. Olson, M. Gingery, F. A. Eiserling, and T. S. Baker. *Virology*, 279:385, 2001.

[65] L. Onsager. *Ann. N.Y. Acd. Sci.*, 51:627, 1949.

[66] H. Poincaré. *J. Math. Pures Appl.*, 1:167, 1885.

[67] A. Poniewierski. *Phys. Rev. E*, 47:3396, 1993.

[68] A. Poniewierski and R. Hołyst. *Phys. Rev. A*, 38:3721, 1988.

[69] A. Poniewierski and R. Hołyst. *Phys. Rev. A*, 41:6871, 1990.

[70] K. E. Richards, R. C. Williams, and R. Calendar. *J. Mol. Biol.*, 78:255, 1973.

[71] T. J. Richmod and C. A. Davey. *Nature*, 423:145, 2003.

[72] N. Saitô, K. Takahashi, and Y. Yunoki. *J. Phys. Soc. (Japan)*, 22:219, 1967.

[73] T. Sato and A. Teramoto. *Macromolecules*, 29:4107, 1996.

[74] H. Shin, M. J. Bowick, and X. Xing. *Phys. Rev. Lett.*, 101:037802, 2008.

[75] G. Skačej and C. Zannoni. *Phys. Rev. Lett.*, 100:1802, 2008.

[76] A. Slosar and R. Podgornik. *Europhys. Lett.*, 75:631, 2006.

[77] A. J. Spakowitz and Z.-G. Wang. *Phys. Rev. Lett.*, 91:166102, 2003.

[78] P. J. Steinhardt, D. R. Nelson, and M. Ronchetti. *Phys. Rev. B*, 28:784, 1983.

[79] J. J. Stoker. *Differential Geometry*. Wiley, New York, 3rd edition, 1989.

[80] S. Stoll and P. Chodanowski. *Macromolecules*, 35:9556, 2002.

[81] J. P. Straley. *Phys. Rev. A*, 8:2181, 1973.

[82] G. B. Sukhorukov, E. Donath, S. Davis, H. Lichtenfeld, F. Caruso, V. I. Popov, and H. Möhwald. 9:759, 1998.

[83] R. van Roij, M. Dijkstra, and R Evans. *J. Chem. Phys.*, 113:7689, 2000.

[84] V. Vitelli and D. R. Nelson. *Phys. Rev. E*, 70:051105, 2004.

[85] V. Vitelli and A. M. Turner. *Phys. Rev. Lett.*, 93:215301, 2004.

[86] F. von Goeler and M. Muthukumar. *J. Chem. Phys.*, 100:7796, 1994.

[87] T. Wallin and P. Linse. *Langmuir*, 12:305, 1996.

[88] E. T. Whittaker and G. N. Watson. *A course of modern analysis*. Cambridge University Press, Cambridge, 4th edition, 1952.

[89] R. G. Winkler and A. G. Cherstvy. *Phys. Rev. Lett.*, 96:066103, 2006.

[90] W.-Y. Zhang and J. Z. Y. Chen. Unpublished.

[91] W.-Y. Zhang and J. Z. Y. Chen. *Europhys. Lett.*, 94:43001, 2011.

[92] W.-Y. Zhang, Y. Jiang, and J. Z. Y. Chen. *Phys. Rev. Lett.*, 108:057801, 2012.

[93] W.-Y. Zhang, Y. Jiang, and J. Z. Y. Chen. *Soft Matter*, (submitted) 2012.

[94] Z. X. Zhang, B. Greene, P. A. Thuman-Commike, J. Jakana, P. E. Prevelige, J. King, and W. Chiu. *J. Mol. Biol.*, 297:615, 2000.